

SMART BUILDINGS:
AN INTEGRATIVE DOUBLE SKIN FAÇADE DAMPER SYSTEM FOR SAFETY AND
ENERGY EFFICIENCY

BY

Rui Zhang

B.S., Architectural Engineering, University of South China, 2012

M.ENG., Mechanical Engineering, University of New Hampshire, 2017

DISSERTATION

Submitted to the University of New Hampshire

in Partial Fulfillment of

the Requirements for the Degree of

Doctor of Philosophy

In

Civil Engineering

December 2017

ProQuest Number:10688477

All rights reserved

INFORMATION TO ALL USERS

The quality of this reproduction is dependent upon the quality of the copy submitted.

In the unlikely event that the author did not send a complete manuscript and there are missing pages, these will be noted. Also, if material had to be removed, a note will indicate the deletion.



ProQuest 10688477

Published by ProQuest LLC (2018). Copyright of the Dissertation is held by the Author.

All rights reserved.

This work is protected against unauthorized copying under Title 17, United States Code
Microform Edition © ProQuest LLC.

ProQuest LLC.
789 East Eisenhower Parkway
P.O. Box 1346
Ann Arbor, MI 48106 – 1346

This thesis/dissertation has been examined and approved in partial fulfillment of the requirements for the degree of Doctor of Philosophy in Civil and Environmental Engineering by:

Dissertation Director, Dr. Tat Fu, Affiliated Assistant Professor,
Civil and Environmental Engineering

Dr. Erin Bell, Department Chair & Associate Professor,
Civil and Environmental Engineering

Dr. Charles Goodspeed, Associate Professor,
Civil and Environmental Engineering

Dr. May-Win Thein, Associate Professor,
Mechanical Engineering

Dr. Se Young Yoon, Assistant Professor,
Electrical and Computer Engineering

On November 28th, 2017

Original approval signatures are on file with the University of New Hampshire Graduate School.

ACKNOWLEDGEMENTS

I would like to first express my deepest gratitude for my advisor, Dr. Tat Fu, for his insightful advice, patient guidance, continued encouragement and relentless support throughout my doctoral career. He is a great mentor who has helped me grow professionally and become a better person. I will cherish those memories working with him.

I would like to express my appreciation Dr. Erin Bell and the department for the support and experimental resources, especially during the final year of my doctoral study. I am grateful of the guidance from Dr. May-win Thein and Dr. Se Young Yoon in the field of control theory, especially Dr. Thein's advice on active control experiments. I would also like to thank Dr. Charles Goodspeed for serving on the dissertation committee and offering insightful comments.

I appreciated the companionship and collaboration with former/current graduate and undergraduate students: Dr. Antonio Garcia-Palencia, Dr. Miguel Negrete-Padilla, Dr. Lukas Moschen, Kyle Wyatt, Daniel White, Travis Adams, Shounak Mitra, Christopher Allen, Shokoufeh Zargar, Travis Manning, Chao Yang, Weiru Tao, and Michael Figueroa.

I would also like to thank the current and former CEPS technicians: John Ahern, James Abare, Sheldon Parent, and Christopher Levesque for their help in offering me the resources in running the experiments. I am especially grateful of Scott Campbell, the machine shop manager, for helping me build the experimental structure that was a critical part of my dissertation research.

I would also like to extend my thanks to senior applications engineer, Chuck Searcy, at Moog Animatics for the control solutions of SmartMotors.

Finally, I would like to thank my family members for their support. This work would not have been possible without the love and support of my family. I would like to especially thank my wife for her companion over my doctoral career. I wish her the best in her research.

I gratefully acknowledge the partial support by the National Science Foundation through grant CMMI 12-28074, and the CEPS Graduate Fellowship from the University of New Hampshire.

TABLE OF CONTENTS

| | |
|--|-------------|
| ACKNOWLEDGEMENTS | iii |
| LIST OF TABLES | vii |
| LIST OF FIGURES | viii |
| ABSTRACT..... | x |
| Chapter 1. Introduction | 1 |
| 1.1 Introduction to smart buildings..... | 1 |
| 1.2 Structural Control | 3 |
| 1.3 Structural Health Monitoring..... | 10 |
| 1.4 Environmental Control..... | 11 |
| 1.5 Outline for the research..... | 13 |
| Chapter 2. The Double-skin façades mass damper system..... | 14 |
| 2.1 Double Skin Façade | 14 |
| 2.2 Mass Dampers | 17 |
| 2.3 The DSF mass damper system | 19 |
| Chapter 3. Energy control with DSF damper system..... | 22 |
| 3.1 Heat Dynamics in DSF..... | 22 |
| 3.2 DSF seasonal ventilation strategies | 25 |
| 3.3 Energy control with DSF damper system | 27 |
| Chapter 4. Passive structural control with Double Skin Façade damper system..... | 29 |
| 4.1 Structural Model and Formulation | 29 |
| 4.2 Experimental setup | 32 |
| 4.3 Test apparatus..... | 38 |
| 4.4 Numerical Simulations for Sizing Experimental Components | 39 |
| 4.4.1 DSF damper system optimization | 40 |
| 4.4.2 TMD system optimization | 42 |
| 4.4.3 Optimization results | 42 |
| 4.5 Result Discussion..... | 44 |
| 4.6 Conclusion | 48 |
| Chapter 5. Active structural control with the double skin façade damper system..... | 49 |
| 5.1 Introduction..... | 49 |
| 5.2 Controlling a Single-story Structure with AMD | 51 |

| | |
|--|------------|
| 5.2.1 System Model | 51 |
| 5.2.2 Controller Design..... | 56 |
| 5.2.3 Results..... | 63 |
| 5.3 Six-story Building Controlled with DSF damper system | 65 |
| 5.3.1 System Model | 65 |
| 5.3.2 Result Discussion..... | 74 |
| 5.4 Comparing Active control to Passive control | 78 |
| 5.5 Conclusion | 79 |
| Chapter 6. Structural health monitoring with DSF damper system..... | 80 |
| 6.1 Experiment setup | 82 |
| 6.2 Modal estimation..... | 88 |
| 6.3 Stiffness estimation | 97 |
| 6.3.1 Damage Configurations | 97 |
| 6.3.2 Least Square Stiffness Estimate | 99 |
| 6.4 Results Discussion | 101 |
| 6.5 Conclusion | 107 |
| Chapter 7 Conclusion | 108 |
| 7.1 Conclusion | 108 |
| 7.2 Limitations and Future Work..... | 110 |
| Appendix. Structural health monitoring with smartphones..... | 115 |
| A.1 Introduction..... | 115 |
| A.2 Experiment setup | 117 |
| A.3 Data acquisition..... | 120 |
| A.4 Testing configurations | 122 |
| A.5 Post processing | 124 |
| A.6 Results Discussion | 125 |
| A.7 Conclusion..... | 129 |
| Reference | 130 |

LIST OF TABLES

| | |
|---|-----|
| Table 1.1: Example of common energy dissipation devices installed in buildings. | 7 |
| Table 4.1: The equation of motion for TMD system (left column) and DSF damper system (right column). | 29 |
| Table 4.2. DSF mass damper configurations. | 34 |
| Table 4.3: Measured dampers' damping ratio. | 42 |
| Table 4.5: Average RMS Inter-story drift of the DSF damper systems compare to TMD system and uncontrolled structure (RMS: root mean square). | 47 |
| Table 4.6: Average RMS acceleration of the DSF damper systems compare to TMD system and uncontrolled structure (RMS: root mean square). | 47 |
| Table 5.1: Identified physical properties estimated from the experiment | 55 |
| Table 5.2: RMS floor acceleration of the AMD systems compare to the uncontrolled structure. | 64 |
| Table 5.3: RMS floor displacement of the AMD systems compare to the uncontrolled structure. | 64 |
| Table 5.4: Identified AMD physical properties | 68 |
| Table 5.5: The Q and R matrix used in controller design | 73 |
| Table 5.6: Summation of RMS command control forces of the DSF damper and AMD systems | 75 |
| Table 5.7: Average RMS acceleration of the DSF damper systems compare to AMD system and uncontrolled structure (RMS: root mean square). | 76 |
| Table 5.8: Average RMS displacements of the DSF damper systems compare to AMD system and uncontrolled structure (RMS: root mean square). | 76 |
| Table 6.1. Motion patterns of the actuators targeting the first and second modes | 90 |
| Table 6.2. Motion patterns of the actuators targeting the first and second modes | 92 |
| Table 6.3: Damage Configurations for DSF configuration (Shaded Floors Are Damaged). | 98 |
| Table 6.4: Definition of the damage identification status and their corresponding color shade. | 101 |
| Table 6.5: Stiffnesses estimated for the AMD system excited at the first and second modes.... | 102 |
| Table 6.6: Stiffnesses estimated for the DMD system excited at the first and second modes.... | 103 |
| Table 6.7: Stiffnesses estimated for the DSF system excited at the first and second modes..... | 104 |
| Table 6.8: DMD configuration estimated stiffness, N/mm (% change from the healthy structure). | 106 |
| Table 6.9: DSF configuration estimated stiffness, N/mm (% change from the healthy structure). | 106 |
| Table A.1: Hardware specification and the price comparison of smartphones and wireless accelerometers..... | 122 |
| Table A.2: Damage Configurations (Shaded Floors Are Damaged) (Kyle, 2015)..... | 123 |
| Table A.3: Smartphone sensors: estimated stiffness, N/mm (% change from the healthy structure). | 128 |
| Table A.4: Microstrain Sensors: estimated stiffness, N/mm (% change from the healthy structure). | 128 |

LIST OF FIGURES

| | |
|---|----|
| Figure 1.1: Building with and without base isolator (source: Advanced Earthquake Resistant Design Techniques, 2015). | 4 |
| Figure 1.2: Acceleration spectrum for building with and without base isolator (source: Santhosh <i>et al.</i> , 2013). | 5 |
| Figure 1.3: Impact of building energy consumption in the United States (source: WBDG, 2015). | 12 |
| Figure 2.1: A typical double skin façade. | 15 |
| Figure 2.2: Mass damper systems. | 18 |
| Figure 2.3: Double skin façade (DSF) damper system; the outer skin moves as a mass damper. | 19 |
| Figure 2.4: Motions of the movable double skin façade system. | 19 |
| Figure 2.5: Details of the connections between the primary building and the movable façade: the wide flange rail system is attached with bearings, dampers and actuators to allow and control linear motions. | 20 |
| Figure 3.1: Heat Transfer in DSF | 23 |
| Figure 3.2: DSF ventilation strategy in cooling (a) and heating season (b). | 26 |
| Figure 3.3: (a) Energy cost compared to airflow; (b) airflow compared to DSF cavity depth (source data from Torres <i>et al.</i> , 2007 and Tascón, 2008). | 28 |
| Figure 4.1: The six-story experiment structure. | 33 |
| Figure 4.2: DSF damper configurations (picture credit Rui Zhang 2016). | 34 |
| Figure 4.3: Details of the DSF mass damper mechanism (picture credit Rui Zhang 2016). | 36 |
| Figure 4.4: Details of the tuned mass damper (TMD). | 37 |
| Figure 4.5: Shake table at University of New Hampshire (picture credit Rui Zhang 2016). | 39 |
| Figure 4.6: Configuration to measure the damping of the linear shafts. | 41 |
| Figure 4.8: Springs used in the experiments. | 44 |
| Figure 4.9: Top floor acceleration response of uncontrolled structure, TMD and (a) one-damper DSF system under Newhall earthquake, (b) two-damper DSF system under Erzincan earthquake, (c) three-damper DSF system under Northridge earthquake and (d) three-damper DSF system under Jiji earthquake. | 45 |
| Figure 4.10: Floor RMS displacements under both simulated and experiment tested DSF two-damper case, TMD and uncontrolled structure. | 46 |
| Figure 5.1: The experiment structure. | 52 |
| Figure 5.2: Hardware used in the experiment. | 53 |
| Figure 5.3: Illustration of the real-time (RT) system. | 54 |
| Figure 5.4: Experiment configuration to measure the stiffness and damping properties of the actuator. | 55 |
| Figure 5.5: Block Diagram of the Active Feedback Control System | 56 |
| Figure 5.6: Workflow of the real-time control system. | 61 |
| Figure 5.7: floor acceleration response under Northridge (left) and Newhall Earthquake (Right). | 63 |

| | |
|--|-----|
| Figure 5.8: The six-story experiment structure..... | 66 |
| Figure 5.9: AMD damper configurations..... | 67 |
| Figure 5.10: DSF damper configurations: one-damper (left), two-damper (middle) and three dampers (right)..... | 70 |
| Figure 5.11: the master and slave SmartMotor configurations for DSF damper systems. | 71 |
| Figure 5.12: DSF damper configurations..... | 72 |
| Figure 5.13: Top floor acceleration response of uncontrolled structure, AMD and (a) one-damper DSF system under Newhall earthquake, (b) two-damper DSF system under Erzincan earthquake, (c) three-damper DSF system under Northridge earthquake and (d) three-damper DSF system under Jiji earthquake. | 75 |
| Figure 5.14: Average reduction in acceleration comparing active and passive control systems.. | 78 |
| Figure 6.1: Six-story shear experimental structure. | 83 |
| Figure 6.2: Spring and turnbuckles used for cross bracing photo credit: Kyle Wyatt 2015) | 83 |
| Figure 6.3: Test configuration for a “healthy” structure..... | 84 |
| Figure 6.4: Test configuration for a damaged floor (6th) case. | 85 |
| Figure 6.5: The motor and belt driven actuator set-up..... | 85 |
| Figure 6.6: System setup for the AMD (left), DMD (middle) and DSF (right) systems..... | 87 |
| Figure 6.7: The master and slave motors configuration. | 89 |
| Figure 6.8: Motion patterns of the actuators targeting under the DMD configuration..... | 91 |
| Figure 6.9: Motion patterns of the actuators under DSF configuration..... | 92 |
| Figure 6.10: Structural harmonic response for DSF (left) and AMD (right)..... | 93 |
| Figure 6.11: AMD system’s harmonic response and mode shapes. | 94 |
| Figure 6.12: DMD system’s harmonic response and mode shapes. | 95 |
| Figure 6.13: DSF system’s harmonic response and mode shapes. | 96 |
| Figure A.1: Contribution of Kyle and the author (Rui). | 117 |
| Figure A.2: Spring and turnbuckles used for cross bracing (Picture credit: Kyle Wyatt 2015). | 118 |
| Figure A.3: Test configuration for a “healthy” structure..... | 119 |
| Figure A.4: Test configuration for a damaged floor (6th) case. | 120 |
| Figure A.5: Difference in workflow comparing wireless accelerometers to smart phones (Kyle, 2015)..... | 121 |
| Figure A.6: Microstrain to Smartphone time history acceleration data comparison. (Kyle, 2015)..... | 126 |

ABSTRACT

SMART BUILDINGS:

AN INTEGRATIVE DOUBLE SKIN FAÇADE DAMPER SYSTEM FOR SAFETY AND ENERGY EFFICIENCY

by

Rui Zhang

University of New Hampshire, December, 2017

A smart building is an intelligent living space that elevates energy efficiency, comfort and safety. The word “smart” implies that the building would have a decision making system that can sense its conditions and reacts to them in an automatic and effective manner. Modern buildings contain many subsystems and, thus, to achieve automation, sophisticated sensing networks and robust control systems must be installed. The proposed research focuses on integrating several building systems — structural health monitoring (SHM), and structural and environmental controls — and explores synergy among them to improve efficiency and sustainability of buildings.

More specifically, an integrative, smart building system is developed by combining double skin façades and mass dampers in buildings to improve both safety and energy efficiency. Double skin façade systems protect and insulate buildings with two heavy glass layers between which air is allowed to flow for ventilation. By enabling movements in the outer façade skin, the façade can be used as a mass damper that reduces structural vibration and damage during earthquakes and wind storms. The added mobility also leads to innovative ways to control

ventilation rate and improve energy efficiency by adjusting the gap size between the outer and inner skins.

In this dissertation research, the energy impact of the integrated system was first investigated. Then both passive and active structural control strategies were experimented and analyzed on a six-story shear building model. Results indicated the proposed system can significantly reduce structural response under the earthquakes excitations. In addition, the sensor networks and actuators introduced by the active structural control system were utilized for structural health monitoring purposes. The actuators provided harmonic excitations while the acceleration data were collected by the sensor networks to perform damage diagnosis.

Finally, since typical SHM systems require large networks of sensors that are costly to install, this dissertation research also examined using smartphones as alternative sensors. Using the aforementioned six-story experimental structure, a sensing system consisted of six smartphones was tested and proven effective in detecting structural damage. The experimental result demonstrates that further developments of smartphone SHM can lead to cost-effective and quick sensor deployments.

Chapter 1. Introduction

1.1 Introduction to smart buildings

Smart buildings integrate cyber and physical systems to make automated adjustments to buildings. This requires a building to know its conditions and how to react to them. The Smart Buildings Institute (2015) -- a non-profit organization that developed a smart building certification process -- describes a certified smart building as one that (1) provides actionable information regarding the performance of building systems and facilities; (2) proactively monitors and detects errors or deficiencies in building systems; (3) integrates systems to an enterprise business level for real-time reporting and management utilization of operations, energy and occupant comfort; and (4) incorporates the tools, technologies, resources and practices to contribute to energy conservation and environmental sustainability.

With the advancement of human civilization and technology, buildings today are complex concatenations of structural, HVAC (heating, ventilating, and air conditioning), electrical, lighting, plumbing and security systems, typically these systems operate independently, and smart buildings explore the synergy among those systems by embedding sensing and control systems to improve performance and efficiency.

Smart buildings can improve structural safety by utilizing structural control (SC) and structural health monitoring (SHM). SC systems aim to control building response under extreme

events (*e.g.* earthquakes and strong winds) such that buildings can remain safe and serviceable. SHM, on the other hand, evaluate structural integrity by installing sensors throughout a building. SHM can identify, locate and estimate structural damage and call for further investigations and repair.

Aside from structural safety, smart buildings focus on optimizing building energy efficiency and improve occupant satisfaction. Smart buildings integrate cyber (data) and physical (control) systems and manage the building environment through real-time and data-driven analytics, the goal is to improve operational performance and occupant comfort while minimizing energy consumption. Nowadays, sensors are increasingly common in buildings to gather data about buildings' environmental conditions such as lighting, temperature and occupancy, recent advances in data sensing and analysis are creating new possibilities for making buildings smarter than before by learning and even anticipating their occupants' needs (Poole and Shvartzberg, 2015).

1.2 Structural Control

Structural control (SC) can change structural dynamic properties and reduce structural response during extreme events such as earthquakes and strong winds. These changes include modifying the natural frequencies, damping, and dynamic response of the structures. The three major categories of SC systems are introduced in the following sessions: base isolation, passive energy dissipation systems, and active/semi-active systems. The following sections discuss some of these systems.

1.2.1 Base isolation system

Base isolators are the most commonly used type among passive SC systems. Base isolation places bearing pads between the foundation and the structure to decouple a building from its foundation (Figure 1.1). During a seismic event, the isolation bearings intend to deform and, thus, allowing the superstructure to essentially act like a rigid body. Compared to a traditional structure with a fixed base (Figure 1.1), a building foundation equipped with base isolation transfers less force to the superstructure and, thus, reduces responses in the superstructure and its contents.

With a base isolation system, a structure's fundamental period is longer compared to that of the same structure with a fixed base. This shifts the position of the structure in the spectrum from the peak-plateau region to the lower regions (Figure 1.2). Also, there is an increased damping introduced at the base level which leads to reduction in the spectral acceleration (Santhosh, 2013). Chopra (2007) states that base isolation systems are effective in reducing

structural motions during earthquakes mainly because of the aforementioned lengthening of the fundamental frequency. The damping in the isolation system and associated energy dissipation is only a secondary factor in reducing structural response.

Base isolation can be used both for new structural design and seismic retrofit. A number of prominent buildings in California (e.g., Pasadena City Hall, San Francisco City Hall, LA City Hall) have been seismically retrofitted using base isolation systems (Xi, 2014). However, base isolation is not suitable for all buildings as current base isolator applications occur in low- to mid-rise buildings (Becker, 2015). Given that high-rise buildings already have long periods, and, thus, the effectiveness of base isolation is reduced. In addition, structural weight supported by the isolation bearings will be considerably larger in high-rise buildings compared to low/mid-rise buildings. The requirement to both support large weights and permit lateral motions makes the isolation bearings difficult to design.

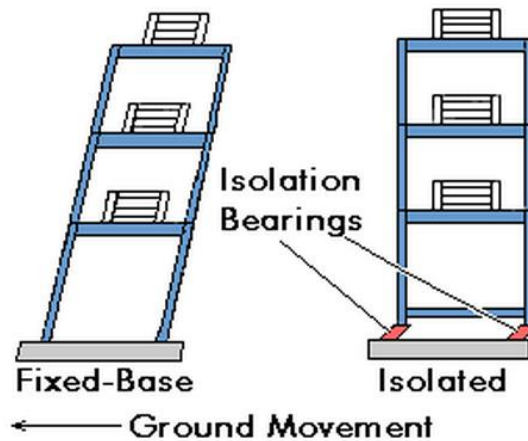


Figure 1.1: Building with and without base isolator (source: Advanced Earthquake Resistant Design Techniques, 2015).

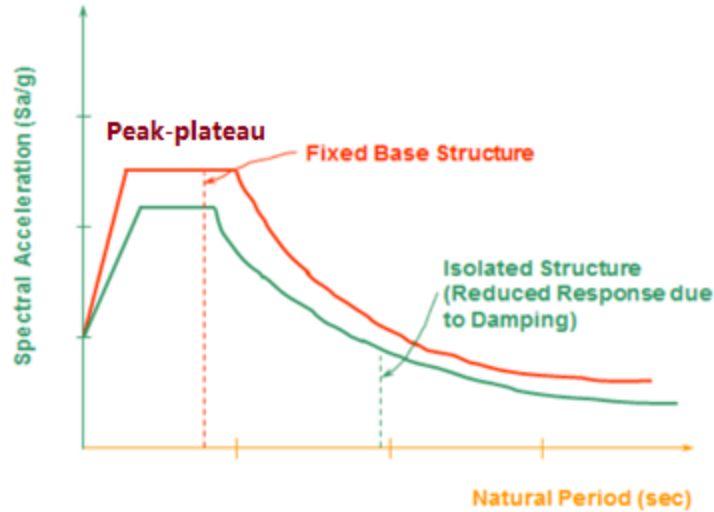


Figure 1.2: Acceleration spectrum for building with and without base isolator (source: Santhosh *et al*, 2013).

1.2.2 Mass damper system

A mass damper is a secondary mass attached to the primary structure and is designed to move in a manner that reduces the primary structure's motions. Tuned mass damper (TMD) is one of the most common mass damper systems. For a typical TMD system, the damper is made of huge concrete blocks or steel bodies coupled with structure by means of springs, fluids or pendulums. The frequency of the damper is tuned to a particular structural frequency so that when that frequency is excited, the damper resonates out of phase with the structural motion (Connor, 2003). TMD concept was first suggested by Frahm in 1909 (Frahm, 1909) to reduce the rolling motion of ships as well as ship hull vibrations, and since then, the theories of TMD has been investigated intensively. Significant contributions were made by Randall *et al.* (1981), Warburton (1981, 1982), Warburton and Ayorinde (1980), and Tsai and Lin (1993). The first application of TMD in buildings is in the John Hancock Tower (1976) at Boston, USA. To date, TMD has proved its effectiveness in applications of various engineering structures (e.g. bridges,

skyscrapers, TV towers and etc.) (GERB 2016). The primary limitation of a TMD is its narrow frequency bandwidth. A TMD can only suppress the response of a primary system in a frequency band, and, therefore, is ineffective for excitation in other frequency ranges.

Due to the limitations of TMD systems, a multiple tuned mass damper (MTMD) system was introduced to increase the robustness by broadening its control frequency bandwidth. A MTMD consist of multiple mass dampers with natural frequencies distributed around the natural frequency(ies) of the target structure. The MTMD concept was first proposed by Igusa and Xu (1994) and Yamaguchi and Harnpornchai (1993). The theory of MTMD was later extensively studied in 1990s (Igusa and Xu (1994), Yamaguchi and Harnpornchai (1993)). MTMD can work in parallel at one floor (e.g., Li, 2000 and 2002, Zuo and Nayfeh, 2005) or distributed spatially on its target structural system (e.g., Bergam *et al.*, 1988, Chen and Wu, 2001). It has been demonstrated experimentally that MTMD with distributed natural frequencies are more effective than a single TMD (Chen and Wu, 2001, Lin *et al.*, 2010).

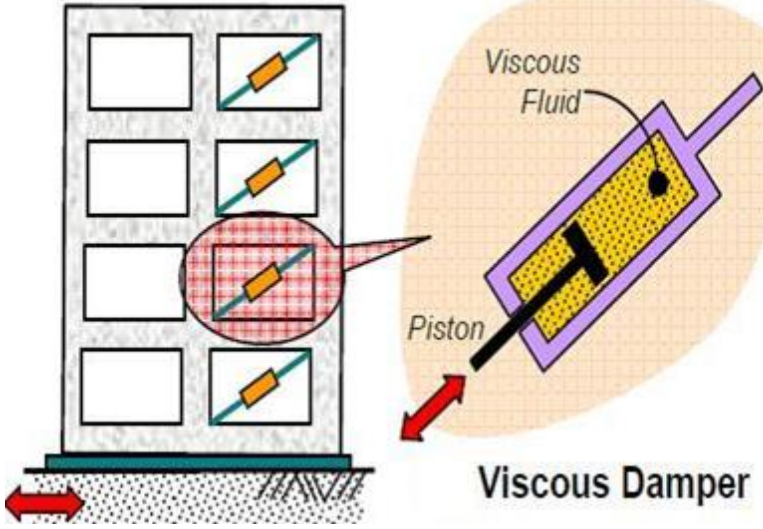
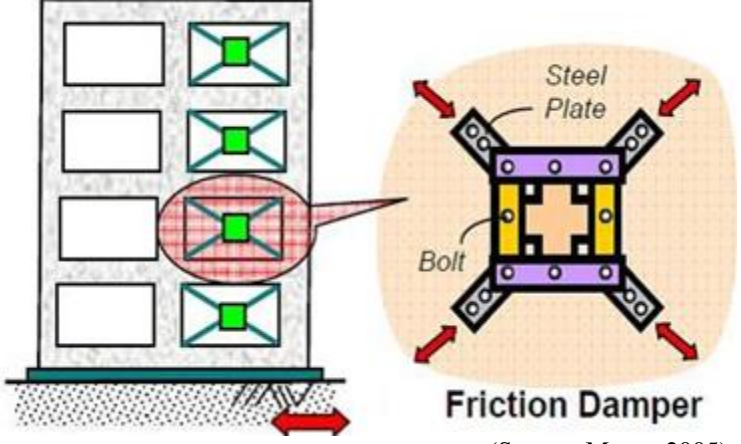
In addition to MTMD systems, Fu and Johnson (2011) studied a distributed mass damper (DMD) system in which a mass damper was placed at every story of a building. Unlike TMD and MTMD systems with concentrated mass, the DMD system distributed the damper weight throughout the building and, thus, allows for a larger total damper weight. Results showed that the DMD system could reduce structural vibration significantly.

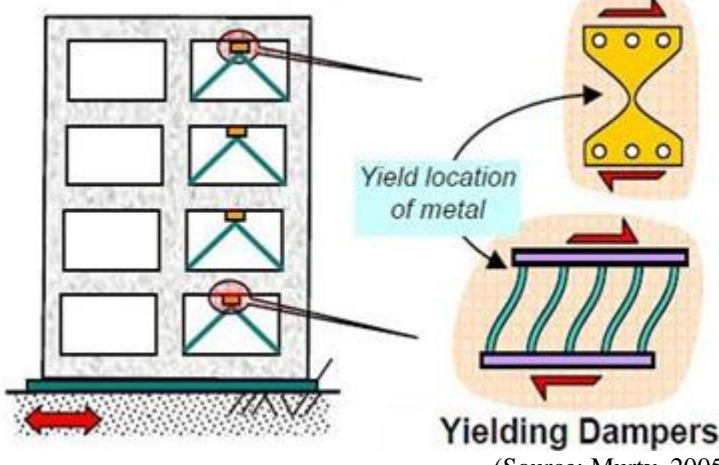
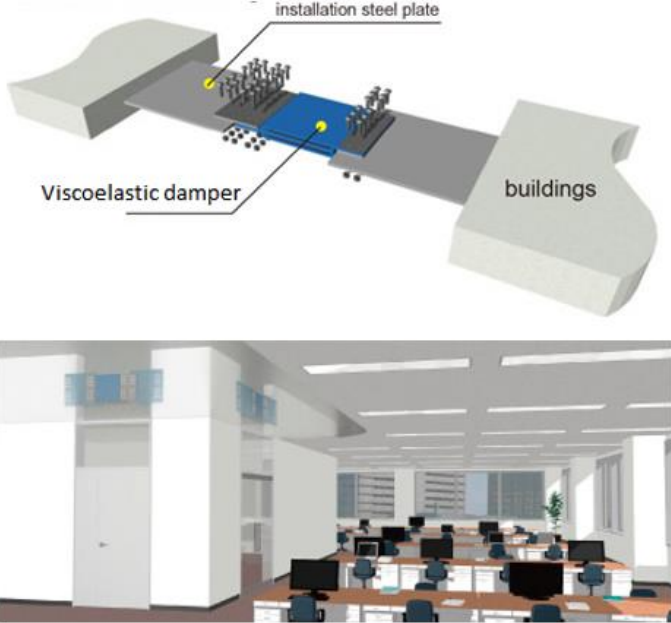
1.2.3 Energy dissipation devices

Energy dissipation devices are essentially extra damping elements. By equipping a building with additional high damping elements, motion energy can be quickly dissipated in buildings such that building damage can be reduced. A wide range of energy dissipation devices

have been developed and installed in buildings (Advanced Earthquake Resistant Design Techniques, 2015). These devices (other than mass dampers) can be grouped four major categories and listed in Table 1.1:

Table 1.1: Example of common energy dissipation devices installed in buildings.

| | |
|---|---|
| <p>Viscous Dampers</p> <p>utilized the forced movement (orificing) of fluids within the damper</p> |  <p>(Source: Murty, 2005)</p> |
| <p>Friction Dampers</p> <p>these utilize frictional forces to dissipate energy</p> |  <p>(Source: Murty, 2005)</p> |

| | |
|--|---|
| <p>Metallic Dampers</p> <p>also known as yielding dampers utilize the deformation of metal elements within the damper</p> |  <p>Yielding Dampers (Source: Murty, 2005)</p> |
| <p>Viscoelastic Dampers</p> <p>utilize the controlled shearing of solids</p> |  <p>Viscoelastic damper</p> <p>buildings</p> <p>(Source: Constec Engi, Co. 2016)</p> |

1.2.2 Active control and Semiactive control

Active control systems aim to apply control force (*e.g.*, via actuators) for suppressing structural motions. Actions of the actuators are determined by real-time measurements in structural response and control algorithms. A variety of active control mechanisms have been studied, including active bracing, active variable stiffness and active mass damper/driver systems

(Soong, 1990). Active bracing systems connect structures to prestressed tendons or braces, whose forces are controlled with electrohydraulic servo (Reinhorn, *et al.*, 1989, Chung *et al.*, 1988, Chung *et al.*, 1989). Active variable stiffness systems shift resonant modes of structures away from the dominate frequencies of earthquakes to adjust structural stiffness (Kobori *et al.*, 1993). An active mass damper (AMD) introduces active control forces to a passive mass damper system by installing actuators and controlling movements of the mass damper. Compared to the passive mass damper system in which the damper is tuned to a certain frequency, the AMD system have less limitation on its frequency bandwidth, and, thus, can be more effective in reducing motions when the structure is subjected to a seismic load with a wide frequency range (Dyke, 1996). Contrast to the active tendon/brace system, the magnitude of actuator force required in AMD system is much smaller (Singh *et al.*, 1997). Details about the AMD systems will be discussed in Chapter 4 for the proposed active control research.

Semiactive control system is defined as a system that cannot increase the mechanical energy in the controlled system and inherently stable (Dyke *et al.*, 1998). They are essentially passive energy dissipation systems with controllable parameters (e.g. stiffness and damping). Semiactive systems can adapt to various kinds of excitations by controlling structural parameters according to structural conditions. Additionally, unlike active system to supply external energy to actuators to mitigate structural motion directly, semiactive system require less external power to vary its controllable parameters. This low power needs that can be satisfied with backup power system is crucial because building might lost power supply under extreme events. Most common examples of semiactive systems are variable stiffness or damping systems (Liu *et al.*, 2008) and magnetorheological (MR) dampers (Dyke *et al.*, 1998).

1.3 Structural Health Monitoring

Natural and man-made hazards such as earthquakes, hurricanes, and explosions will damage structures or exacerbate the existing structural damage. Structural health monitoring (SHM) assesses a structure's integrity through analyzing structural response data (*e.g.*, accelerations and strains) to detect real time changes in structural characteristics. SHM system monitor the structure continuously thus the user can response to emergencies regarding structural safety. Two key parts of SHM are sensing networks and structural damage assessment.

SHM required a very large number of sensors distributed throughout the structure and collecting data continuously during the service life of the structure. Common SHM sensors are nondestructive and attached to the structure as external equipment, like ultrasound, X-ray, strain gauge, accelerometer and camera. This dissertation study will mainly focus on detecting structural vibrational responses and the use of various sensors will be introduced.

The goal of SHM is to identify damage through sensor measurements, damage identification can be classified into four levels (Rytter 1993): (1) detection, (2) localization, (3) quantification, and (4) prediction of future damage (damage prognosis). The focus of this dissertation is to reach the localization and quantification levels, in which information regarding the location and servility of damage will be estimated. The prediction level (4) is generally associated with the fields of structural design, fracture mechanics, fatigue life analysis, or structural design assessment and, as therefore is not addressed in this dissertation.

1.4 Environmental Control

Environmental control (EC) is designed to condition building environments (*e.g.* illumination, thermal comfort, air quality and sanitation) for occupant's comfort. Research shows that the buildings' environmental conditions have a significant impact on occupants' health and productivity (Loftness *et al.*, 2003).

Buildings are the largest consumers of energy in the United States and accounts for 36% total energy use (Figure 1.3). Heating, ventilating, and air-conditioning (HVAC) systems account for 39% of the energy used in commercial buildings (EPA, 2015). With continually increasing demand on the limited fossil fuel resources and that the impacts of global climate change are becoming more evident, it is essential to find ways to reduce energy load, increase efficiency, and maximize the use of renewable energy sources. Improving the energy performance of building is vital to achieve this because energy efficient EC systems require less energy and emitting less pollution to the environment while maintaining desired indoor comfort for occupants.

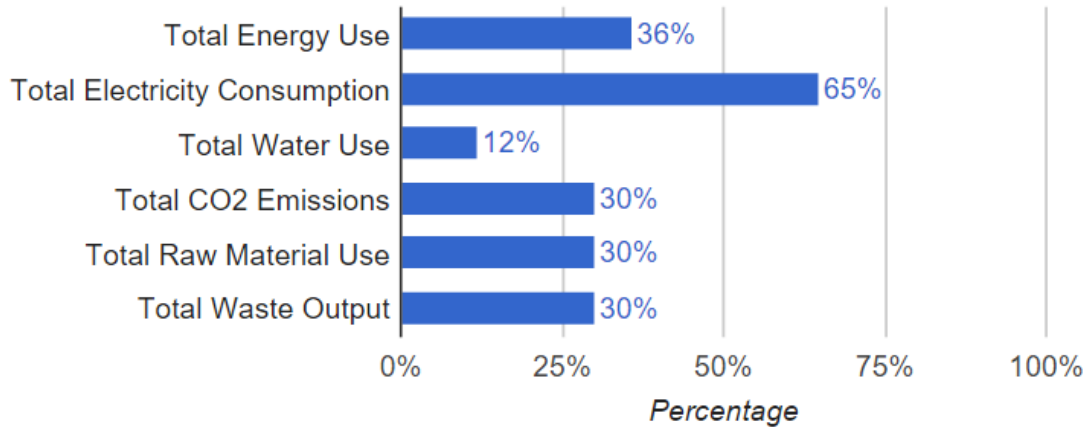


Figure 1.3: Impact of building energy consumption in the United States (source: WBDG, 2015).

Smart EC systems equipped with sophisticated sensing and control devices are increasingly popular to save building operation cost and make buildings more sustainable compared to conventional buildings. Smart systems can manage lighting, temperature, and ventilation in automatic manner which revolutionized building management systems. In order to achieve automation, smart buildings are also to sense and process information on their building environmental conditions for adjusting their control strategies.

Cost is a major concern for EC, especially with a network of sophisticated sensors and controllers. The initial installation cost of a smart EC system is usually much higher compared to the annual building operation cost, which may make developers choose cheaper but less effective EC systems. This is shortsighted because, with the advancement of structural technology, buildings built nowadays are expected to last a very long time. Additionally, many older buildings' lifespans are prolonged with retrofits because retrofitting them is often more cost-effective than building a new facility. Factoring in the length of building lifespans, long term savings of a better performing EC system can surpass the extra initial cost after years of operations.

1.5 Outline for the research

This dissertation targets three aspects for buildings: structural control (SC), structural health monitoring (SHM) and environmental control (EC). SC aims to control structural response, and to prevent or minimize structural damage under extreme events (e.g., strong winds and earthquakes). SHM, on the other hand, checks the integrity of the structure throughout its life cycle and after major events (e.g., wind storms, earthquakes and fire). Other than identifying unsafe structures, SHM systems can also detect structural damage and call for further investigations and repairs. Regarding building environments, EC provides necessary occupant comfort and good EC systems would do so efficiently by minimizing energy usage and harmful emissions.

In this dissertation, the double skin façade (DSF) damper system is first introduced in Chapter 2. The DSF damper system is a smart building system integrating SHM, SC and EC. The energy impact of the DSF damper system is discussed in Chapter 3. In the structural control study, both passive and active control strategies are considered on the DSF damper system. Chapter 4 focuses on the passive control strategies using a six-story shear building model under earthquakes excitations. Chapter 5 investigates the active control strategies using wireless sensing for feedback. Since the active structural control system introduces sensor networks and actuators to the building, Chapter 6 also explores utilizing them for SHM purposes. Finally, given that current SHM sensing systems are often complex and costly, a study using a network of smartphones is investigated in Appendix as an alternative SHM sensor network to reduce installation cost.

Chapter 2. The Double-skin façades mass damper system

This chapter introduces a smart building system by combining double skin façades and mass dampers, the background of the Double-skin façades (DSF) and the Mass Damper is first illustrated, then the integrative system is proposed.

2.1 Double Skin Façade

Double-skin façades (DSF) started to emerge from 1980's. The Occidental Chemical Center (1981) building in Niagara Falls, New York is widely recognized as the first modern DSF (Michael and Harris, 2002). In common DSF systems, a DSF is an envelope system sealed with two glass skins with ventilation openings near the bottom and top of the façade system. As illustrated in Figure 2.1, the air cavity between the two skins could be ventilated naturally (buoyancy driven) and/or mechanically (Saelens, 2008). Compared to a single glass skin system, this system is more insulating and its cavity allows airflow to help ventilate a building.

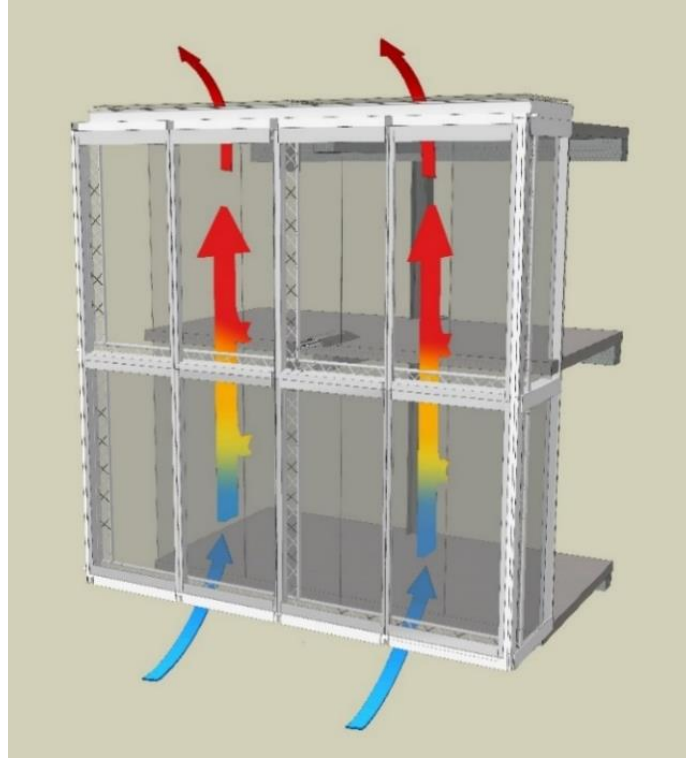


Figure 2.1: A typical double skin façade.

Compared to a single glass skin system, this system is more insulating and its cavity allows airflow to help ventilate a building. The following aspects are common factors considered by architects to incorporate DSF into their designs:

- The aesthetic for all glass façade
- Daylight saving from transparency of the façades
- Improved acoustical insulation
- Improved indoor environment
- Efficient solar shading from outer skin or shading devices within cavity
- Improved energy efficiency through optimized ventilation strategy in different seasons

or climates

However, there are disadvantage with the DSF systems. The major drawback of double-skin façades system is its complexity. In addition, façade layer the increased cost and weight compared to traditional curtain wall systems.

2.2 Mass Dampers

A mass damper is a secondary mass attached to the primary structure that is designed to affect (reduce) structural motions. One of the most common mass damper system is the tuned mass damper (TMD). A TMD can only suppress the response of a primary system in narrow frequency band and, therefore, is ineffective for excitation in other frequency ranges. Thus, a multiple tuned mass damper (MTMD) system was introduced to increase the robustness by tuning MTMDs to wider frequency bands. Igusa and Xu (1994) and Yamaguchi and Harnpornchai (1993) first proposed a MTMD to compensate for the sensitivity of a single TMD to the uncertain natural frequencies of the building system. The MTMD was later extensively studied by Abe and Fujino (1994) and Kareem and Kline (1995). Most of these other 1990s studies concentrate the multiple dampers in one floor or use just a single degree-of-freedom (DOF) model of the primary system (e.g., Li, 2000; Li, 2002; Zuo and Nayfeh, 2005); some other research has had dampers on several floors of a multistory building (e.g., Bergam *et al.*, 1989; Chen and Wu, 2001). In contrast, the proposed DSF damper system herein has dampers in all floors because the DSF covers the building surfaces and is structurally supported throughout the building. Previous work by the authors (Fu and Johnson, 2011) includes a distributed mass damper system that also places mass dampers in all floors of a building. However, the DSF damper system is different than the author's previous work because the DSF dampers connected multiple floors, coupling the motions of several floors. Figure 2.2 illustrates the difference between the single TMD, a single-floor MTMD, the distributed mass damper system and the proposed DSF damper systems. Moon (2009) first proposed the idea using a double skin façade (DSF) as a mass damper. In that study, the author showed vibration reduction by modeling the

primary structure as a single DOF system and the DSF damper as the 2nd DOF element. By modeling the overall system as a 2DOF system, Moon’s model is the most basic TMD system. There are some weaknesses to that model. First, it is not applicable to typical buildings with DSFs where the primary structure is generally a multiple DOF system. Second, because the DSF covers all exterior surfaces of a building, multiple dampers are required to connect the façade system throughout the building as shown in Figure 2.2. This dissertation investigates these issues by formulating a multiple DOF structural model with multiple dampers connecting the DSF. Another similar system is Obayashi Corporation’s “Hula” mass damper (Obayashi, 2012). In the Hula concept system, the outer walls of the building are attached with dampers. This system is similar to a configuration of the DSF system in this study: when the entire DSF is considered rigid and a single mass damper. However, given that a rigid single DSF damper (spanning the entire height of a building) is unpractical for tall buildings, in contrast, the recently proposed DSF system (Fu and Zhang 2016) herein has configurations of multiple DSF dampers.

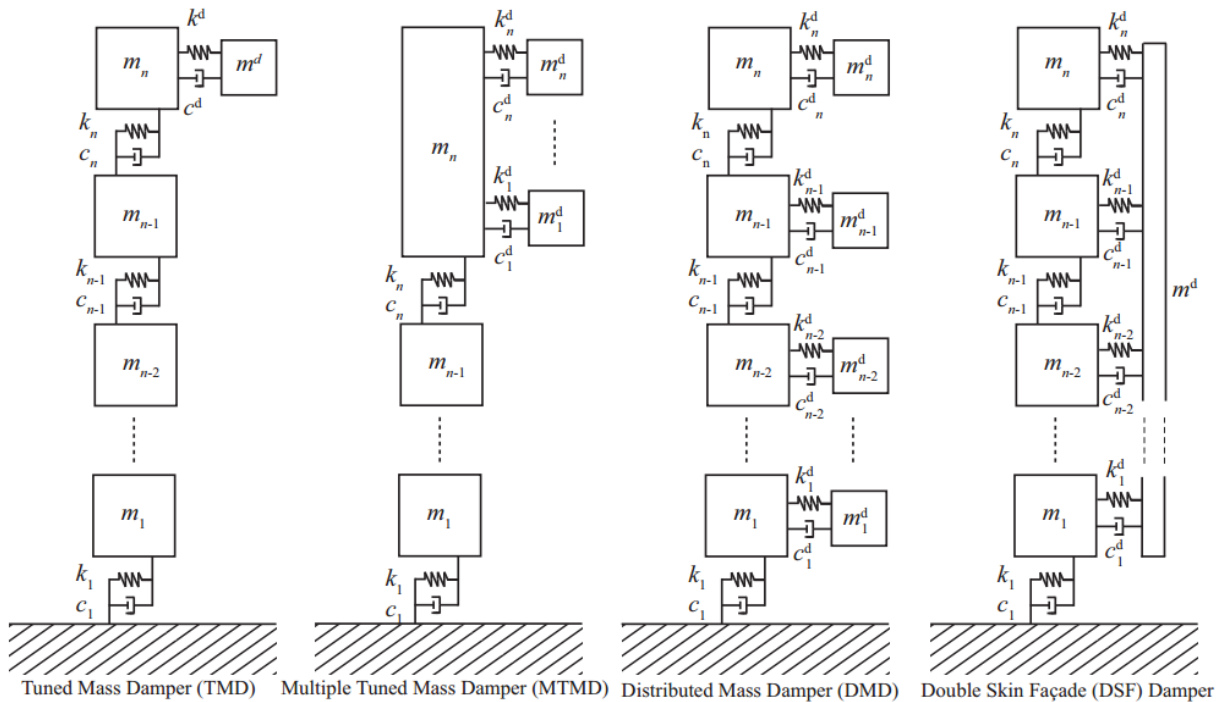


Figure 2.2: Mass damper systems.

2.3 The DSF mass damper system

The double skin façade (DSF) damper system is proposed by combining double skin façades and mass dampers (Figure 2.3). The proposed system adds mobility to the outer façade, making serve as mass dampers. As shown in Figure 2.4 and Figure 2.5, the outer façade is attached to the primary building with a rail system consist of bearings, dampers and actuators. Using façade systems as mass dampers can eliminate the need to add extra mass (i.e., separate mass dampers) to the structure. In terms of energy efficiency, the added mobility of façades (to damp vibrations) can lead to innovative ways to adjust airflow and environmental conditions in the building. Additionally, the actuators controlling the movements of the DSF dampers will be studied to excite the structure for SHM.

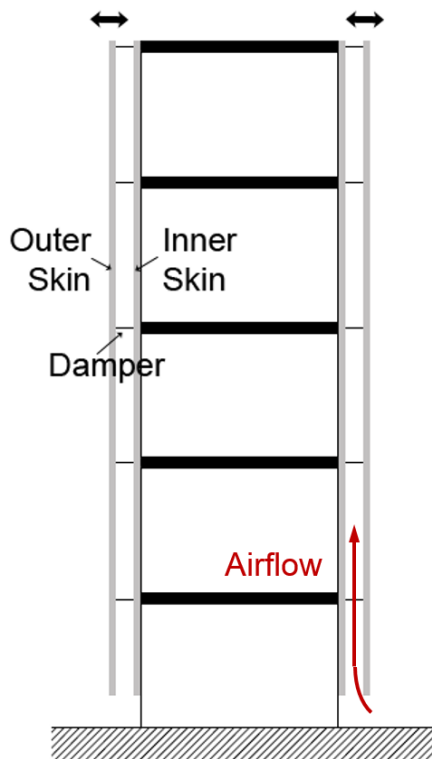


Figure 2.3: Double skin façade (DSF) damper system; the outer skin moves as a mass damper.

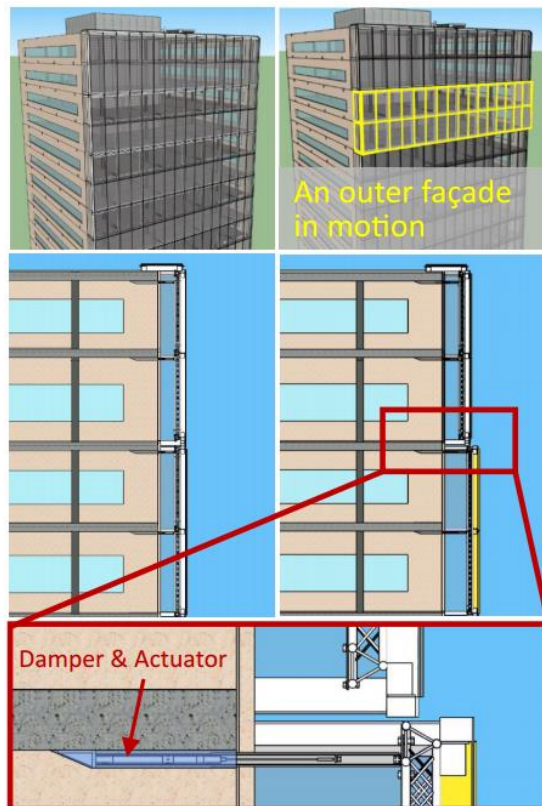


Figure 2.4: Motions of the movable double skin façade system.



Figure 2.5: Details of the connections between the primary building and the movable façade: the wide flange rail system is attached with bearings, dampers and actuators to allow and control linear motions.

DSF are traditionally stationary, but the movements for mass dampers mobilize the façade system and offers novel methods to reduce building energy consumptions. By moving the outer skin, the cavity between the two skins can be adjusted according to internal building conditions (heating/cooling needs) and external conditions (outside temperatures, wind conditions, etc.). In a typical building, HVAC (heating, ventilation, air conditioning) systems typically draw the largest amount of energy compared to other building functions. Given that cavity size influences cavity airflow and the insulating effectiveness of the façade system, the movable DSFs affords an efficient way to regulate temperatures and ventilation in the building. Different control strategies of DSF systems in cooling and heating seasons will be investigated in Chapter 3.

The proposed DSF damper system is an interesting and challenging structural system. Given that the DSF covers all exterior surfaces of a building, multiple dampers are required to connect the façade system throughout the building. Figure 2.2 illustrates the difference between the proposed DSF damper systems comparing to the single TMD, a single-floor MTMD, and the distributed mass damper system. The motions of multiple dampers are coupled because they are connected to the same DSF system. This coupled multiple damper system is more difficult for engineers to design due to the coupling effect and the various locations of individual dampers, but can be less disruptive for architectural design because there is no additional bulky damper masses in the building. Since the façade system is heavy, the proposed DSF damper system can be more massive than traditional mass damper system. Configurations of multiple DSF dampers are studied and compared to the traditional single mass dampers, passive and active control strategies are studied in Chapter 4 and Chapter 5, respectively. In addition, the actuators installed in the DSF damper system also studied in Chapter 6 to excite the structure for SHM purposes.

The system targets improving building sustainability in terms of structural safety and energy efficiency by combining Structural Health Monitoring (SHM), Structural Control (SC) and Environmental Control (EC) systems. The synergy of the integrated system comes not only from its individual functions but also its utilization. Structural control systems are used only during the infrequent recurrence of strong motions, while environmental control systems are in constant use to provide continuous comfort for building occupants. This integrated system would perform environmental control most of the time and switch to structural control when needed, thus providing a synergistic dual-purpose system to improve building energy efficiency and enhance structural and life safety.

Chapter 3. Energy control with DSF damper system

3.1 Heat Dynamics in DSF

In common DSF systems, a DSF is an envelope sealed with two glass skins with ventilation openings near the bottom and top of the façade system. Two major factors that DSF affect building energy consumptions are stack effect and greenhouse effect. As illustrated in Figure 3.1, when solar radiation strikes the external glass skin, it largely passes straight through the external glazing because glasses have a high transmittance to shortwave (solar) radiation. A portion of the solar radiation is absorbed by the glass skin and cause the glass to be heated. After crossing the external skin, the solar radiation first heat up the air in the cavity between the two glass skins then passes through the second glass skin to enter the building. Again a portion of the solar radiation is absorbed by the interior skin. As the cavity gets warm, they (like any warm objects) emit thermal radiation in a long wavelength form. Given that glasses have low transmittance to long wave radiation, the heat is trapped between two glass skins and, thus, amplify the heat gain in the cavity. The process of glass trapping solar heat gain is called the greenhouse effect.

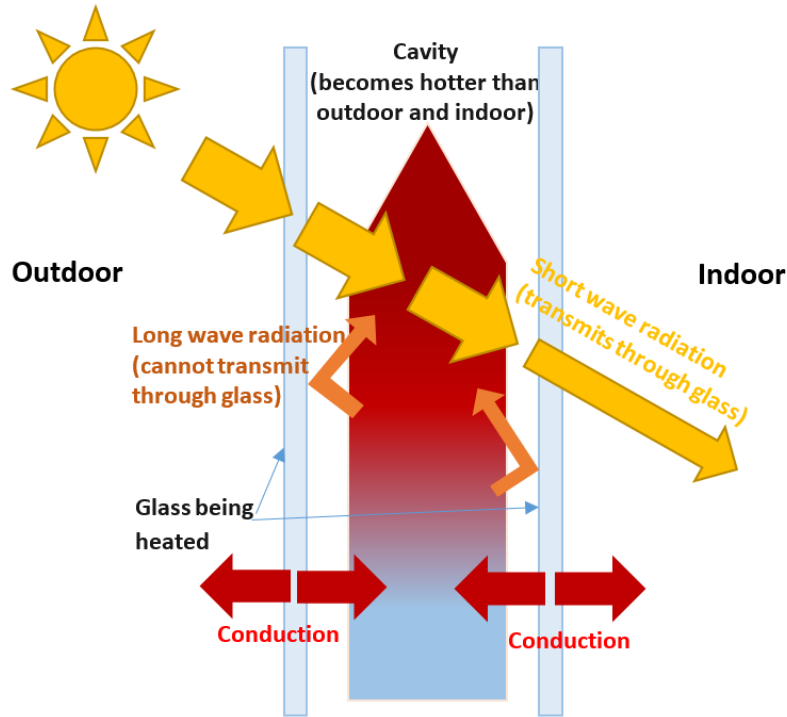


Figure 3.1: Heat Transfer in DSF

In DSF systems, there is another natural effect that influences the heating and cooling aspects: the stack effect. In a tall space, hot air rises to the top of the space because it is lighter than cold air. At the top of the space, the concentrated hot air creates a higher air pressure compared to the outside air and this higher pressure pushes air outward. The outflows of air on the top of the space forces cooler, denser air to enter from the bottom. The rate of airflow, Q , induced by the stack effect can be computed using:

$$Q = CA \sqrt{2gh \frac{T_i - T_o}{T_i}}, \quad (3.1)$$

where A is the flow area, C is a discharge coefficient, g is the gravitational acceleration, h is the height of the space, T_i is the average inside temperature and T_o is the average outside air

temperature. According to (1), the airflow rate increases in a DSF cavity when the cavity height grows and/or the temperature difference between outside air and air inside the cavity increases.

To date, numerous buildings are built with DSF, mostly driven by its improved energy efficiency and architects' designs. Its complexity and adaptability to different climatic conditions increase the need for careful design. The coupling between thermal dynamics, fluid dynamics and the environment makes modeling a ventilated double skin Façade system an intricate problem, following factors should be considered when simulating a DSF system model: 1) wind and buoyancy-driven airflow through the cavity 2) incident solar radiation, and 3) radiative, conductive, and convective heat transfer through the glazed façades and into the adjacent space (Pappas and Zhai, 2006). In recent years, a number of numerical, experimental and field measurement studies have contributed to a better understanding energy saving aspect of the DSF ventilation systems. This section summarizes some significant findings in this field.

Gratia and Herde (2004) using TAS — a building modeling and simulation software (2009) – to evaluated the natural ventilation of the DSF that is influenced by both buoyancy and wind force. They found that natural ventilation can be achieved in DSF system. Another important characteristic of greenhouse effect was also studied by Gratia and Herde (2007). The result shows that greenhouse effect is achieved if DSF is oriented to the south. Balocco (2004) showed that the ventilation and temperature in the Façade depend on the width of the cavity: the narrower the cavity is, the higher the risk is of façade overheating in summer. Since DSF is a complex problem involving convection, conduction and radiation, computational fluid dynamics (CFD) is often used for detailed analysis, CFD help predict the airflow and plan for an optimal ventilations strategy in DSF system by numerically solving a series equations related to convection, conduction and radiation. Hien *et al.* (2005) investigated energy consumption,

thermal comfort and condensation of DSF systems by using TAS and CFD software. The result showed that a natural ventilation DSF system was able to minimize energy consumption as well as enhance the thermal comfort. Manz *et al.* (2006) studied DSF using a spectral optical and a CFD model and validated with a single story naturally ventilated DSF subsystem through experiments. Stec and Paassen (2005) compared the performance of nine different façade systems for Dutch climate and concluded that the DSF systems were competitive in energy performance. They also stressed DSF should integrate with HVAC system. Hong *et al.* (2013) studied the DSF seasonal energy-efficient strategies and found out that about 12% energy saving could be achieved during the heating and cooling seasons.

3.2 DSF seasonal ventilation strategies

There are different ventilations strategies for DSF systems in cooling and heating seasons. In cooling seasons or summer, outside temperatures are generally higher than indoor temperatures. DSFs are also rapidly heated up by solar radiation and by the greenhouse effect. For providing thermal comfort and saving cooling cost, DSF system can be configured as a thermal chimney (see Figure 2.3 (a)) utilizing its potency of stack effect to remove excess heat in order to avoid overheating (Tascon, 2008; Brunoro *et al.*, 2011; Rahmani *et al.*, 2012).

Meanwhile, during heating seasons or winter, the external temperature is colder than the indoor temperature. A thermal buffer zone (a DSF with sealed cavity without openings) can help insulate the building from the cold outside environments (see Figure 2.3 (b)). The Telus Headquarters building in Toronto and the Occidental Chemical buildings in Niagara Falls and in New York use a static air buffer as an airflow operating method to reduce heating energy

consumption in winter (Boake *et al.*, 2001). As a closed buffer zone, the DSF cavity would be heated up rapidly by absorbing solar radiation and the greenhouse effect. Rooms adjacent to the DSF could reduce heating loads by absorbing heat through the inner skin. Tascon's (2008) study shows that temperature in sealed cavity is 28% higher than ventilated cavity. Researchers stated that 20% to 30% heating energy consumption can be reduced by using a static air buffer during winter (Xu and Ojima, 2007; Gracia *et al.*, 2012).

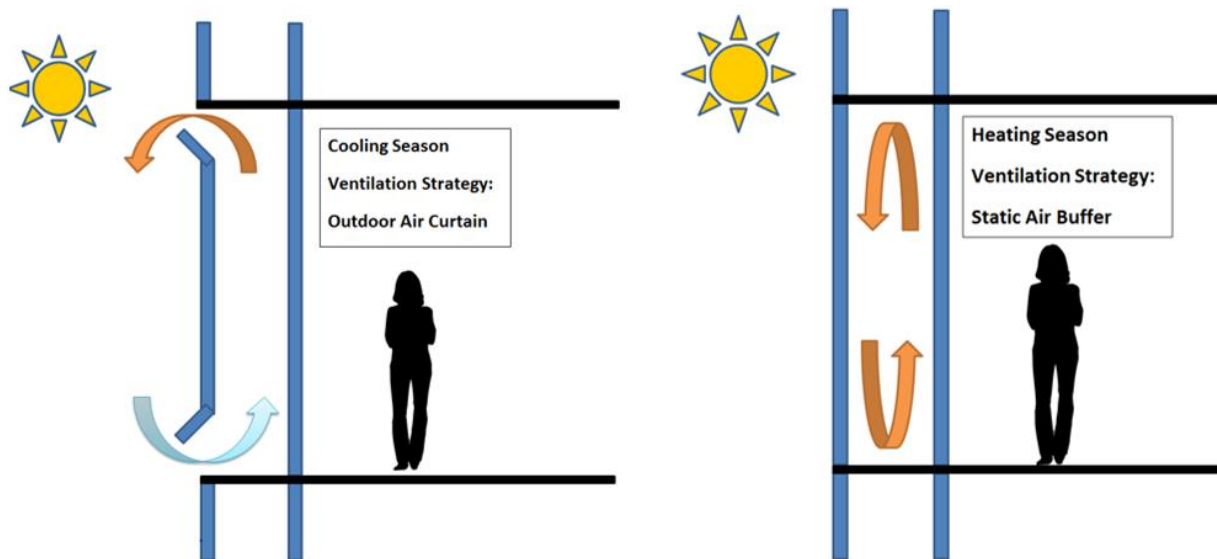


Figure 3.2: DSF ventilation strategy in cooling (a) and heating season (b).

3.3 Energy control with DSF damper system

In the author's proposed DSF damper system, the movements for mass dampers mobilize the façade system and offers novel methods to reduce building energy consumptions. Given that cavity size influences cavity airflow and the insulating effectiveness of the façade system, the movable DSFs affords an efficient way to regulate temperatures and ventilation in the building. In a typical building, HVAC (heating, ventilation, air conditioning) systems typically draw the largest amount of energy compared to other building functions, the adjustable cavity size design also enables different energy efficiencies control strategies in cooling and heating seasons.

In cooling seasons, outside temperatures are generally higher than indoor temperatures, and DSFs are rapidly heated up by solar radiation and the greenhouse effect. In terms of thermal comfort and cooling energy saving, it would be advantageous to ventilate DSF cavities with a large airflow rate to prevent cavity air being overheated. Figure 3.3(a) showed that increases in air change rates would lower cooling loads. Figure 3.3(a) also shows that decreases in air change rates would lower heating loads. During heating seasons, the external temperature is cooler than the indoor temperature; and a thermal buffer zone (such as a DSF with a higher cavity temperature) can help insulate the building from the cold outside environments. Low air change rates would cause cavity temperature to raise (Gratia and De Herde, 2012).

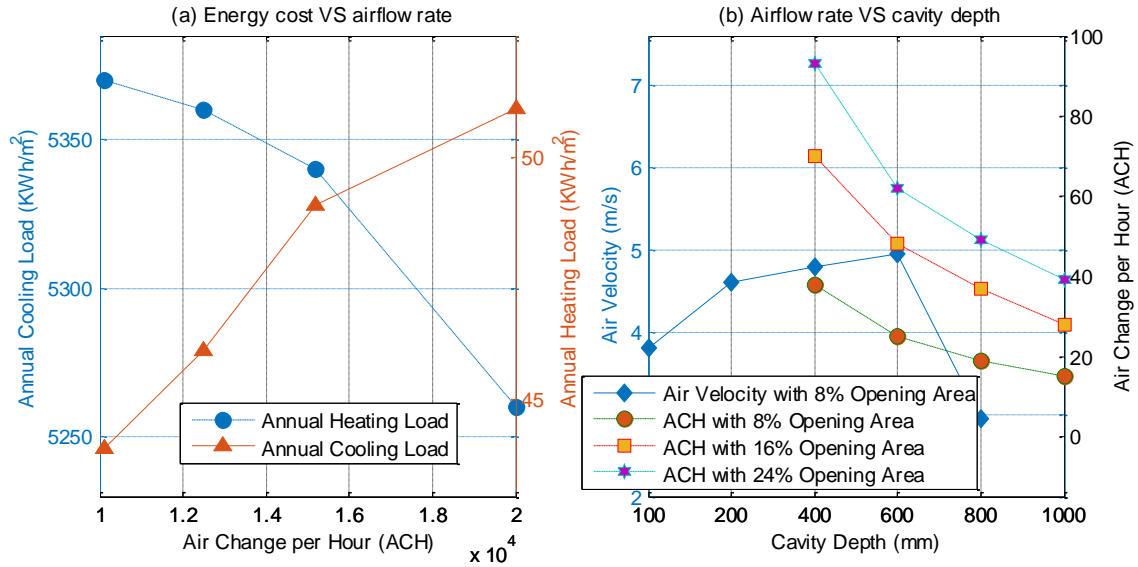


Figure 3.3: (a) Energy cost compared to airflow; (b) airflow compared to DSF cavity depth (source data from Torres *et al.*, 2007 and Tascón, 2008).

Depending on the DSF configurations (*e.g.*, ventilation opening sizes, façade height), there are different depths for each DSF system to achieve fastest or slowest air flow rates. Figure 3.3(b) shows different airflow rate curves for various cavity depths in different DSF configurations (Torres *et al.*, 2007; Tascón, 2008). Large depths are preferred for slow air flow rates that could cause cavity to heat up quickly and decrease heating loads in buildings. To obtain the fastest airflow rates and reduce cooling loads, an optimal depth is desired (*e.g.*, 400-600 mm in Figure 3.3(b)). Tascón showed that airflow was restricted in cavities smaller than the optimal depth while a cavity larger than the optimal depth would form low speed turbulence eddies that decrease the overall airflow. Figure 3.3 shows that cooling and heating seasons demand different cavity depths to reduce energy consumption, highlighting the potential of the proposed movable DSF system in which DSF cavity depths can be adjusted.

Chapter 4. Passive structural control with Double Skin Façade damper system

In previous chapters, the DSF damper system was introduced and has been shown energy reduction in buildings, this chapter illustrates the DSF mass damper system design with passive control strategy. A passive control system was fabricated based on the numerical optimization, then experimented on a scaled six-story structure model. Under seismic excitations, the performance of the passive DSF mass damper system was compared with the traditional TMD and the uncontrolled structure.

4.1 Structural Model and Formulation

The equations of motions for the n -story structure with TMD or passive DSF dampers can be expressed as Equation (4.1),

$$\mathbf{M}\ddot{\mathbf{x}} + \mathbf{C}\dot{\mathbf{x}} + \mathbf{K}\mathbf{x} = -\mathbf{M}\mathbf{1}\ddot{x}_g \quad (4.1)$$

In this equation, \mathbf{M} is the mass matrix, \mathbf{C} is the damping matrix and \mathbf{K} is the stiffness matrix, $\mathbf{x} = [x_1 \ x_2 \ \dots \ x_n \ x_1^d \ x_2^d \ \dots \ x_n^d]^T$, x_i and x_i^d are the i^{th} floor displacement and the i^{th} damper displacement relative to the ground, respectively. \ddot{x}_g is the ground acceleration and $\mathbf{1}$ is a column vector of ones. The difference between the traditional TMD system and the DSF system are illustrated in Figure 2.2, the DSF dampers connected multiple floors while the TMD only connects to the top floor. Table 4.1 compares the equation of motion for TMD system and DSF damper system.

Table 4.1: The equation of motion for TMD system (left column) and DSF damper system (right column).

| TMD | DSF |
|---|---|
| $\mathbf{M} = \begin{bmatrix} [\mathbf{M}_s]_{n \times n} & 0 \\ 0 & m^d \end{bmatrix}$ | $\mathbf{M} = \begin{bmatrix} [\mathbf{M}_s]_{n \times n} & \mathbf{0}_{n \times l} \\ \mathbf{0}_{l \times n} & [\mathbf{M}_d]_{l \times l} \end{bmatrix}$ |
| $\mathbf{K} = \begin{bmatrix} [\mathbf{K}_s]_{n \times n} & -k^d \\ -k^d & k^d \end{bmatrix}$ | $\mathbf{K} = \begin{bmatrix} [\mathbf{K}_{11}]_{n \times n} & [\mathbf{K}_{12}]_{n \times l} \\ [(\mathbf{K}_{12})^T]_{l \times n} & [\mathbf{K}_{22}]_{l \times l} \end{bmatrix}$ |

For both systems, damping matrix \mathbf{C} takes a similar form as \mathbf{K} . Here, m_i and m_i^d are the masses of the i^{th} floor and m_i^d of the i^{th} damper, respectively; k_i and k_i^d are the stiffness coefficients of the i^{th} floor and between the i^{th} floor and the corresponding damper, respectively. For TMD systems, the damper is connected to the top story of the building, the mass matrix and stiffness matrices of the primary structure are as following:

$$\mathbf{M}_s = \begin{bmatrix} m_1 & 0 & \cdots & 0 \\ 0 & m_2 & & 0 \\ \vdots & & \ddots & \vdots \\ 0 & 0 & \cdots & m_n \end{bmatrix}, \quad \mathbf{K}_s = \begin{bmatrix} k_1 + k_2 & -k_2 & 0 & \cdots & 0 \\ -k_2 & k_2 + k_3 & -k_3 & & 0 \\ 0 & & \ddots & & \vdots \\ \vdots & & & -k_{n-1} & k_{n-1} + k_n & -k_n \\ 0 & \cdots & 0 & -k_n & k_n + k^d \end{bmatrix}.$$

For DSF damper systems, the DSF dampers connected multiple floors, coupling the motions of several floors. Consider a multiple DSF damper system with n stories and l dampers where $n = r l$. Here, r is a scalar value, implying that l is chosen to be able to divide n . For example, a six story structure can have three DSF dampers with each damper attached to two floors. This system with evenly divided DSF dampers is selected for simplicity and scalability in simulations.

$$\mathbf{M}_d = \begin{bmatrix} m_1^d & 0 & \cdots & 0 \\ 0 & m_2^d & & 0 \\ \vdots & & \ddots & \vdots \\ 0 & 0 & \cdots & m_l^d \end{bmatrix},$$

$$\mathbf{K}_{11} = \begin{bmatrix} k_1 + k_2 + k_1^d & -k_2 & 0 & \cdots & 0 \\ -k_2 & k_2 + k_3 + k_2^d & -k_3 & & 0 \\ 0 & & \ddots & & \vdots \\ \vdots & & & -k_{n-1} & k_{n-1} + k_n + k_{n-1}^d & -k_n \\ 0 & \cdots & 0 & & -k_n & k_n + k_n^d \end{bmatrix},$$

$$\mathbf{K}_{12} = \begin{bmatrix} k_1^d & k_2^d & \cdots & k_r^d & 0 & 0 & \cdots & 0 & \cdots & 0 & 0 & 0 & 0 \\ 0 & 0 & \cdots & 0 & k_{r+1}^d & k_{r+2}^d & \cdots & k_{2r}^d & & 0 & 0 & 0 & 0 \\ \vdots & & & & & & & \ddots & & & & & \vdots \\ 0 & 0 & \cdots & 0 & 0 & 0 & \cdots & 0 & \cdots & k_{(l-1)r+1}^d & k_{(l-1)r+1}^d & \cdots & k_{lr}^d \end{bmatrix}^T,$$

and

$$\mathbf{K}_{22} = \begin{bmatrix} \sum_{i=1}^r k_i^d & 0 & 0 & \cdots & 0 \\ 0 & \sum_{i=r+1}^{2r} k_i^d & 0 & & 0 \\ 0 & 0 & \sum_{i=2r+1}^{3r} k_i^d & & 0 \\ \vdots & & & \ddots & \vdots \\ 0 & 0 & 0 & \cdots & \sum_{i=(l-1)r+1}^{lr} k_i^d \end{bmatrix}.$$

The corresponding state space representation of Equation 4.1 is

$$\begin{bmatrix} \dot{\mathbf{x}} \\ \ddot{\mathbf{x}} \end{bmatrix} = \begin{bmatrix} \mathbf{0} & \mathbf{I} \\ -\mathbf{M}^{-1}\mathbf{K} & -\mathbf{M}^{-1}\mathbf{C} \end{bmatrix} \begin{bmatrix} \mathbf{x} \\ \dot{\mathbf{x}} \end{bmatrix} + \begin{bmatrix} 0 \\ -\mathbf{1} \end{bmatrix} \ddot{x}_g \quad (4.2)$$

or $\dot{\mathbf{z}} = \mathbf{A}\mathbf{z} + \mathbf{B}\mathbf{u}$, where \mathbf{u} is the system input vector. The output vector $\mathbf{y} = \mathbf{C}_y\mathbf{z} + \mathbf{D}_y\mathbf{u}$ can include, for example, floor drifts, velocities and/or absolute accelerations depending on \mathbf{C}_y and \mathbf{D}_y . For a passively controlled system, \mathbf{u} depends only on the ground acceleration.

4.2 Experimental setup

To check the performance of the proposed DSF mass damper system, a six-story shear scaled model were fabricated to serve as a base structure. Three configurations of the DSF mass damper system and a TMD system were installed on the base structure and tested respectively. This section discusses the experimental structure and the damper mechanisms.

The experimental structure was a six-story shear structure as shown in Figure 4.1. It had a dimension of 0.46 m (18 inches) in length, 0.46 m (18 inches) in width and 1.85 m (73 inches) in height and was mounted on a shake table at the University of New Hampshire. The structure was a metal frame structure consists of four steel columns with rectangle cross sections and six aluminum plates equally spaced to represent floors. Aluminum plates were held by friction using four extra steel stocks at corners to keep the plate perpendicular to the column. Each story had identical height of 30.5 cm (12 inches) and identical weight of 23.8 kg (52.5 lb). The fundamental period was designed to be 0.6 seconds to represent this six-story building structure.



Figure 4.1: The six-story experiment structure.

Double Skin Façade (DSF) damper

Three DSF damper configurations are tested: one-, two- and three-damper configurations as shown on Table 4.2 and Figure 4.2. In the one-damper configurations, the façade spanned and

connected to all six floors and, thus, moved as an entire piece. In the two- and three-damper configurations, each of the DSF dampers spanned three or two floors, respectively.

Table 4.2. DSF mass damper configurations.

| Floor | Number of dampers | | |
|-------|-------------------|------------|------------|
| | 1 | 2 | 3 |
| 1 | | | 1st damper |
| 2 | | 1st damper | |
| 3 | 1st damper | | 2nd damper |
| 4 | | 2nd damper | |
| 5 | | | 3rd damper |
| 6 | | | |

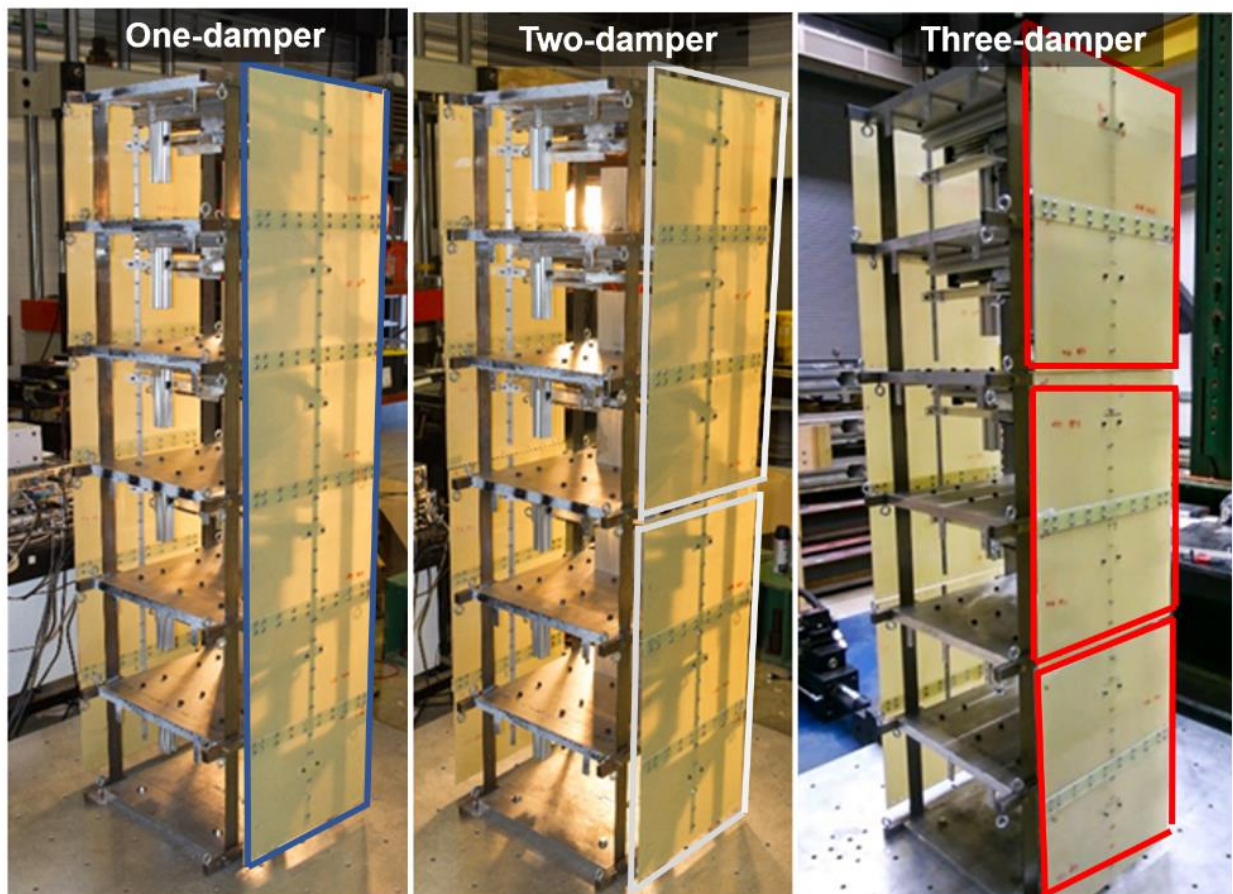


Figure 4.2: DSF damper configurations (picture credit Rui Zhang 2016).

In this experiment, the DSF damper had a 10% damper mass ratio (relative to the primary structural floor mass). Typically, mass damper systems use damper mass ratios less than 2%. This is because that damper masses are kept small to avoid introducing a large amount of extra weight to the structure. In the proposed system, DSFs are part of the existing architectural systems in a building and, thus, are not additional weights to the structure. Building façade systems and their weights can vary significantly from one building to another. Given that they form the entire surfaces of buildings, building façades are heavy, especially in DSF in which there are two layers of glasses and a dedicated support structural system for the outer glass layer. In this study, the DSF dampers account for 10% of the overall structural mass.

Each DSF damper consisted of a two fiber glass panels and served as the movable outer skin of DSF. A set of extension springs and a sliding dual shaft linear guide as shown in Figure 4.3. The fiber glass panels on each side of the building were connected by a horizontal T-bar which attached to the linear guide's movable carriage. The linear guides were oriented along the shake table stroke direction. A pair of extension springs were connected between the T-bar and a set of aluminum frames. The vertical component of the aluminum frame was made adjustable thus different sizes of springs could fit in. In the three-damper configuration shown in Figure 4.2, façades spanned two floors could move entirely as one unit. The weight of DSF damper consisted of the two fiber glass panels, a moving carriage on the linear shaft and a T-bar. The DSF mass damper weighed 2.22 kg (4.91 lb) and was approximately 10% of damper mass ratio (relative to the primary structural mass). The frequency of the damper could be adjusted by using different springs.

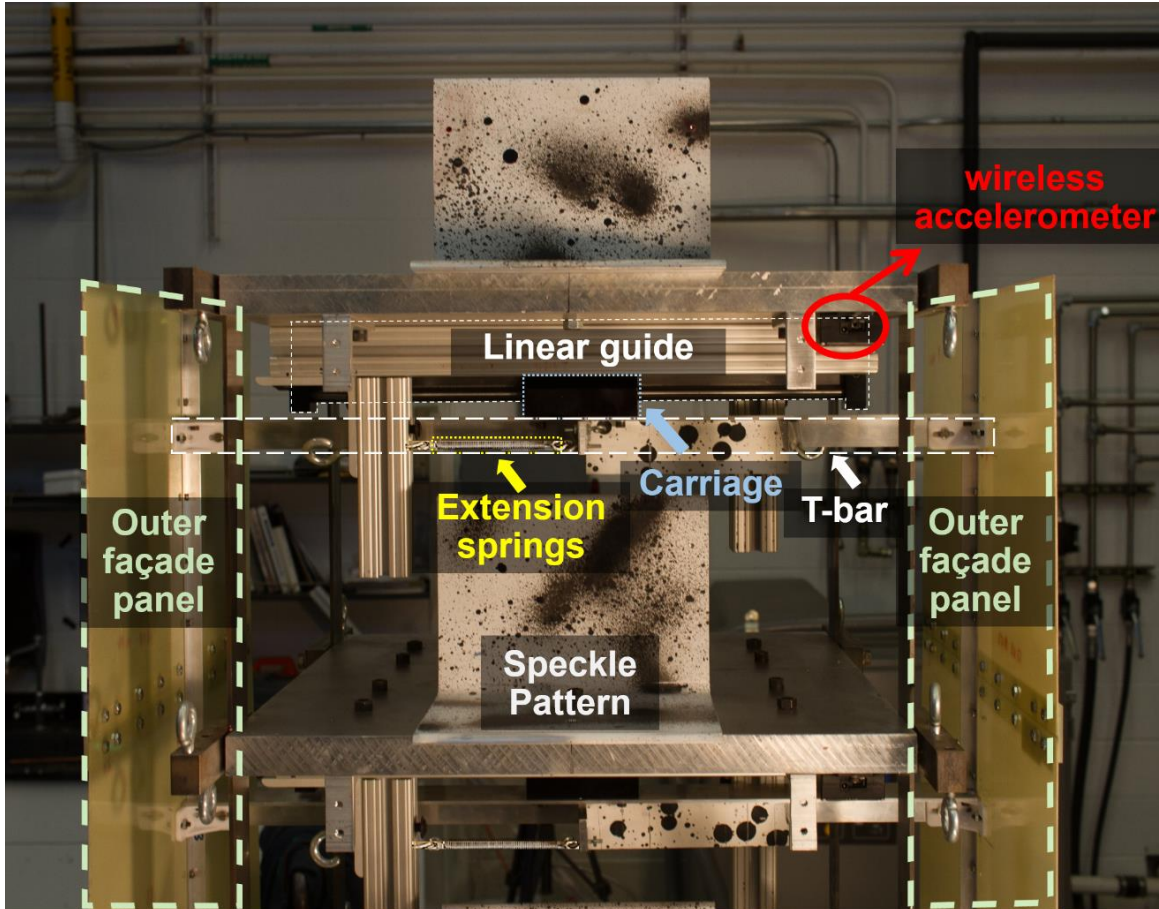


Figure 4.3: Details of the DSF mass damper mechanism (picture credit Rui Zhang 2016).

Tuned mass damper (TMD)

In this study, a single TMD was attached to the top story of the experiment building (see Figure 4.4). The TMD system has the same mechanical component compared to the DSF system except that the façade panels were replaced with equivalent weights (steel stocks) lumped on the linear guide on the structure's top story. The damper mass ratio (10%) of the TMD system was kept the same as the DSF damper system. The frequency of the damper could be adjusted by using different springs. Compared to the DSF system setup, the structure with the TMD had all the static parts of dampers remained on 1st -5th floor, while all the moveable damper mass was removed at those floors. The carriage was locked on the linear guide to prohibit any motion.

Comparisons were made between three cases: 1) an uncontrolled structure enclosed with a static DSF, 2) a structure enclosed with a static DSF and equipped with a TMD on the top floor, 3) a structure with the proposed movable DSF damper system. However, since the façade panels were designed to span multiple floors under the experiment setup, the façade panels had to be removed to avoid coupling multiple floors. To make a fair comparison to the DSF system, equivalent weights of the façade panels were installed on each floor for the TMD and uncontrolled structure as static weights.

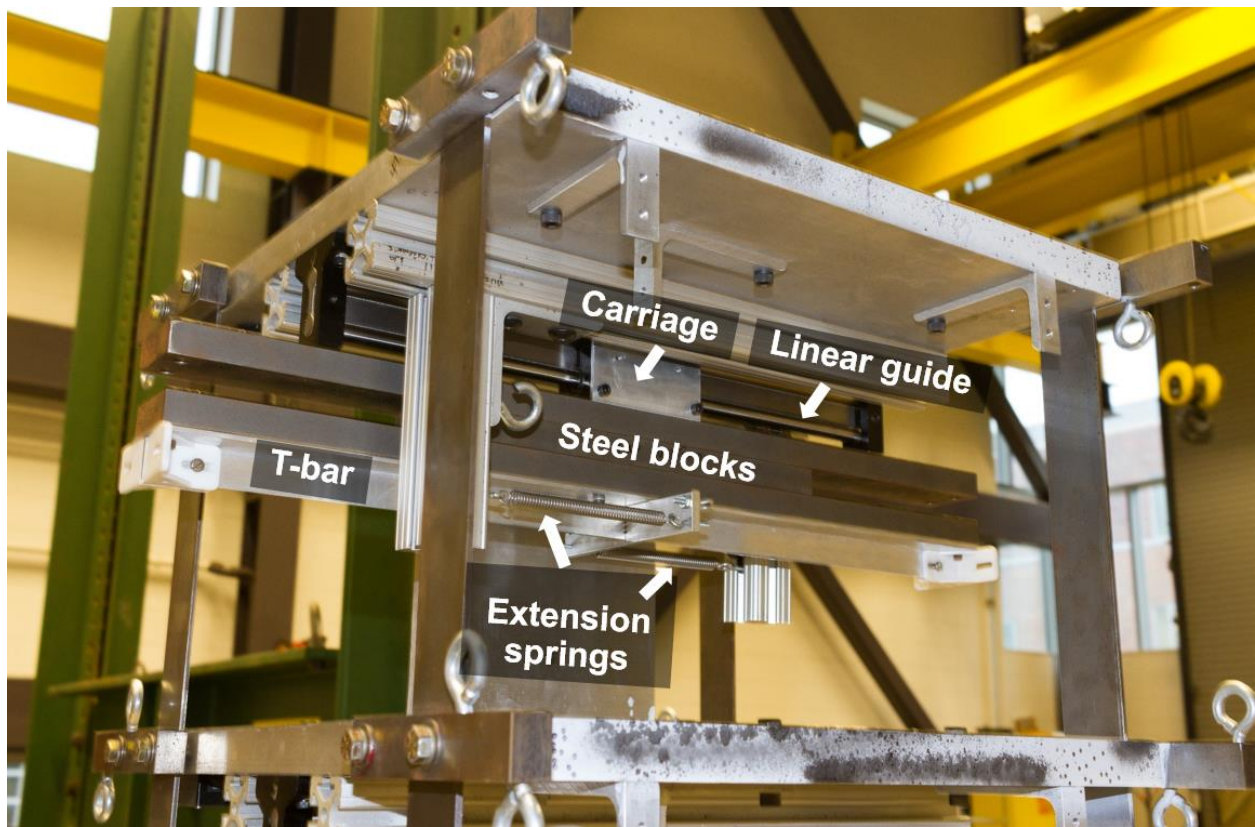


Figure 4.4: Details of the tuned mass damper (TMD).

4.3 Test apparatus

The testing apparatus was a seismic shake table manufactured by MTS Systems Corporation. This shake table (Figure 4.5) consists of a 2.5m × 2.5m aluminum sliding plate and a 97.8 kN (22-kip) linear hydraulic actuator with a 15.2cm (6 inch) stroke. The shake table can be displacement-controlled through an LVDT (linear variable differential transformer). Accelerations were recorded during the testing; six Microstrain® G-Link® -LXRS® wireless accelerometers (2017) were installed on each floor of the building (Figure 4.3). The wireless accelerometers had a 12-bit resolution, ±2 g range and the sampling rate was set to 256 Hz. A Microstrain® WSDA-1000 data aggregator was used to collect the acceleration test data. In addition, floor displacements were measured via digital image correlation (DIC) technique. A target painted with speckle pattern was mounted on each floor (see Figure 4.3), Two Photron® (2017) high speed cameras were placed on the side of structure to track the floor motion at 60 frames per second. The captured frames were processed through DIC software Vic-2D 2009 (2017) to obtain the floor displacements. Inter-story drifts were then derived from floor displacement.



Figure 4.5: Shake table at University of New Hampshire (picture credit Rui Zhang 2016).

4.4 Numerical Simulations for Sizing Experimental Components

To design the DSF damper system under earthquake excitations, parametric studies was conducted on the three DSF damper configurations and on the TMD system (*i.e.*, a single mass damper, with an equivalent damper mass, located on the top story). A numerical model of the structure was built using Equation 4.2. Then the dampers' parameters were optimized through parametric studies. Two types of parametric studies were conducted to determine if extra damping elements needed for experiment. In first parametric study, both stiffness and damping of the damper were optimized. In second parametric study, only the stiffness terms of the damper were optimized and damping is obtained from measurements of dampers.

Dampers' stiffness and damping values are optimized to minimize the sum of the root mean square (RMS) inter-story drifts under the Kanai-Tajimi model of ground motion in Equation (4.3). Global minima were found in the both TMD and DSF systems in minimizing drifts in the 6-DOF structure. A Kanai-Tajimi filter stochastic model (Soong and Grigoriu, 1993) of earthquake ground motion is used as the excitation: a low-pass filtered Gaussian white noise with filter:

$$F(s) = \frac{2\zeta_g \omega_g s + \omega_g^2}{s^2 + 2\zeta_g \omega_g s + \omega_g^2} \quad (4.3)$$

here $\omega_g = 17$ rad/s and $\zeta_g = 0.3$ to approximate the frequency content of four historical ground motions (1940 El Centro, 1968 Hachinohe, 1995 Kobe and 1994 Northridge, Ramallo *et al.*, 2002).

4.4.1 DSF damper system optimization

Optimize dampers' stiffness and damping ratio

For simplicity, in this analysis, the DSF damper stiffness, k_i^d , $i = 1, \dots, 6$, and damping ratio ξ_i^d , $i = 1, \dots, 6$, were assumed identical across the six floors. Given that high stiffness value would cause the DSF dampers to group multiple floors into a single floor, the ranges of these parameters were limited:

Stiffness: $0 \leq k_i^d \leq k_i$; (each damper stiffness must be less than the stiffness of each story)

Damping ratio: $0 \leq \xi_i^d \leq 10 \xi_i^d$; (each mass damper must be less than ten times the damping of each story).

Optimize dampers' stiffness only

Similarly, the DSF damper stiffness values, k_i^d , $i = 1, \dots, 6$, were assumed identical across the six floors in this analysis. The friction between the bearing and the linear shafts was assumed constituted the major damping source of the damper system, the damper's damping terms, ξ_i^d , $i = 1, \dots, 6$, were estimated from experiment setup (Figure 4.6); in which a mass damper system was mounted directly on the shake table and excited by a square wave excitation. The acceleration response of the damper was measure by an accelerometer. Damping ratios of the damper system was estimated using the half-power bandwidth method (Butterworth *et al.*, 2004) and results are listed in Table 4.3. In this parametric study, only dampers' stiffness values were optimized. The ranges of the stiffness are limited:

Stiffness: $0 \leq k_i^d \leq k_i$; (each damper stiffness must be less than the stiffness of each story)

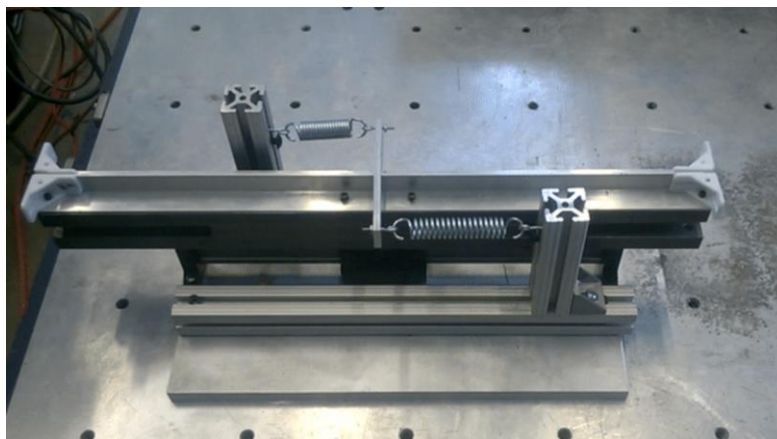


Figure 4.6: Configuration to measure the damping of the linear shafts.

Table 4.3: Measured dampers' damping ratio.

| Floor damper located | Damping ratio ζ (%) |
|-----------------------|---------------------------|
| 1 st floor | 4.78% |
| 2 nd floor | 4.59% |
| 3 rd floor | 3.87% |
| 4 th floor | 4.58% |
| 5 th floor | 5.44% |
| 6 th floor | 2.77% |

4.4.2 TMD system optimization

The damper parameters of the TMD system were also optimized using the two aforementioned parametric study procedures. In the first parametric study, both damper's stiffness and damping terms were optimized. In the second parametric study, the damper's damping ratio value was taken from the damping ratio of the 6th floor damper (2.77% from Table 4.3), thus only the damper's stiffness values were optimized.

4.4.3 Optimization results

Figure 4.7 shows the optimization of damper' stiffness and damping values on the three-damper DSF damper systems and on the TMD system. A global minima can be seen in both systems. Table 4.4 compares the dampers' optimization results of various DSF damper configurations and the TMD system. The optimized stiffness values obtained from the stiffness-and-damping optimization and the stiffness-only optimization were similar, which implied that the global minima of both optimization procedures were numerically less depend of the damper's damping. In other words, damping would not significantly affect the global optimization results

and it would not be critical to optimize the damping values. Therefore, in the experimental setup, the dampers' damping values were based on the measurements listed in Table 4.3. The springs used in experiments were chosen as the approximation of the optimal stiffness values, the springs used in the experiments are listed in Table 4.4 and shown in Figure 4.8.

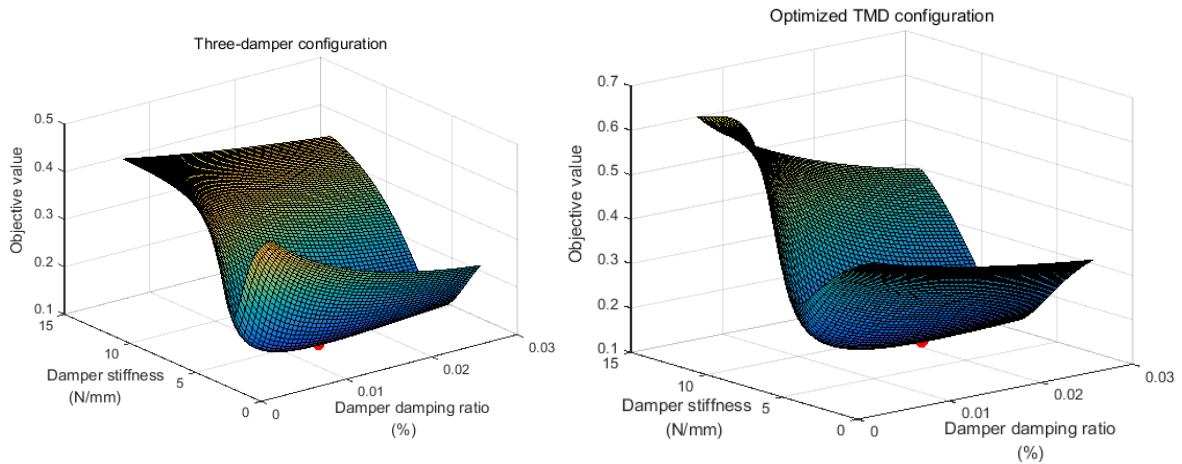


Figure 4.7: Parametric studies to optimize damper' stiffness and damping on three-dampers DSF damper systems (left) and on a TMD system (right) (note: red dots are the global minima in the respective systems).

Table 4.4: Dampers' stiffness used in experiment compared to damping obtained from numerical optimization.

| | Numerical optimized stiffness for each spring (N/mm) | | Spring used in the experiment (N/mm) |
|------------------|--|------------------------|--------------------------------------|
| | Stiffness & Damping optimization | Stiffness optimization | |
| TMD | 0.080 | 0.081 | 0.081 |
| DSF one-damper | 0.016 | 0.014 | 0.016 |
| DSF two-damper | 0.026 | 0.025 | 0.026 |
| DSF three-damper | 0.047 | 0.047 | 0.046 |

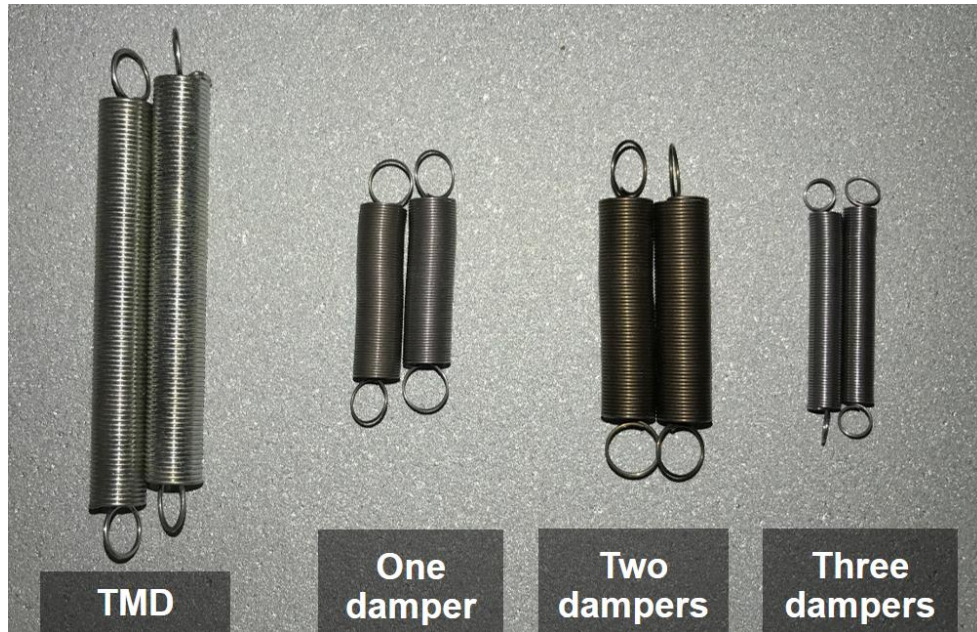


Figure 4.8: Springs used in the experiments.

4.5 Result Discussion

Five experimental test cases (an uncontrolled structure, an optimized TMD system, and three configurations of the DSF damper systems) were performed under five historic earthquake records (*i.e.*, 1992 Erzincan, 1994 Northridge, 1995 Kobe, 1999 Jiji and 2011 New hall). The absolute accelerations at all six floors were measured. Figure 4.9 shows a comparison of the top floor (6th floor) time history acceleration of the uncontrolled, TMD and DSF systems under the Northridge and Jiji earthquakes. The earthquake excitation length was about 2 seconds for the Newhall, 17 seconds for the Erzincan, 30 seconds for the Northridge and 50 seconds for the Jiji. Clearly shown in Figure 4.9, both the TMD and DSF systems reduced significant amounts of vibrations compared to the uncontrolled structure. The structure with the TMD reduced the top-floor vibration by 19.38% under New Hall, 58.17% under Erzincan, 79.80% under Northridge and by 56.60% under Jiji. Meanwhile, the DSF dampers outperformed the TMD by reducing

responses by 83.37% under New Hall, 56.60% under Erzincan, 83.37% under Northridge and by 64.56% under Jiji.

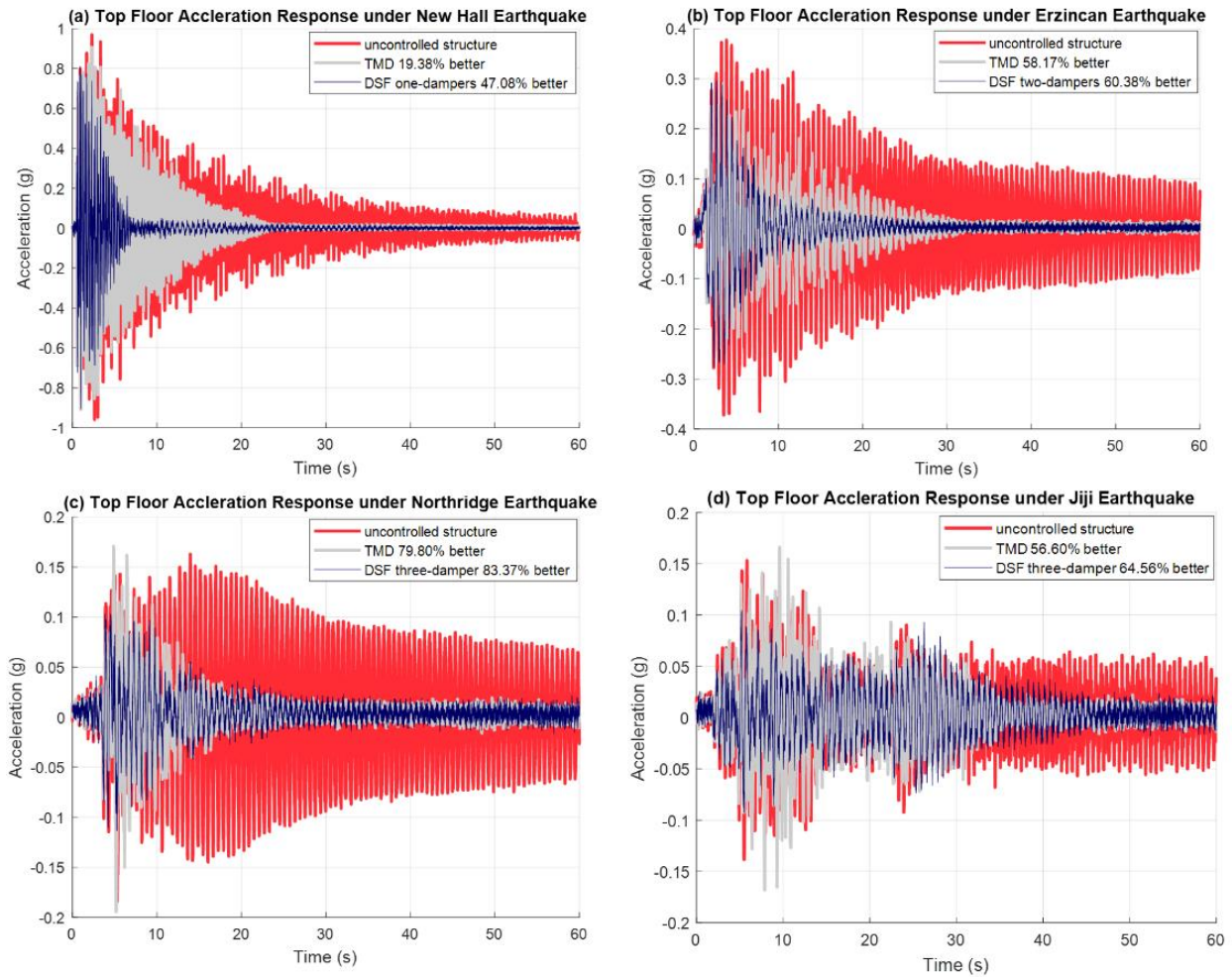


Figure 4.9: Top floor acceleration response of uncontrolled structure, TMD and (a) one-damper DSF system under Newhall earthquake, (b) two-damper DSF system under Erzincan earthquake, (c) three-damper DSF system under Northridge earthquake and (d) three-damper DSF system under Jiji earthquake.

Figure 4.10 Compares the DSF two-damper case to the uncontrolled structure under the Kobe earthquake excitation, as it can be seen from the figure, the displacement outcome of the experiments are closely correlated to the one that simulated. It's also clear from the figure that DSF two-damper case has largely reduced the floor displacement compare to the uncontrolled structure and outperforms the TMD.

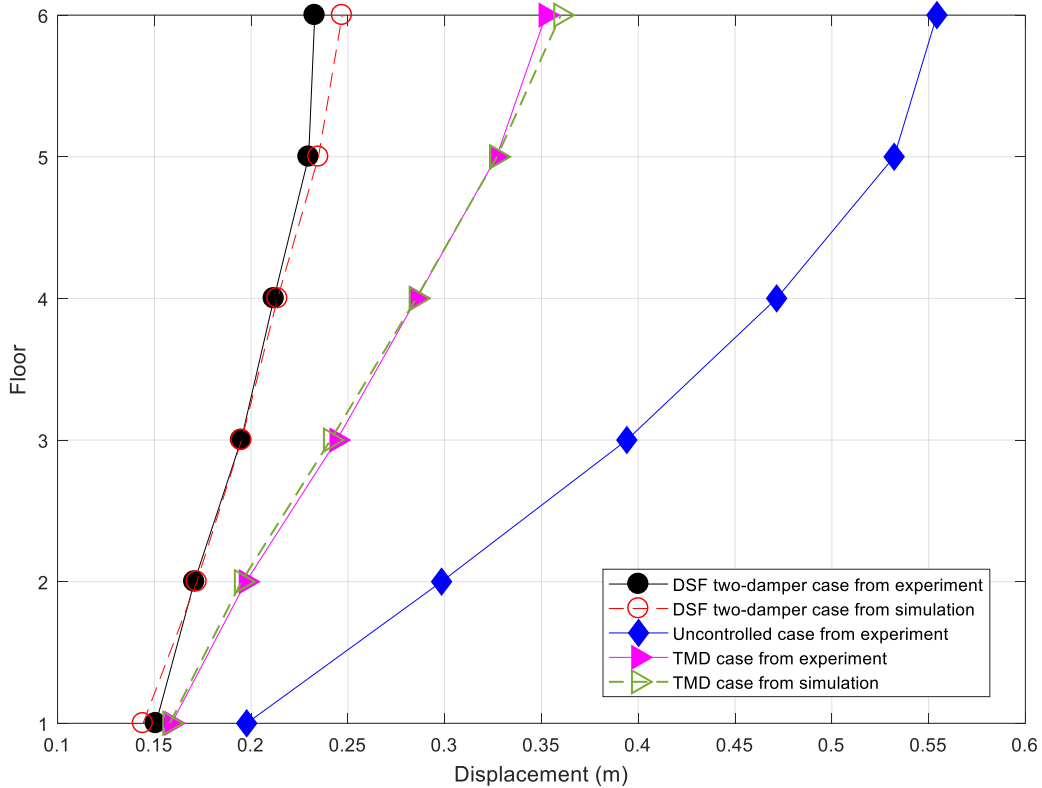


Figure 4.10: Floor RMS displacements under both simulated and experiment tested DSF two-damper case, TMD and uncontrolled structure.

Tables 4.5 and 4.6 show the reduction in both inter-story drifts and acceleration, respectively. Three different DSF damper configurations and a conventional TMD were compared to the uncontrolled structure performed under the five scaled historic earthquake excitations.

Table 4.5: Average RMS Inter-story drift of the DSF damper systems compare to TMD system and uncontrolled structure (RMS: root mean square).

| Excitation | Uncontrolled | TMD | | DSF one-damper | | DSF two-damper | | DSF three-damper | |
|----------------|--------------|-------------|----------------|----------------|----------------|----------------|----------------|------------------|----------------|
| | Drift (mm) | Drift (mm) | Reduct. | Drift (mm) | Reduct. | Drift (mm) | Reduct. | Drift (mm) | Reduct. |
| Northridge | 1.38 | 1.16 | -16.18% | 1.14 | -17.29% | 1.12 | -18.93% | 1.19 | -14.15% |
| Kobe | 1.98 | 1.68 | -15.36% | 1.17 | -53.29% | 1.21 | -51.97% | 1.71 | -31.85% |
| New Hall | 0.85 | 0.65 | -23.12% | 0.48 | -61.71% | 0.49 | -61.10% | 0.52 | -58.04% |
| Jiji | 2.06 | 1.76 | -14.53% | 1.65 | -20.07% | 1.76 | -14.78% | 1.74 | -15.64% |
| Erzincan | 3.20 | 1.96 | -38.78% | 1.24 | -61.30% | 1.24 | -61.22% | 1.12 | -65.03% |
| Average | 1.89 | 1.44 | -21.59% | 1.14 | -42.73% | 1.16 | -41.60% | 1.26 | -36.94% |

Table 4.6: Average RMS acceleration of the DSF damper systems compare to TMD system and uncontrolled structure (RMS: root mean square).

| Excitation | Uncontrolled | TMD | | DSF one-damper | | DSF two-damper | | DSF three-damper | |
|----------------|---------------|---------------|----------------|----------------|----------------|----------------|----------------|------------------|----------------|
| | Accel. (g) | Accel. (g) | Reduct. | Accel. (g) | Reduct. | Accel. (g) | Reduct. | Accel. (g) | Reduct. |
| Northridge | 0.0203 | 0.015 | -26.11% | 0.0126 | -37.93% | 0.013 | -35.96% | 0.0145 | -28.57% |
| Kobe | 0.0875 | 0.0695 | -20.57% | 0.0352 | -59.77% | 0.0371 | -57.60% | 0.0347 | -60.34% |
| New Hall | 0.1146 | 0.0998 | -12.91% | 0.0745 | -34.99% | 0.0754 | -34.21% | 0.0832 | -27.40% |
| Jiji | 0.0406 | 0.0241 | -40.64% | 0.016 | -60.59% | 0.0202 | -50.25% | 0.0181 | -55.42% |
| Erzincan | 0.1349 | 0.1141 | -15.42% | 0.0336 | -75.09% | 0.0333 | -75.32% | 0.0272 | -79.84% |
| Average | 0.0796 | 0.0645 | -23.13% | 0.0344 | -53.67% | 0.0358 | -50.67% | 0.0355 | -50.31% |

As shown in Table 4.6, all DSF damper systems reduced significant amounts of inter-story drifts compared to the uncontrolled structure without any dampers, and the overall performance of DSF outperforms that of the conventional TMD system. Among the DSF configurations, the one-damper configuration was overall the best performing system; and the two-damper configuration was a close second. The one-damper case reduced an averaging 42.73% of inter-story drift and 53.67% of floor acceleration compared to the uncontrolled structure. In terms of the average inter-story drift reduction, the one- and two-damper configurations outperformed the TMD system in all the excitations, while three-damper case outperformed the TMD case in all excitations except Northridge. In terms of the average

acceleration reduction, all DSF damper systems outperformed the TMD system in all five earthquake excitations.

4.6 Conclusion

In this Chapter, an innovative system integrating double skin façades (DSF) and mass damper was analyzed and experimented. The façade damper system was formulated first, then, the damper parameters (stiffness and damping coefficients) were optimized using a parametric study to minimize structural responses under earthquake excitations. Three configurations with one-, two- and three- dampers were optimized and fabricated. Exciting an experimental structure with historical earthquake records, the DSF mass damper system was shown to significantly reduce structural motions. Additionally, the proposed system was shown to mostly outperform a conventional tuned mass damper system with an equivalent damper mass ratio.

Chapter 5. Active structural control with the double skin façade damper system

5.1 Introduction

Active structural control systems aim to actively control building response under extreme events (*e.g.* earthquakes and strong winds) such that buildings can remain safe and serviceable. An active structural control system is a feedback control system which involves sensors, actuators and a digital controller. Under such a system, the sensors measure structure responses of a structure caused by external loads, the controller process the measured data, and the actuators apply feedback forces. Compared to passive structural control systems, feedback control systems offer improved performance over a larger frequency bandwidth and variety of loading cases (Housner *et al.*, 1997).

In recent years, wireless sensors become an attractive alternative to the traditional tethered system for monitoring civil infrastructures due to the wireless sensors' decreasing cost and their ease of deployment (Fu *et al.* 2013). Typical wireless smart sensors include onboard processing, memory, communication, and sensor interfaces. Their onboard capabilities in combination with an actuation interface make wireless sensor networks (WSN) an attractive alternative to tethered systems for control applications as well (Lynch and Loh 2006). However, wireless sensors posing inherent challenges for robustness of the control system including reliability of communication, communication delays and lower sampling rates. Slow sampling rates can negatively affect the robustness and performance of the control system. Lynch *et al.* (2008) explored the effect of slow sampling rates on the robustness of the structural control

system. In their study, two sensing systems (wired at 200Hz and wireless at 12.5Hz) were implemented on a three-story structure with an MR damper on the first story. The smaller sampling rate was largely governed by the on-board calculation of the wireless sensors and time-division multiple access (TDMA) communication protocol. It was shown that the lower sampling rates of wireless sensors led to poor disturbance rejection and less successful mitigating the response of near-field earthquakes using velocity feedback. However, while under acceleration feedback solution, the wireless system was proven equivalent compared to the wired system.

To date, two groups have published successful implementations of using wireless sensors for structural control with active mass dampers (AMDs). Casciati and Chen (2012) implemented an AMD on a three-story steel structure with a centralized control algorithm. The wireless control system achieved comparable performance compared to the wired system subject to sinusoidal excitations. Linderman and Spencer (2016) studied both centralized and decentralized controls for a four-story structure with two active mass dampers and wireless acceleration feedback. The wireless control system achieved performance similar to the wired system; however the lower sampling rate of wireless sensors required careful design to incorporate the latency and time delay of the wireless control system.

The work in this chapter addresses the control design with actuators and wireless sensors using the proposed double skin façade (DSF) mass damper system. The system will use the story acceleration response as feedback measurements for controlling the structure, the controller design will combine a Kalman estimator and a linear quadratic regulator (LQR) control design. Due to the nature of the wireless control system, slow sampling rates and time delay in data transmission require careful control design and hardware selection. This work explores these challenges by first designing and experimentally verifying an AMD system on a single-story

structure. Then the controlled design was applied to a six-story structure with both the DSF damper and AMD systems.

5.2 Controlling a Single-story Structure with AMD

This section evaluates the design of AMD installed on a single-degree-of-freedom (SDOF) structure. This section presents the system model, controller design, and experimental results.

5.2.1 System Model

The test structure is a single-story shear structure. Figure 5.1 shows the experiment configuration. The structure, mounted on a shake table at the University of New Hampshire, had a dimension of 0.46 m (18 inches) in length, 0.46 m (18 inches) in width and 0.30 m (12 inches) in height, and a weight of 23.14 kg (51.01 lb). The structure was a metal frame structure consists of four steel columns with rectangle cross sections and aluminum plates equally spaced to represent floors. Aluminum plates were held by friction using four steel stocks at corners to keep each plate perpendicular to the columns.

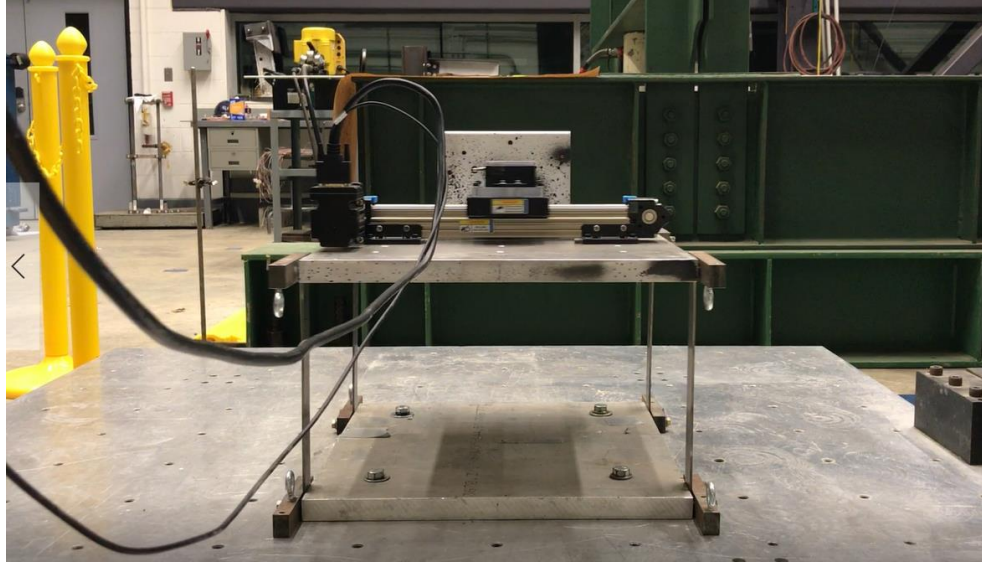


Figure 5.1: The experiment structure.

The AMD system consisted of a single-story building-like structure with a controllable linear actuator on top (as shown in the Figure 5.2). The actuator was a belt driven uniaxial module (W45-15) made by CCM Automation Technology (CCM, 2017). The carriage of the actuator was driven by a programmable Moog Animatics SmartMotor (SM23165D) that moved along the actuator rail (the same direction as the ground motion input generated by the shake table). SmartMotor was a high performance and highly programmable brushless D.C. servomotor; it integrated servo motor system integrated with a motor, an encoder, an amplifier, a controller, serial communication (Moog Animatics 2017). The SmartMotor featured a tunable PID (Proportional, Integral, Derivative) controller that updated at 8,000Hz. Based on the loading condition, the PID would direct the amplifier to give the motor as much current as required to stay on the trajectory. By connecting the motor to the actuator, the rotational motion of the motor shaft transformed into to the axial motion of the actuator cart.

A Microstrain G-Link-LXRS (2017) wireless accelerometer node were installed on floor of the structure. The wireless accelerometers had a 12-bit resolution and a ± 2 g range, and the sampling rate was set to 64 Hz. A WSDA-102 serial interface data aggregator was used to collect the acceleration data.

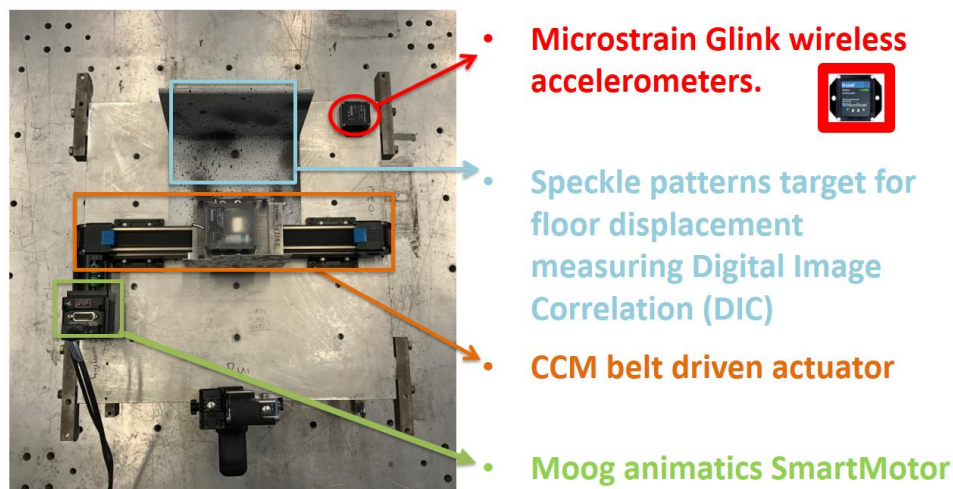


Figure 5.2: Hardware used in the experiment.

The consistency of timing is crucial for controllers used for real-time feedback control purposes. The digital controller used in this study was the LabVIEW Real-Time Module. A desktop personal computer (PC) was converted to a deterministic deployment target running on LabVIEW Phar Laps ETS real-time operating system. The real-time (RT) operating system had the ability to prioritize tasks so that the most critical task could always take control of the processor when needed, guaranteeing reliable predictable and execution (National Instrument 2017). In this study, the control algorithm was executed on the target machine. The real-time system could guarantee the full cycle of control that included collecting and parsing acceleration data, calculating the control gain, and sending out command to drive the motor during a sampling period. The host PC connected to the target PC via an Ethernet cable which allowed the

host PC to monitor the data from the real-time target. The serial input-output interface was on the target machine and ran on the real-time system to collect acceleration data and send commands to the motor via serial connections.

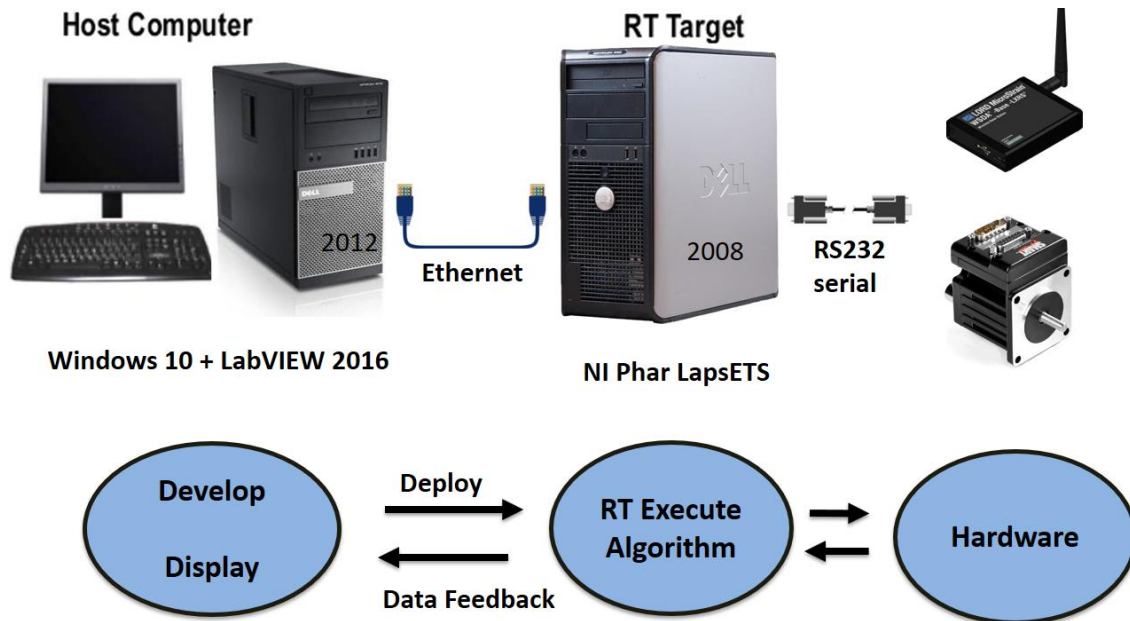


Figure 5.3: Illustration of the real-time (RT) system.

In the single-story experimental configuration, the mass damper weighed 2.67 kg (5.89 lb) and had approximately a 10% damper mass ratio (relative to the primary structural floor mass). The dampers' physical properties (stiffness and damping values) were identified from experiments. As shown in Figure 5.4, a floor plate with an AMD system was mounted directly on the shake table. An open-loop unit torque pulse was applied by the motor to excite the damper and the acceleration response of the damper was measure by a wireless accelerometer installed on the cart. Stiffness and damping properties of the damper system was estimated using a half-power bandwidth method (Butterworth *et al.*, 2004). Similarly, the physical properties of the primary structure was identified through acceleration response excited by the impulse torque by

the actuator. Table 5.1 summarizes the identified physical properties of both the primary structure and the mass damper.

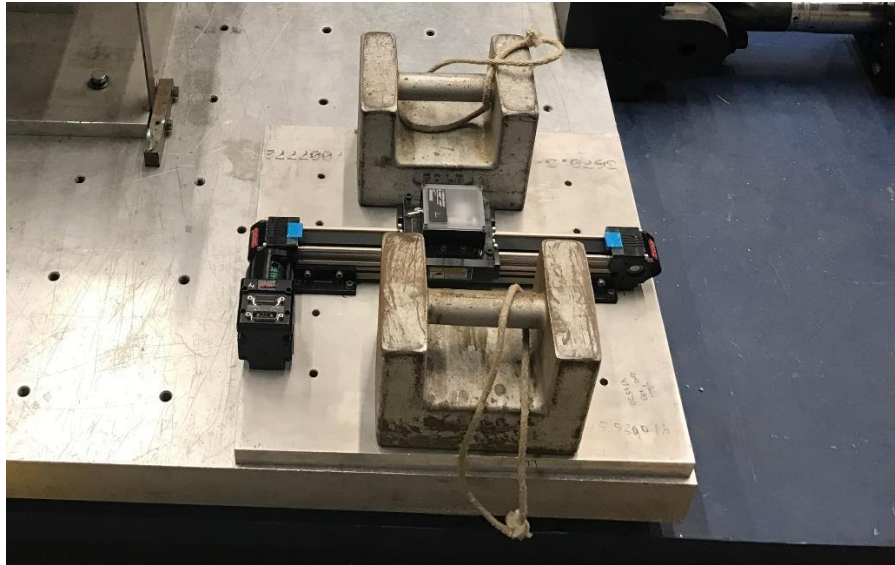


Figure 5.4: Experiment configuration to measure the stiffness and damping properties of the actuator.

Table 5.1: Identified physical properties estimated from the experiment

| | Natural Frequency (Hz) | Stiffness (N/m) | Damping ratio |
|-------------|------------------------|-----------------|---------------|
| Structure | 6.92 | 50533 | 0.0153 |
| Mass damper | 14.69 | 19739 | 0.4362 |

5.2.2 Controller Design

The controller in this study is an acceleration feedback close loop control system. Acceleration measurements can be reliable and inexpensive, and oftentimes used in feedback control of civil structures (Dyke *et al.* 1996, Spencer *et al.* 1998). In this study, acceleration from wireless sensors is used as partial state feedback, a Kalman estimation combined with the linear quadratic regulator (LQR) is used to determine the appropriate control force for the active DSF system. A block diagram of the complete closed-loop system is given in Figure 5.5.

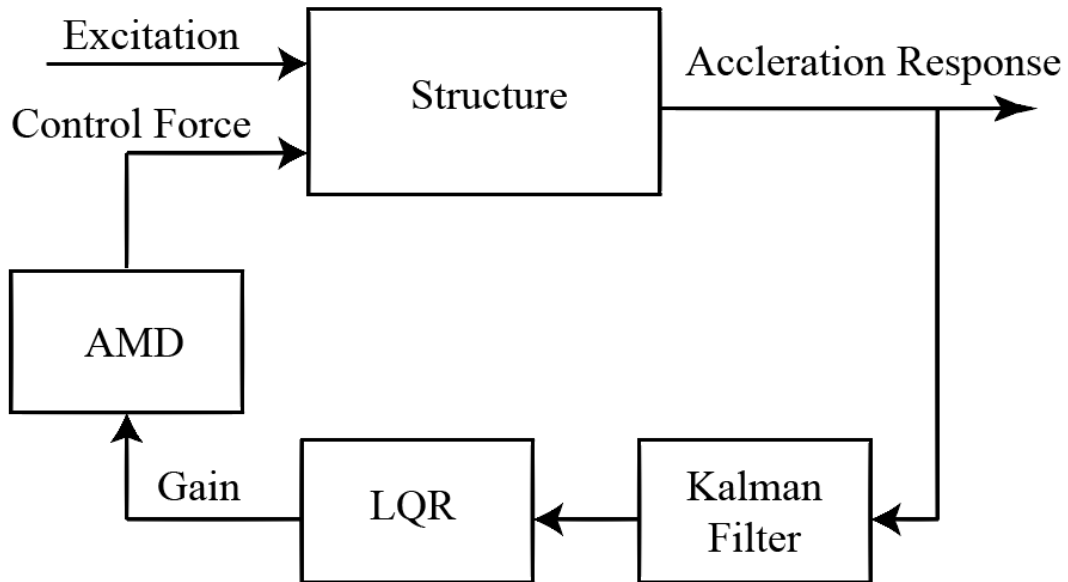


Figure 5.5: Block Diagram of the Active Feedback Control System

The equations of motions for an n -story structural with an active control damper can be expressed as:

$$\mathbf{M}\ddot{\mathbf{x}} + \mathbf{C}\dot{\mathbf{x}} + \mathbf{K}\mathbf{x} = -\mathbf{M}\mathbf{1}\ddot{x}_g + \mathbf{f} \quad (5.1)$$

The state space representation of (5.1) is

$$\begin{bmatrix} \dot{\mathbf{x}} \\ \ddot{\mathbf{x}} \end{bmatrix} = \begin{bmatrix} \mathbf{0}_{n \times n} & \mathbf{I}_{n \times n} \\ -\mathbf{M}^{-1}\mathbf{K} & -\mathbf{M}^{-1}\mathbf{C} \end{bmatrix} \begin{bmatrix} \mathbf{x} \\ \dot{\mathbf{x}} \end{bmatrix} + \begin{bmatrix} \mathbf{0}_{n \times n} \\ \mathbf{M}^{-1}\mathbf{B}_c \end{bmatrix} \mathbf{u} + \begin{bmatrix} \mathbf{0}_{n \times l} \\ -\mathbf{1}_{n \times l} \end{bmatrix} \ddot{x}_g \quad (5.2)$$

or $\dot{\mathbf{x}} = \mathbf{A}\dot{\mathbf{x}} + \mathbf{B}\mathbf{u} + \mathbf{E}\ddot{x}_g$, where \mathbf{u} is the system input vector, \ddot{x}_g is the ground displacement of the earthquake and $\mathbf{1}$ is a column vector of ones, \mathbf{f} is the controlled force introduced by the actuators and \mathbf{u} is the output acceleration from the motors.

The output of the state space equation can be written as:

$$\mathbf{y} = \mathbf{C}_1 \begin{bmatrix} \mathbf{x} \\ \dot{\mathbf{x}} \end{bmatrix} + \mathbf{D}\mathbf{u} + \mathbf{F}\ddot{x}_g \quad (5.3)$$

where \mathbf{y} is the output vector that contains floor displacements, accelerations and/or damper displacements depending on \mathbf{C}_1 , \mathbf{D} and \mathbf{F} .

Linear Quadratic Regulator (LQR) Control

A LQR controller regulates the states of a linear system with a quadratic cost function. The method calculates a feedback gain \mathbf{K} that minimizes the following cost function subject to the system dynamics $\dot{\mathbf{x}} = \mathbf{A}\dot{\mathbf{x}} + \mathbf{B}\mathbf{u}$:

$$\mathbf{J} = \mathbf{E}[\mathbf{y}^T \mathbf{Q} \mathbf{y} + \mathbf{u}_c^T \mathbf{R} \mathbf{u}_c] \quad (5.4)$$

where \mathbf{Q} and \mathbf{R} are response and control weighting matrices, respectively.

The resulting gain, \mathbf{K} , yields the optimal solution to achieve the balance of system response, \mathbf{y} , and control effort, \mathbf{u}_c , based on state feedback $\mathbf{u}_c = -\mathbf{K}\mathbf{x}$. The optimal solution that minimize cost function \mathbf{J} could be found as

$$\mathbf{K} = \mathbf{S}^{-1} \mathbf{B}^T \mathbf{T}, \quad (5.5)$$

where \mathbf{S} is the positive definite solution of the algebraic Riccati equation, given by

$$\mathbf{A}^T \mathbf{S} + \mathbf{S} \mathbf{A} - \mathbf{S} \mathbf{B} \mathbf{R}^{-1} \mathbf{B}^T + \mathbf{Q} = \mathbf{0} \quad . \quad (5.6)$$

Consider the case that \mathbf{y} contains floor displacements and floor accelerations, or

$\mathbf{y} = [\mathbf{y}_{\text{displacement}}^T, \mathbf{y}_{\text{acceleration}}^T]^T$, then \mathbf{Q} can take the following form:

$$\mathbf{Q} = \begin{bmatrix} q_{\text{displacement}} \mathbf{I} & \mathbf{0} \\ \mathbf{0} & q_{\text{acceleration}} \mathbf{I} \end{bmatrix} = \begin{bmatrix} (1-10^a) / (\bar{y}_{\text{displacement}}^{-2}) \mathbf{I} & \mathbf{0} \\ \mathbf{0} & 10^a / (\bar{y}_{\text{acceleration}}^{-2}) \mathbf{I} \end{bmatrix} \quad . \quad (5.7)$$

where $q_{\text{displacement}}$ and $q_{\text{acceleration}}$ are weighting constants related to the floor displacement and floor absolute accelerations, respectively. $\bar{y}_{\text{displacement}}$ and $\bar{y}_{\text{acceleration}}$ are root mean squares of the structural displacements and accelerations, respectively, given by:

$$\bar{y}_{\text{displacement}} = \sqrt{\frac{1}{n} \sum_{i=1}^n (y_{i,\text{displacement}})^2} \quad . \quad (5.8)$$

where $y_{i,\text{displacement}}$ is the displacement response for the i^{th} story, and $\bar{y}_{\text{acceleration}}$ takes a similar form. Meanwhile, \mathbf{R} is only concerned with the control forces and, thus, has a simpler form of $\mathbf{R} = r \mathbf{I}$; a large value of the constant r calls for small control forces and vice versa. By varying \mathbf{Q} and \mathbf{R} , the control forces can be designed for different types of active systems and for different performance levels.

Kalman filter

The LQR design assumes full-state feedback, but full-state responses (*i.e.*, displacement, velocity and acceleration) are usually hard to achieve in the experiments due to the limited

capacity and cost of the sensors. In this study, based on floor acceleration measurements, a Kalman filter is used to reconstruct the full-state response of the system.

Kalman filters are optimal model-based predictor-corrector type estimator that minimize the variance of the estimated error covariance in the presence of Gaussian type process and measurement noise. Although Kalman filters are traditionally derived in discrete-time, a continuous time Kalman filter will be initially presented in the following section and followed by the discrete-time implementation (Stengel 1986).

The design of Kalman augmented common continuous time-invariant plant can be expressed as

$$\begin{aligned}\dot{\mathbf{x}}(t) &= \mathbf{Ax} + \mathbf{Bu} + \mathbf{Gw} \\ \mathbf{y}(t) &= \mathbf{Cx} + \mathbf{Du} + \mathbf{v}\end{aligned}\quad (5.9)$$

where the previous state space equation (5.2) is augmented with process noise, \mathbf{w} , and sensor noise, \mathbf{v} . The matrices \mathbf{A} , \mathbf{B} , \mathbf{C} , and \mathbf{D} in the state space equation are known. \mathbf{w} and \mathbf{v} are assumed to be zero-mean, white noise processes uncorrelated with initial state $\mathbf{x}(0)$ and uncorrelated with each other, the covariance is defined by

$$\mathbf{E}(\mathbf{w}\mathbf{w}^T) = \mathbf{S}_w, \quad \mathbf{E}(\mathbf{v}\mathbf{v}^T) = \mathbf{S}_v \quad . \quad (5.10)$$

Construct a state estimate $\hat{\mathbf{x}}$ that minimizes the steady-state error covariance \mathbf{P} ,

$$\mathbf{P} = \lim_{x \rightarrow \infty} \mathbf{E}\{(\mathbf{x} - \hat{\mathbf{x}})(\mathbf{x} - \hat{\mathbf{x}})^T\} \quad . \quad (5.11)$$

The optimal solution can be found with

$$\dot{\hat{\mathbf{x}}} = \mathbf{A}\hat{\mathbf{x}} + \mathbf{Bu} + \mathbf{L}(\mathbf{y} - \mathbf{C}\hat{\mathbf{x}}) \quad , \quad (5.12)$$

where $\hat{\mathbf{x}}$ is the estimated state, and \mathbf{L} is the steady-state Kalman gain given by

$$\mathbf{L} = \mathbf{P}\mathbf{C}^T\mathbf{S}_v^{-1} \quad (5.13)$$

The error covariance matrix, \mathbf{P} , is positive definite and can be obtained by solving the Riccati equation:

$$\mathbf{A}\mathbf{P} + \mathbf{P}\mathbf{A}^T - \mathbf{P}\mathbf{C}^T\mathbf{S}_v^{-1}\mathbf{C}\mathbf{P} + \mathbf{G}\mathbf{S}_w\mathbf{G}^T = \mathbf{0} \quad (5.14)$$

Tuning of the SmartMotor

The output from the LQR controller is in unit of force while the SmartMotor driving the actuator is a servomotor controlled by displacement. Though direct force control was not achievable in the experiment, control was applied by adjusting the direction and acceleration of the cart (and the attached damper mass) of the linear actuator. A program was developed and embedded in the SmartMotor such that the motor would execute the close-loop control of the shaft rotational acceleration. Upon receiving the incoming serial commands, the SmartMotor would recalculate and react immediately based on the developed program. The master motor was set to the position mode which is a close-loop PID controlled mode based on encoder feedback of the shaft rotational position. The PID parameters — K_P , K_I and K_D — were tuned for the best control performance; the main objective in tuning a servo was to get the proportional gain, K_P , as high as possible for fast system response while maintaining stability.

Time delay

Figure 5.6 illustrates the control workflow of the real-time control system. The acceleration response was first measured by the accelerometer node and collected by the data aggregator wirelessly. The acceleration data were then transferred to the target real-time PC and

were parsed such that the control gain could be calculated. Finally, the calculated control force was sent to the motor via serial RS232. The time required for sensing, wireless communication of the sensor, and control force calculation and actuation resulted in at least one-sample delay for the control system. Therefore, in this study, one sampled sensor delay of the control system was incorporated in continuous-time model using Padé approximation method (Golub and Van Loan, 1989).

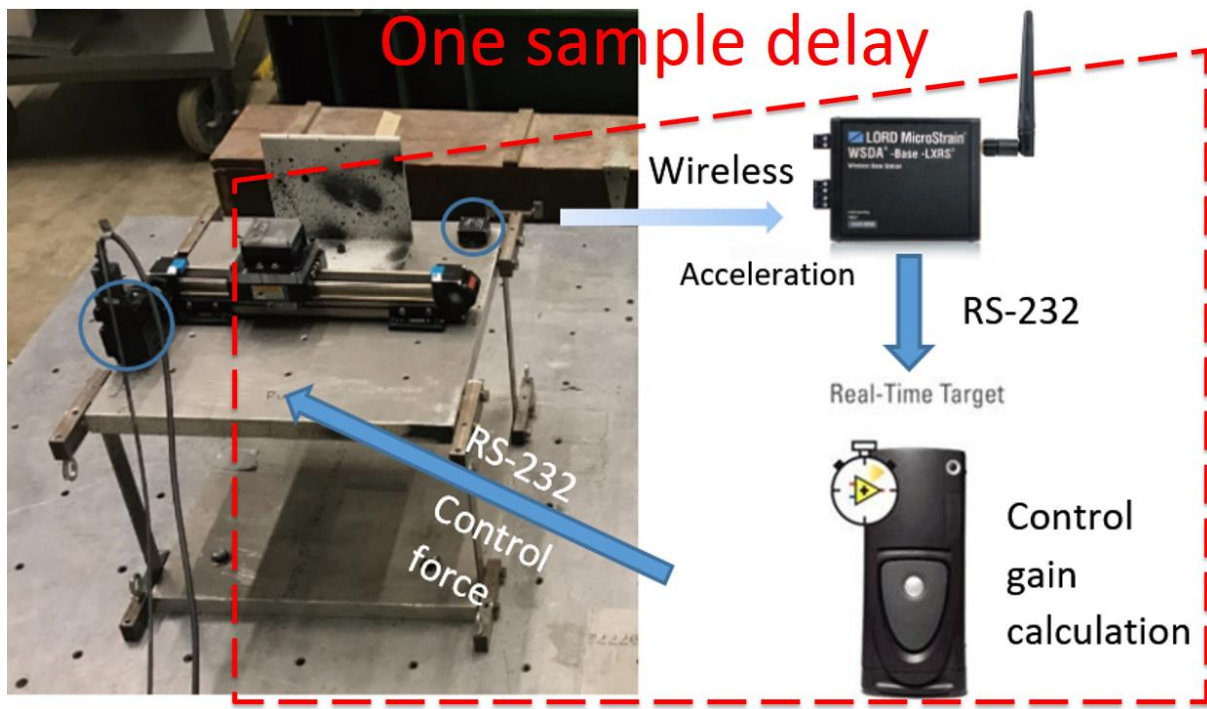


Figure 5.6: Workflow of the real-time control system.

Digitization

The minimum sampling rate of a control system is known as Nyquist frequency and is at least twice the system bandwidth to avoid aliasing of the higher dynamics. However, to approximate a discrete control system as continuous, the sample rate should be about thirty to fifty times the highest mode of interest (Franklin *et al.* 1998). Due the low sampling frequency of

the wireless sensors, a discrete-time representation of the controller is required. Therefore, the discrete sample time should also be considered in the control plant modeling. The continuous plant is converted to discrete time plant via zero-order hold (ZOH) transformation.

Controller for the one-story structure with an AMD system

For a one-story structure with an AMD system, the mass and stiffness matrices in the equations of motions can be expressed as:

$$\mathbf{M} = \begin{bmatrix} m_1 & 0 \\ 0 & m_d \end{bmatrix}, \quad \mathbf{K} = \begin{bmatrix} k_1 + k_d & -k_d \\ -k_d & k_d \end{bmatrix}, \quad (5.15)$$

and \mathbf{C} takes a form similar to \mathbf{K} . Here, m_1 and m_d are the masses of the primary structure and the damper mass, respectively; k_1 and k_d are the stiffness coefficients of the primary structure and stiffness, respectively. $\mathbf{x} = [x_1 \ x_d]^T$, x_1 and x_d are the floor displacement relative to the ground and the damper displacement relative to the floor, respectively.

The goal of this AMD system is set to control both structural displacement and acceleration equally. Therefore, equal weightings were assigned on floor displacement and floor acceleration by balance the weighing constants, $q_{\text{displacement}}$ and $q_{\text{acceleration}}$, in equation (5.7). The control force was limited by the physical actuator system and, therefore, was selected based on this limit while maximizing overall control performance. In this study, the weight, \mathbf{R} , was chosen to be $1e^{-3}$.

The Kalman estimator weights were determined experimentally because process noise and sensor noise existed in the experiments. The resulting process and sensor noise weights are:

$$\mathbf{S}_w = [0.1], \quad \mathbf{S}_v = [0.001].$$

5.2.3 Results

The uncontrolled structure and the structure with AMD were excited under five historic earthquake records (*i.e.*, 1992 Erzincan, 1994 Northridge, 1995 Kobe, 1999 Jiji and 2011 New Hall). Figure 5.7 shows a comparison of the time history acceleration of the uncontrolled and AMD systems under the Northridge and Newhall earthquakes. The figure clearly shows that the AMD system can significantly reduce the acceleration response during the earthquake excitations.

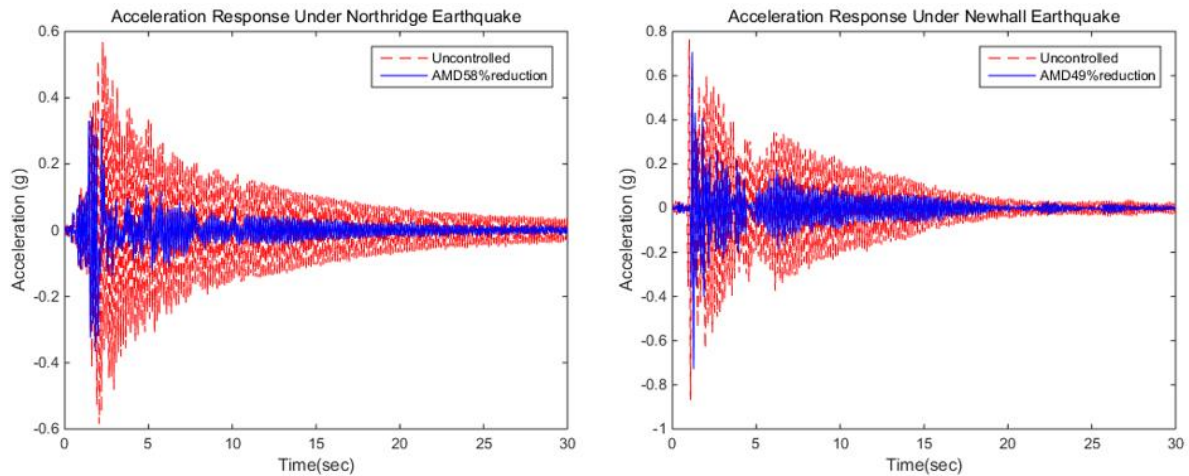


Figure 5.7: floor acceleration response under Northridge (left) and Newhall Earthquake (Right).

Table 5.2 and Table 5.3 shows the reduction in root mean square (RMS) of floor acceleration and displacement. In all earthquake cases, the AMD system reduced a significant amount of floor acceleration and displacement compared to the uncontrolled structure without any dampers. On average, the AMD reduced 54% floor acceleration and 43.62% floor displacement.

Table 5.2: RMS floor acceleration of the AMD systems compare to the uncontrolled structure.

| Excitation | Uncontrolled | AMD | |
|----------------|------------------|------------------|----------------|
| | Acceleration (g) | Acceleration (g) | Reduction |
| Northridge | 0.1139 | 0.0475 | -58.30% |
| Kobe | 0.1623 | 0.092 | -43.31% |
| New Hall | 0.1438 | 0.0726 | -49.51% |
| Jiji | 0.1608 | 0.0712 | -55.72% |
| Erzincan | 0.2648 | 0.1051 | -60.31% |
| Average | 0.16912 | 0.07768 | -54.07% |

Table 5.3: RMS floor displacement of the AMD systems compare to the uncontrolled structure.

| Excitation | Uncontrolled | AMD | |
|----------------|-------------------|-------------------|----------------|
| | Displacement (mm) | Displacement (mm) | Reduction |
| Northridge | 6.1086 | 3.5063 | -42.60% |
| Kobe | 3.918 | 2.2387 | -42.86% |
| New Hall | 1.0534 | 0.4505 | -57.23% |
| Jiji | 9.0477 | 5.2253 | -42.25% |
| Erzincan | 4.8678 | 2.6728 | -45.09% |
| Average | 4.9991 | 2.81872 | -43.62% |

In this pilot experiment, an AMD system with wireless acceleration feedback control was analyzed. Exciting the experimental structure with historical earthquake records, the AMD system was shown to significantly reduce structural motions. Through careful control design and hardware selection that particularly addressed system modeling, slow sampling rate of the wireless system and time delay compensation, the resulting controller design was proven robust under experimental testing.

5.3 Six-story Building Controlled with DSF damper system

The aforementioned AMD model showed that the proposed controller design performed well, and this section expands the active controller design to the double skin facade dampers system. The control algorithm was expanded to a six-story shear frames structure equipped with six sensors and six actuators. The performance of the double skin facade dampers system was compared to with the same structure with an AMD and the uncontrolled structure.

5.3.1 System Model

The experimental structure was a six-foot, six-story shear structure mounted on a fixed base (Figure 5.8). The structure used was essentially the same as the “uncontrolled structure” configuration in passive DSF mass damper experiments; structural details can be find in Section 4.1. One of the main differences was that the belt driven actuators replaced the linear rails used in the passive control experiment, therefore the structural weight (21.50 kg or 47.40 lb on each story) changed slightly compared to the passive design (23.8 kg or 52.5 lb). Structure stiffness was kept the same compared to the passive configuration.



Figure 5.8: The six-story experiment structure.

AMD

In this study, a single AMD was attached to the top story of the experiment building (Figure 5.9). The damper mass replaced the façade panels with equivalent weights (steel stocks) lumped on carriage of the actuator at the top story of the structure. The steel stocks weigh 13.46 kg (29.89 lb). The damper mass ratio (10.43%) of the AMD system was kept the approximately the same as the DSF damper system. Compared to the DSF system setup, the structure with the AMD had all the static parts of dampers remained on the 1st to 5th floors, with all the moving parts (e.g., façade panels) were replaced with equivalent weights at those floors. The carriages were locked on the actuators to prohibit any motion. The identification of the AMD properties

followed the same procedure as the single-story AMD system. The identified properties were listed in Table 5.4.



Figure 5.9: AMD damper configurations.

exceeded its current limit. To keep the motor running within its limit, the weighing \mathbf{R} was chosen as 160. In addition, the PID parameters of the SmartMotor was also tuned with higher K_p and K_d values to cater the heavy motor load.

Similar to the single-story AMD system, the Kalman Filter estimator weights were determined experimentally with the the process noise and sensor noise weights being:

$$\mathbf{S}_w = [1e^{-3}], \quad \mathbf{S}_v = 1e^{-3} \times \begin{bmatrix} 1 & & & & & \\ & 1 & & & & \\ & & 1 & & & \\ & & & 1 & & \\ & & & & 1 & \\ & & & & & 1 \end{bmatrix}. \quad (5.17)$$

DSF damper

Similar to the passive control experiment in Chapter 4, three DSF damper configurations were tested: one-, two- and three-damper configurations (Figure 5.10). In the one-damper configuration, the façade spanned and connected to all six floors and, thus, moved as an entire piece. In the two- and three-damper configurations, each of the DSF dampers spanned three or two floors, respectively.

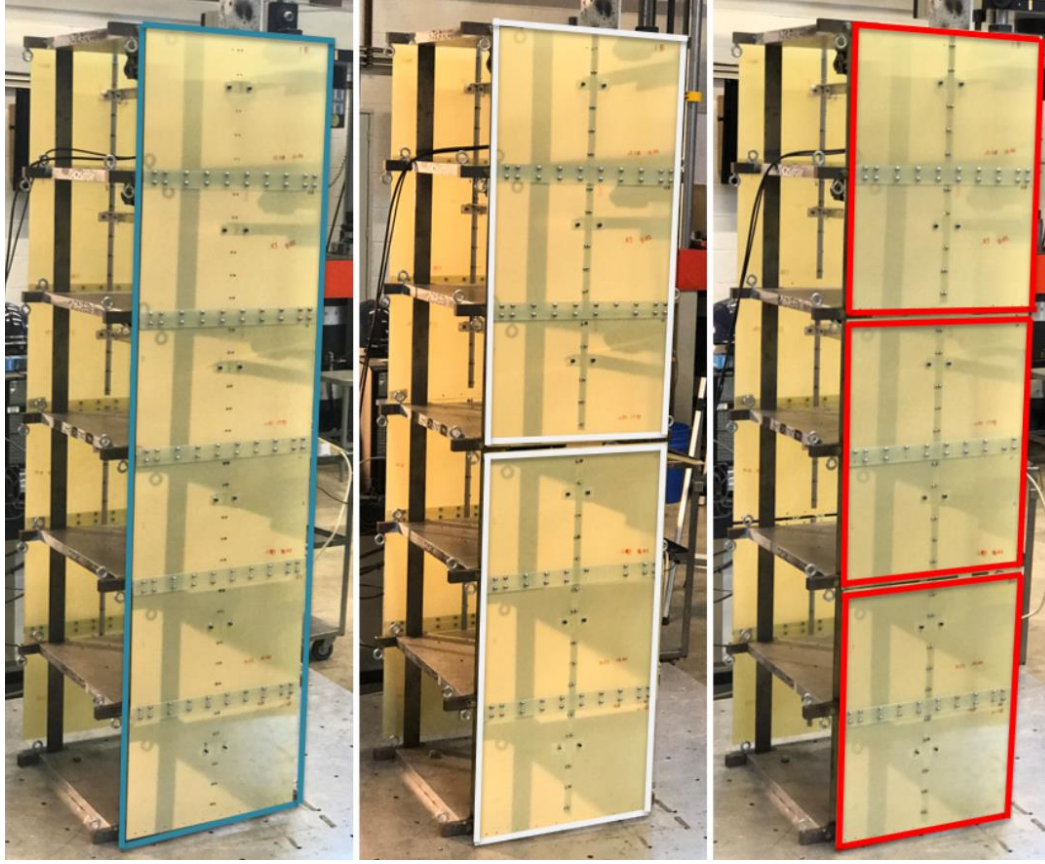


Figure 5.10: DSF damper configurations: one-damper (left), two-damper (middle) and three dampers (right).

To make each of the DSF damper to move as a piece, it was essential to have synchronized motion between the actuators associated with the damper. A master and slave configuration was created for the SmartMotors to synchronize the control of multiple actuators. In the master-slave configuration, the master motor initiated a repetitive sinusoidal motion and sent its internal encoder signals to the slave motors via wires. The slave motors, in “Mode Follow”, then moved based on the incoming encoder signals to synchronize to the master motor’s motion. Figure 5.11 illustrates the master-slave SmartMotor configuration for one, two- and three-damper configurations respectively. In the one-damper configuration with the entire façade moving as one piece, Motor 6 at the top floor was selected as the master motor while the motors at the lower floor levels served as slave motors. In the two-damper configuration, each of

the DSF dampers spanned three floors; thus, the Motors 3 and 6 were selected to be the master motors. In the three-damper configuration, Motors 2, 4 and 6 were selected to the master motors.

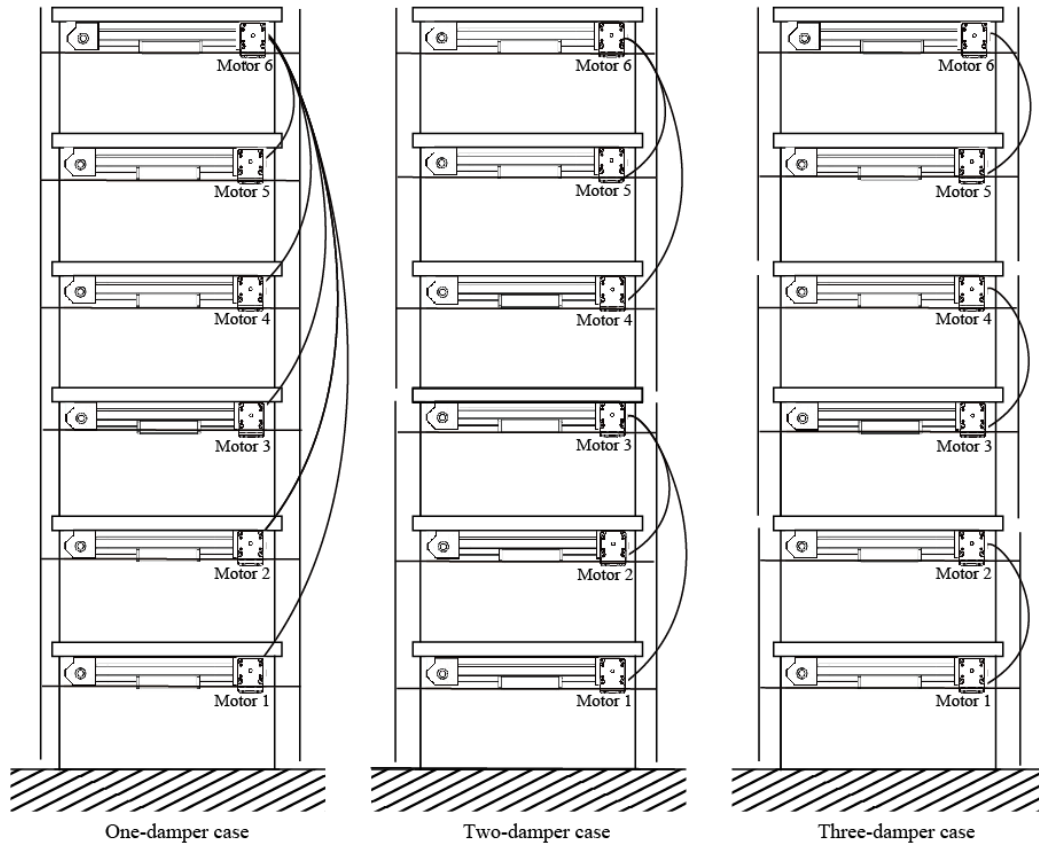


Figure 5.11: the master and slave SmartMotor configurations for DSF damper systems.

Compared to Chapter 4, the linear guides used in the passive experiments was replaced by the belt-driven actuators oriented along the shake table stroke direction in this active control experiment. The fiber glass panels on each side of the building were connected by a horizontal T-bar attached to carriage of the actuator. The DSF mass damper weighed 2.01 kg (4.43 lb) and had a 9.35% damper mass ratio relative to the primary structural mass. The design of the controller followed the same procedure as the designing the controller for the AMD system.

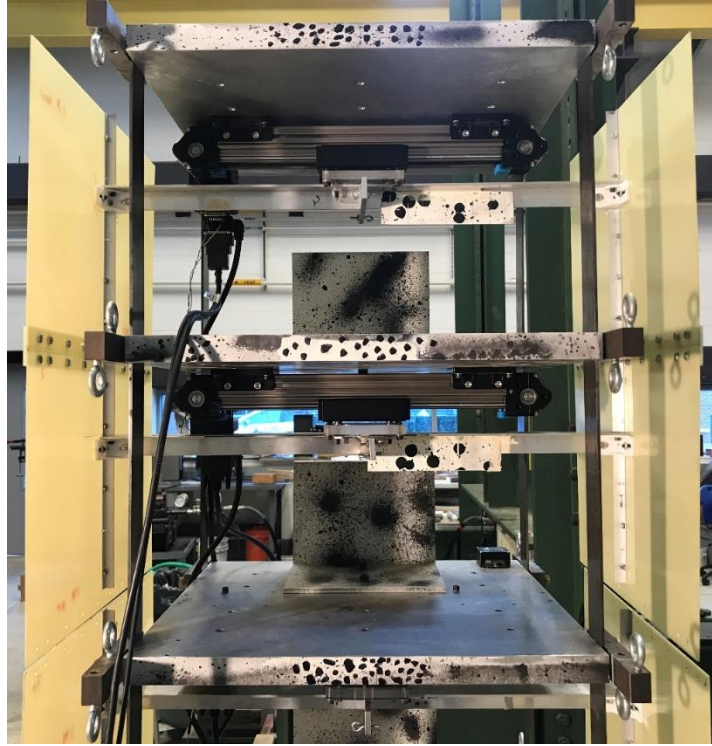


Figure 5.12: DSF damper configurations.

To make a fair comparison between the DSF damper cases and the AMD case, the overall control forces should be in similar range between the two systems. Therefore, the weighing matrices, \mathbf{R} , in the DSF dampers systems were chosen to yield a similar amount of overall control forces compared to that of the AMD system. Table 5.4 shows the values of \mathbf{Q} and \mathbf{R} used in the AMD and DSF systems. Given that the DSF two- and three-damper configurations had multiple master actuators, their \mathbf{R} varied in sizes according to the number of independent actuators.

Table 5.5: The Q and R matrix used in controller design

| | AMD | DSF one-damper | DSF two-damper | DSF three-damper |
|----------|--|---|--|---|
| Q | $\mathbf{Q} = \begin{bmatrix} 6.804e^{-5} & \\ & 4626.806 \end{bmatrix}$ | $\mathbf{Q} = \begin{bmatrix} 1723.10 & \\ & 187.676 \end{bmatrix}$ | $\mathbf{Q} = \begin{bmatrix} 9955.1 & \\ & 0.1067 \end{bmatrix}$ | $\mathbf{Q} = \begin{bmatrix} 258.044 & \\ & 0.032 \end{bmatrix}$ |
| R | $\mathbf{R} = [8.63]$ | $\mathbf{R} = [8.61]$ | $\mathbf{R} = \begin{bmatrix} 4.930e^{-2} & \\ & 5.84e^{-2} \end{bmatrix}$ | $\mathbf{R} = \begin{bmatrix} 3.59e^{-3} & & \\ & 6.00e^{-3} & \\ & & 6.20e^{-5} \end{bmatrix}$ |

Shake table tests were conducted on the three systems: 1) an uncontrolled structure, 2) a structure equipped with an AMD on the top floor, 3) a structure with an active DSF damper system. To account for the extra weight of the façade panels in the DSF system, equivalent weights of the façade panels were installed on each floor as static weights on the AMD and uncontrolled structures.

5.3.2 Result Discussion

Five experimental structures (an uncontrolled structure, an AMD system, and three configurations of the DSF damper system) were tested under five historic earthquake records (*i.e.*, 1992 Erzincan, 1994 Northridge, 1995 Kobe, 1999 Jiji and 2011 New Hall). The absolute accelerations and displacements of all six floors were measured.

Figure 5.13 shows a comparison of the top floor (6th floor) time history acceleration of the uncontrolled, AMD and three-damper DSF systems under the Northridge and Jiji earthquakes. The earthquake excitation duration was about 30 seconds for the Northridge earthquake and 50 seconds for the Jiji earthquake. As shown in Figure 5.13, both the AMD and DSF systems reduced vibrations significantly compared to the uncontrolled structure. The structure with the AMD reduced the top-floor vibration by 71.44% under New Hall, 62.81% under Erzincan, 67.44% under Northridge and by 49.80% under Jiji earthquakes. Meanwhile, the DSF dampers outperformed the AMD by reducing responses by 81.66% under New Hall, 69.81% under Erzincan, 83.72% under Northridge and by 55.14% under Jiji earthquakes.

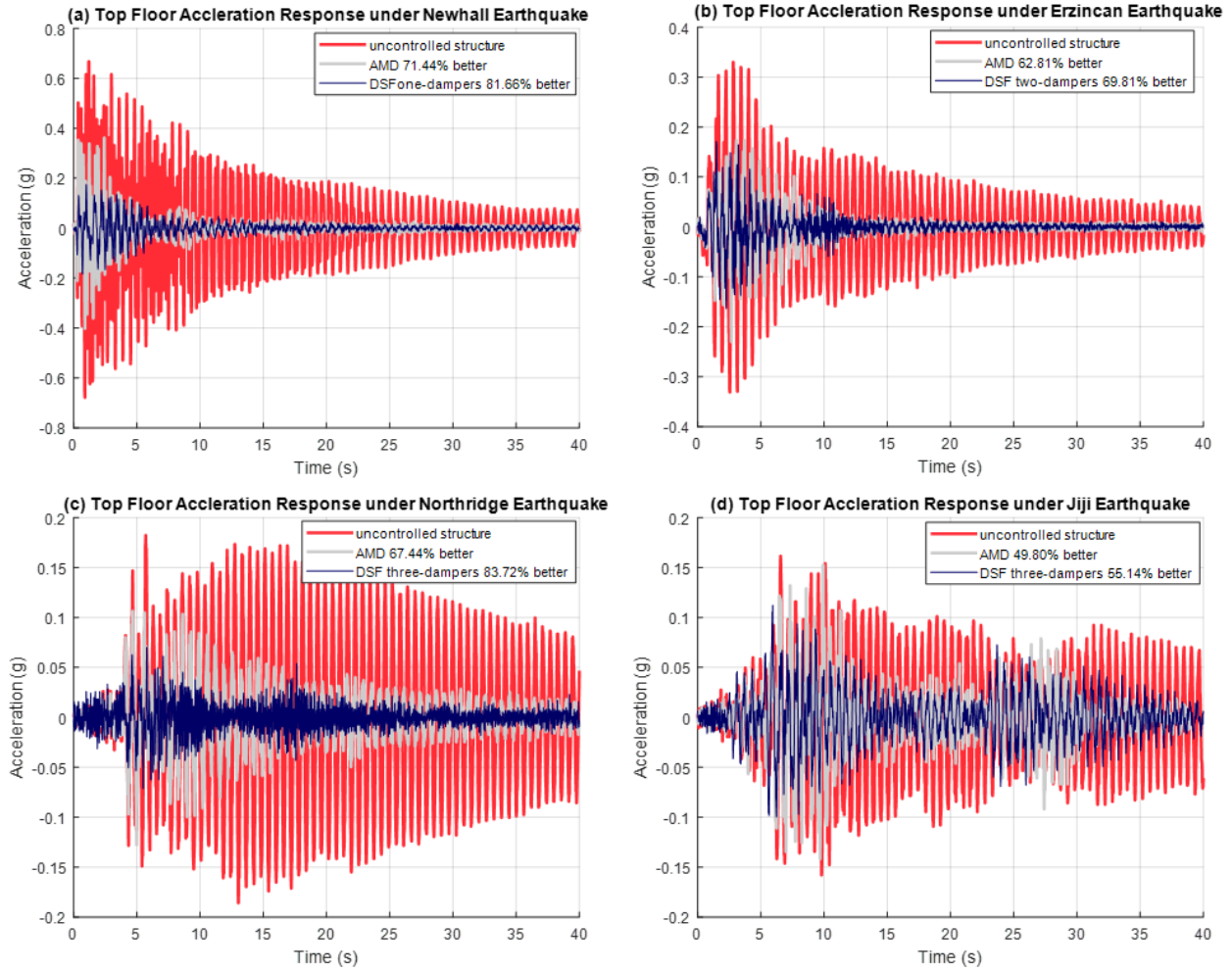


Figure 5.13: Top floor acceleration response of uncontrolled structure, AMD and (a) one-damper DSF system under Newhall earthquake, (b) two-damper DSF system under Erzincan earthquake, (c) three-damper DSF system under Northridge earthquake and (d) three-damper DSF system under Jiji earthquake.

Table 5.6: Summation of RMS command control forces of the DSF damper and AMD systems

| Excitation | AMD | DSF one-damper | DSF two-damper | DSF three-damper |
|------------|-------------------|-------------------|-------------------|-------------------|
| | Control force (N) | Control force (N) | Control force (N) | Control force (N) |
| Northridge | 0.573 | 0.515 | 0.532 | 0.559 |
| Kobe | 2.182 | 2.088 | 2.011 | 2.084 |
| New Hall | 2.743 | 2.479 | 2.512 | 2.584 |
| Jiji | 2.181 | 2.040 | 2.013 | 2.005 |
| Erzincan | 1.609 | 1.659 | 1.667 | 1.607 |
| Average | 1.858 | 1.756 | 1.747 | 1.768 |

Table 5.7: Average RMS acceleration of the DSF damper systems compare to AMD system and uncontrolled structure (RMS: root mean square).

| Excitation | Uncontrolled | | AMD | | DSF one-damper | | DSF two-damper | | DSF three-damper | |
|----------------|---------------|---------------|----------------|---------------|----------------|---------------|----------------|---------------|------------------|--|
| | Accel. (g) | Accel. (g) | Reduct. | Accel. (g) | Reduct. | Accel. (g) | Reduct. | Accel. (g) | Reduct. | |
| Northridge | 0.0287 | 0.0158 | -45.03% | 0.0077 | -73.20% | 0.0097 | -66.23% | 0.0118 | -58.84% | |
| Kobe | 0.0562 | 0.0355 | -36.85% | 0.0232 | -58.74% | 0.0259 | -53.89% | 0.0267 | -52.54% | |
| New Hall | 0.0794 | 0.0357 | -55.05% | 0.0286 | -63.93% | 0.0327 | -58.84% | 0.0310 | -61.01% | |
| Jiji | 0.0421 | 0.0229 | -45.61% | 0.0212 | -49.64% | 0.0227 | -46.11% | 0.0217 | -48.57% | |
| Erzincan | 0.0595 | 0.0249 | -58.23% | 0.0215 | -63.89% | 0.0231 | -61.24% | 0.0251 | -57.75% | |
| Average | 0.0532 | 0.0269 | -49.34% | 0.0204 | -61.57% | 0.0228 | -57.12% | 0.0233 | -56.29% | |

Table 5.8: Average RMS displacements of the DSF damper systems compare to AMD system and uncontrolled structure (RMS: root mean square).

| Excitation | Uncontrolled | | AMD | | DSF one-damper | | DSF two-damper | | DSF three-damper | |
|----------------|----------------|----------------|----------------|----------------|----------------|----------------|----------------|----------------|------------------|--|
| | Displ. (mm) | Displ. (mm) | Reduct. | Displ. (mm) | Reduct. | Displ. (mm) | Reduct. | Displ. (mm) | Reduct. | |
| Northridge | 6.2840 | 3.6636 | -41.70% | 2.7612 | -56.06% | 7.2645 | -54.49% | 2.8049 | -55.36% | |
| Kobe | 4.5589 | 3.1119 | -31.74% | 2.2569 | -50.49% | 2.1618 | -52.58% | 2.1725 | -52.35% | |
| New Hall | 2.4631 | 1.6790 | -31.84% | 1.3063 | -46.97% | 1.3433 | -45.46% | 1.1738 | -52.35% | |
| Jiji | 13.2842 | 8.2823 | -37.65% | 7.9672 | -40.03% | 8.0135 | -39.68% | 8.0632 | -39.30% | |
| Erzincan | 4.2518 | 2.5014 | -41.17% | 2.2436 | -47.23% | 2.3457 | -44.83% | 2.1502 | -49.43% | |
| Average | 6.1684 | 3.8476 | -37.62% | 3.3070 | -46.39% | 3.3449 | -45.77% | 3.2729 | -46.94% | |

Table 5.6 displays RMS command control forces of the DSF damper AMD systems. In the DSF systems, a summation was taken for the control forces in the multiple actuators. With the controllers based on the LQR weighing matrices in Table 5.4, the overall control forces in the three DSF damper configurations were similar. They also had similar forces compared to the AMD system. The similarity in control forces implied that all the active control system were on a similar playing field; none of the active control systems used a much larger amount of force to control responses compared to other systems.

As shown in Table 5.7, all active DSF damper systems reduced significant amounts of floor acceleration and displacements compared to the uncontrolled structure in the five earthquake records. With the same level control forces, the overall performance of DSF

outperformed the AMD system. In terms of the average acceleration reduction, Table 5.8 shows that all active DSF damper systems outperformed the AMD system by at least 7% in all five earthquake excitations. Among the DSF configurations, the one-damper configuration was overall the best performing system. The one-damper configuration reduced an averaging 61.57% of floor acceleration compared to the uncontrolled structure when the two-damper and three-damper configurations reduced an averaging 57.12% and 56.29% of floor acceleration, respectively. In terms of the average floor displacement reduction, all three DSF configurations had very similar performance with 46.39%, 45.77% and 46.94% of average floor displacement reductions.

5.4 Comparing Active control to Passive control

The actively controlled DSF and AMD systems were compared to the passively controlled DSF and TMD systems (from Chapter 4). Figure 5.14 shows the reduction rates in terms of averaged floor accelerations across all five earthquakes responses. The active systems outperformed the passive systems. The AMD system doubled the reduction rate compared to the TMD system, while the active DSF damper systems outperformed the passive DSF damper systems by approximately 10%. For both passive and active control systems, the performance of the two-damper and three-damper configurations are similar and outperformed by DSF one-damper case. However, given that a rigid single DSF damper (spanning the entire height of a building) is unpractical for tall buildings, configurations of multiple DSF dampers shall be adopted.

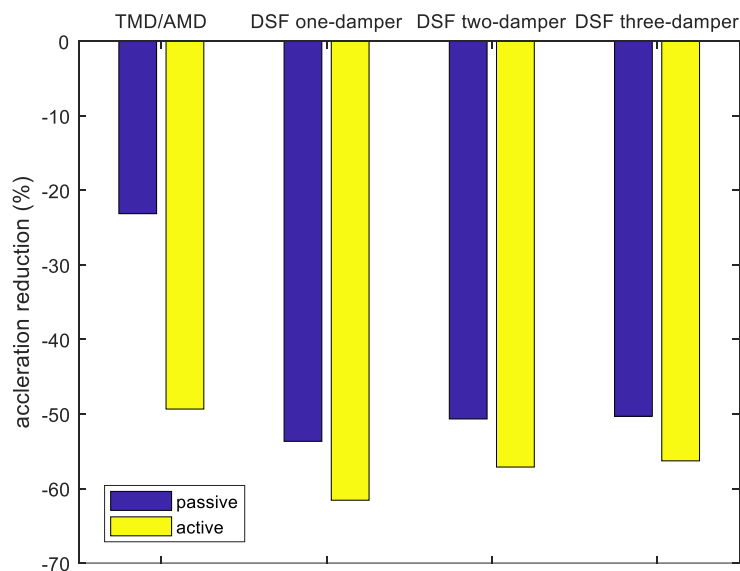


Figure 5.14: Average reduction in acceleration comparing active and passive control systems.

5.5 Conclusion

In this study, an AMD on a single-story building was first experimented. The system contained a LQG controller with wireless acceleration feedback. Through careful control design and hardware implementation that addressed system modeling, slow sampling rate of the wireless system and time delay compensation, the resulting controller design was proven robust and effective. The selected hardware were also shown to be reliable under the real-time close loop control setting. In a shake table test, the AMD system could better reduce the single-story structural response compared to the uncontrolled structure.

The design of the AMD on a single-story building was expanded to actively control the DSF damper system on a six-story shear structure. In the experiments, each floor was equipped with a wireless sensor and an actuators. Based on wireless acceleration feedbacks, active control strategies were designed to balance the reductions in both floor displacement and acceleration. Under the five historical earthquakes, the actively controlled DSF system outperformed the uncontrolled and passive systems. In addition, the actively controlled DSF system also outperformed the AMD system with a similar level of control force.

Chapter 6. Structural health monitoring with DSF damper system

In previous chapters, the DSF damper system has been shown synergistic in vibration mitigation and energy reduction in buildings. The actuators installed in the DSF damper system can also be used to excite the structure. This section introduces and discusses another useful aspect of the DSF damper system— structural health monitoring (SHM).

SHM reliability depends on accurate estimations of structural characteristics from structural response measurements. However, some structural characteristics, such as natural frequencies and structural mode shapes, may not be well represented or identifiable depending on how structures are excited, thereby compromising the effectiveness of SHM.

Vibration based SHM commonly include forced vibration or ambient vibration. During forced vibration tests, the structure is sometimes excited to a steady-state response with one or more shakers with controllable speeds and/or forces (Hudson, 1962). The most common shakers used in buildings are eccentric mass shakers. These shakers are usually installed on the roof of a building and the building can be shaken routinely for the SHM purposes. However, conducting shaker tests is time consuming and often requires special permissions from the building owners; in addition, the shaker itself lacks mobility and is not easy to install (Beskhyroun *et. al.* 2013). Another important approach to dynamic testing of structures is ambient based vibration tests, in which vibrations are induced by wind, traffic, operational use, etc. Though ambient vibration tests are economical and easy to conduct, they usually have low signal-to-noise ratios because of their low excitation amplitudes therefore requires advanced signal processing and identification

techniques, this complicates and affects the results of the modal analysis (Omenzetter *et. al.* 2013).

Due to the aforementioned difficulties in the traditional forced vibration and ambient vibration for SHM, Fu and Johnson (2013) developed a distributed mass damper (DMD) system that would use existing multiple active mass dampers to excite the structure and analyze the resulting responses. In computer simulations, the dampers were shown to be able to provide harmonic excitations to target specific structural modes/frequencies and to amplify structural responses. The accuracy of damage detection was successfully demonstrated on a 20-story simulated structure model.

In this study, the actuators — introduced to control the movements of the DSF for structural and environmental controls – are also used to excite the structure for SHM purposes. The actuators are installed at every floor of the structure and can provide excitations to any floors. This system enhances the robustness of SHM because the actuators can generate repeatable excitations for the building. In addition, the actuators can target specific structural modes (i.e., frequencies) for modal analyses and to amplify structural responses, improving the noise-to-signal ratio of sensor measurements. This chapter details the conducted experiments that showed how to excite the structure at multiple locations with multiple actuators for SHM.

6.1 Experiment setup

The experimental structure was a six-foot, six-story shear structure mounted on a fixed base (Figure 6.1). The structure used was essentially the same as the “uncontrolled structure” configuration in the DSF mass damper experiments; structural details can be found in Section 5.3.1. In this SHM experiment configuration, the main structure weighed 21.50 kg (47.40 lb). To simulate “healthy” and “damaged” cases, cross braced springs were installed on the structure to adjust the stiffness at certain floor levels without damaging the main structure. A single cross bracing consisted of one spring and two turnbuckles (Figure 6.2), and they could be easily installed and removed. The stiffness of each spring was 2.35 N/mm (13.41 lb/inch) and total mass of all three components (two turn buckles and one spring) was 0.49 kg (1.07 lb). When a story was fully braced, the four cross bracings would add a total of 1.94 kg (4.28 lb) to the structure.

A healthy structure was fully braced in all stories with springs (Figure 6.3) and damage was introduced by removing bracing springs at one or more stories (Figure 6.4), when the springs were removed to change the inter-story stiffness, they were taped to the floor from which they were removed to maintain a constant mass for that specific floor.



Figure 6.1: Six-story shear experimental structure.



Figure 6.2: Spring and turnbuckles used for cross bracing photo credit: Kyle Wyatt 2015) .



Figure 6.3: Test configuration for a “healthy” structure.



Figure 6.4: Test configuration for a damaged floor (6th) case.



Figure 6.5: The motor and belt driven actuator set-up.

Acceleration data of each story were recorded by a Microstrain® G-Link® -LXRS® wireless accelerometer (2017). A Microstrain G-Link-LXRS wireless accelerometer node were installed on floor of the building. The wireless accelerometers had a 12-bit resolution and ± 2 g range and their sampling rate was set to 256 Hz. A WSDA-102 serial interface data aggregator was used to collect the acceleration data.

Three configurations of actuators and structural combination were tested for SHM purposes; Active mass damper (AMD), Distributed Mass Dampers (DMD) and Double Skin Façade Damper (DSF) systems. The difference of these three systems in structural control were explained in Section 2.2. The experiment setup for these three configurations is displayed in Figure 6.6 and described in the following sections:

AMD: this case utilized an active mass damper located on the top floor to excite the structure. The AMD case resembled a traditional structural exciter, which excited the structure only at the top floor. The AMD setup for SHM utilized a similar setup for the AMD system mentioned in the Chapter 5. The AMD system had damper weight of 23 kg, or a damper mass ratio of 10% compared to the overall structural weight. AMD's damper mass was equivalent to all the damper masses in the DSF or DMD systems.

DMD: the actuators were installed at every floor. The cart of the each actuator carried a mass damper which had a 10% damper mass ratio relative to the floor mass.

DSF: the actuators were installed at every floor and connected to the façade panels. The configuration differed from the DMD damper configuration. Given that DSFs are typically installed by hanging the multi-story façades from the top of the associating stories, the DSF dampers were attached on the ceilings to match typical DSF installations. In this study, a three-

damper case (described in Section 5.3) was chosen since the actuators were separated into three groups to maximize the testing flexibility. Under this case, with each façade damper attached to two floors, the actuators on these two floors were moving as one unit.

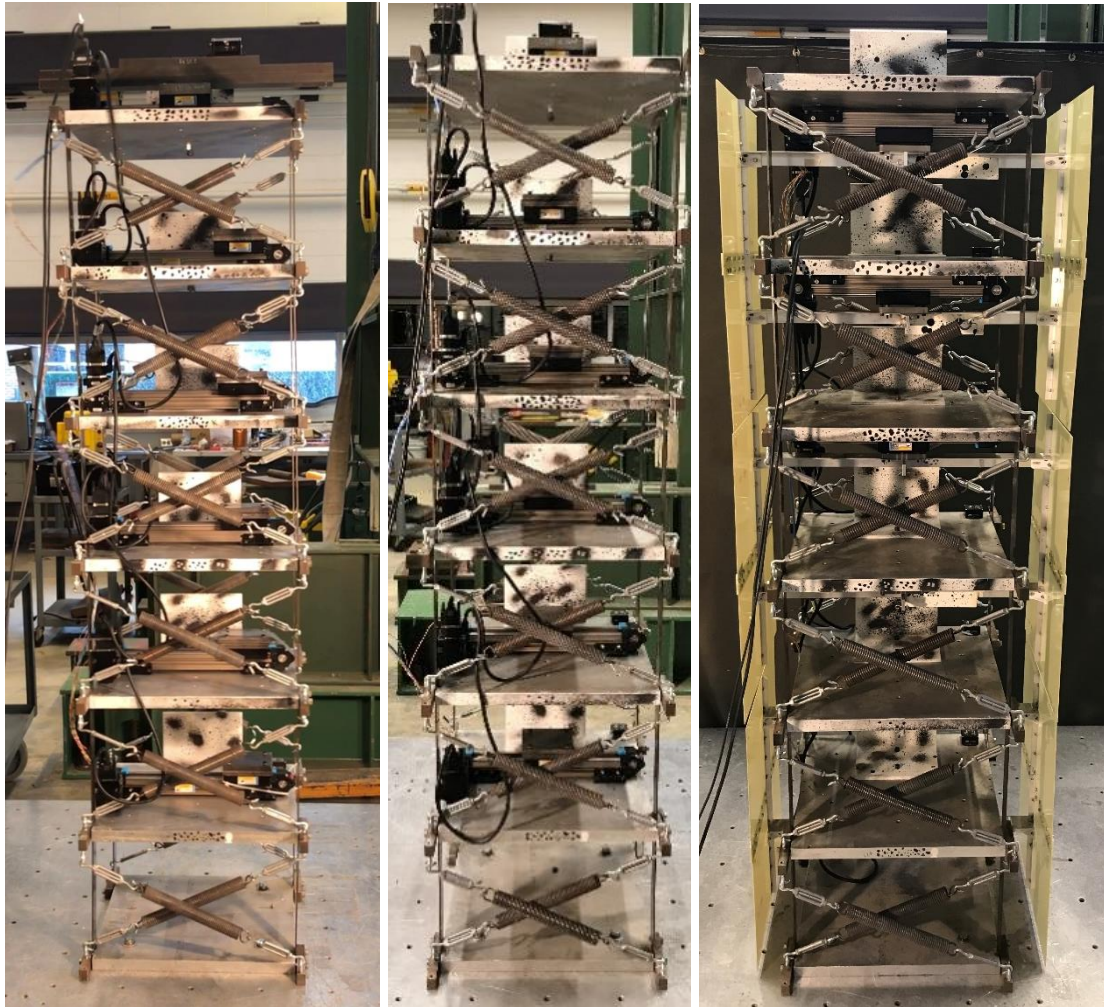


Figure 6.6: System setup for the AMD (left), DMD (middle) and DSF (right) systems.

6.2 Modal estimation

The mode shape of any particular structural mode could be found by analyzing the steady-state responses of the structure excited at these particular modes. To generate excitations targeting specific structural modal frequencies, sinusoidal motor motion profiles were created to oscillate the dampers at frequencies close to the fundamental modal frequencies of the structure.

For the AMD system, only the actuator installed on the top floor was in motion and the other actuators were not motorized and acted as dead weight. To create smooth sinusoidal excitations, the top floor's Smartmotor was set in "Cam Mode" (Electronic Camming). Under the Cam Mode, the motor moved to pre-defined locations stored in the motors' memory. These locations were constructed to form a full cycle of sinusoidal motion. A repeating sinusoidal motion was programmed and the frequencies of the sinusoidal motion could be adjusted depending on a specific modal frequency of interest.

For the DMD and DSF systems, the actuators at different floors were configured to have synchronized sinusoidal motions. A master and slave configuration was created for the Smartmotors. The master motor initiated a repetitive sinusoidal motion and sent its internal encoder signal to the slave motors via wires; the slave motors, in "Mode Follow", then moved based on the incoming encoder signals to synchronize to the master motor's motion. In Figure 6.7, the master Smartmotor was connected to five slave motors by wires. The Mode Follow also allowed the slave motors to move in reversed directions of the master motor.

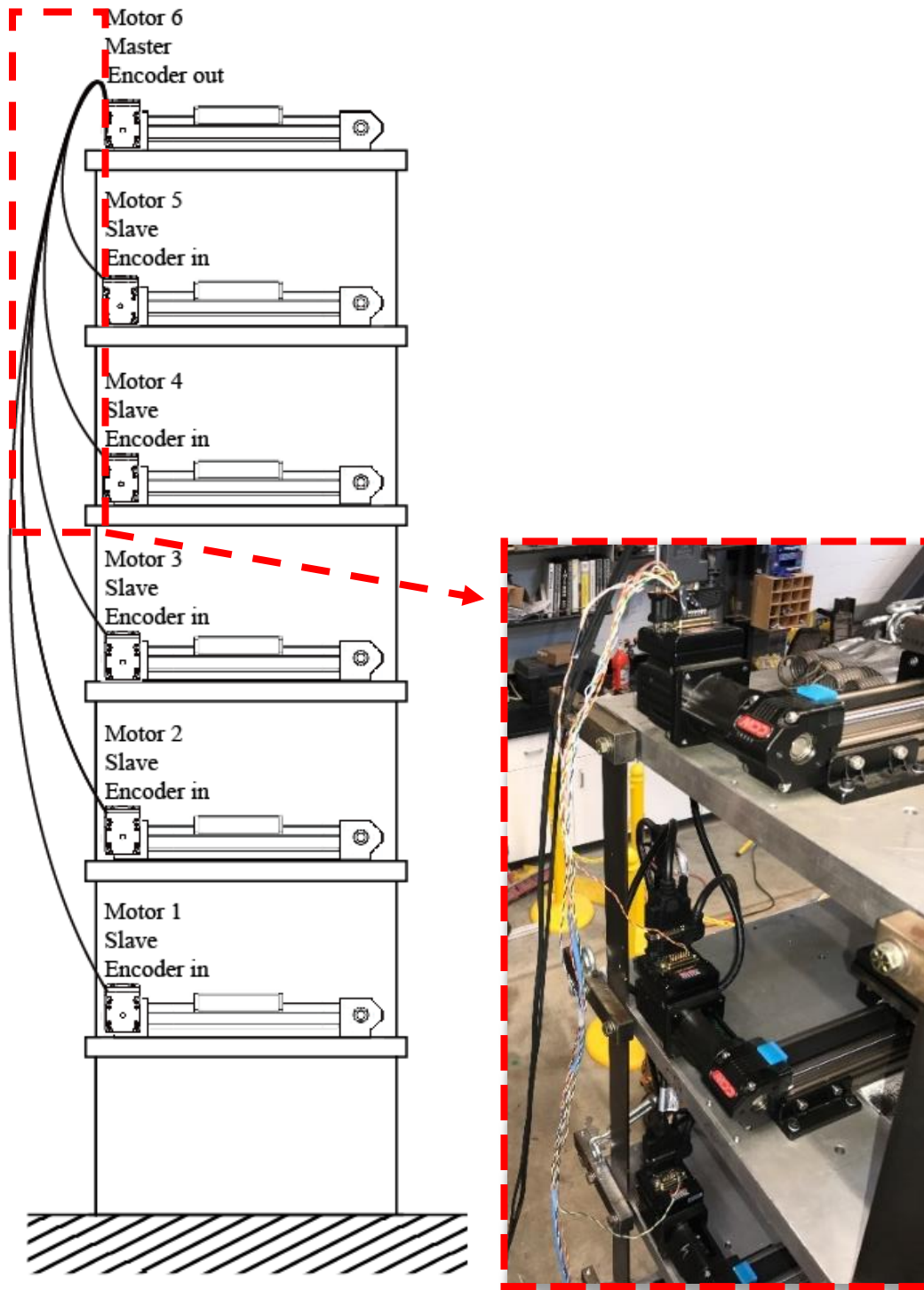


Figure 6.7: The master and slave motors configuration.

The bi-directional following feature allowed the motors to be programmed to move in a pattern correspond to the mode shape of the structure (e.g., different stories moving in opposite directions). In this study, the first three modes of the structure were excited and the actuators were applying forces with the same magnitudes but with directions in each story corresponding to the mode shape of the targeted mode.

Table 6.1 and Figure 6.8 summarize the motion patterns of the actuators under DMD configuration. To target the first mode, all six actuators moved with the same magnitude and direction. For the second mode, all the actuators had the same magnitude but the actuators in the top three stories moved in the opposite direction compared to the bottom three stories.

Table 6.1. Motion patterns of the actuators targeting the first and second modes

| | Mode 1 | Mode 2 |
|---------|--------|--------|
| Story 6 | + | + |
| Story 5 | + | + |
| Story 4 | + | + |
| Story 3 | + | - |
| Story 2 | + | - |
| Story 1 | + | - |

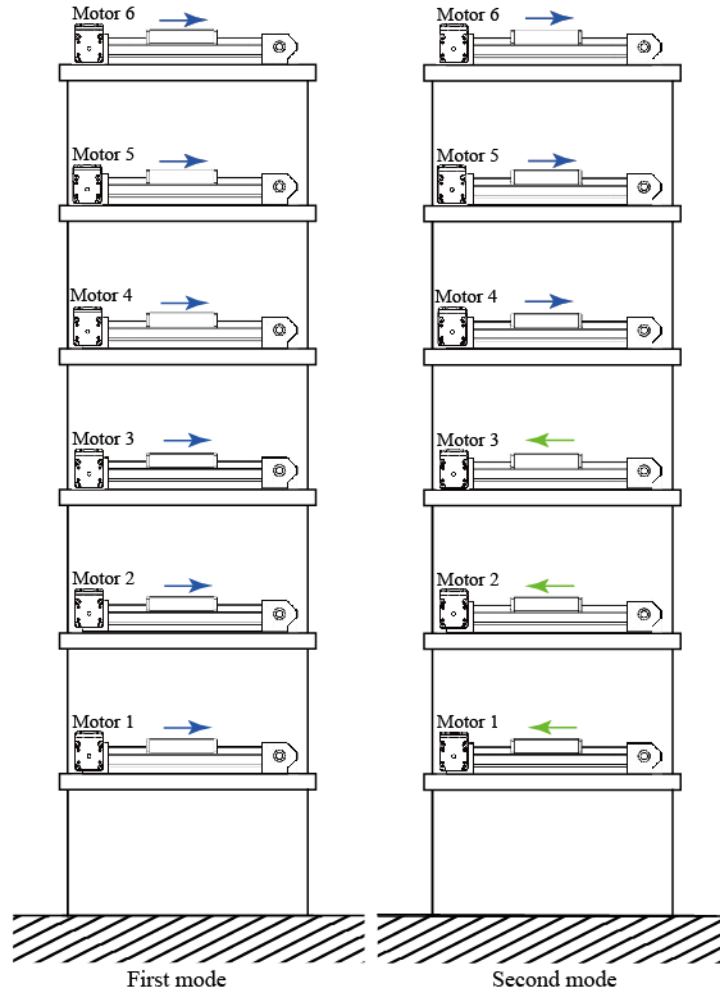


Figure 6.8: Motion patterns of the actuators targeting under the DMD configuration.

The DSF three-damper case was selected for SHM testing. Table 6.2 and Figure 6.9 summarize the motion patterns of the actuators under DSF configuration, same as the DMD configurations, all six actuators were moving with the same magnitude and direction to target the first mode. For the second mode, since the actuators were installed on the “ceilings”, it changed the center of gravity for each floor and affect the mode shapes thereby. This led to a actuator direction pattern different from the DMD system; the actuators in the top two stories moved in the opposite direction compared to the bottom four stories.

Table 6.2. Motion patterns of the actuators targeting the first and second modes

| | Mode 1 | Mode 2 |
|---------|--------|--------|
| Story 6 | + | + |
| Story 5 | + | + |
| Story 4 | + | - |
| Story 3 | + | - |
| Story 2 | + | - |
| Story 1 | + | - |

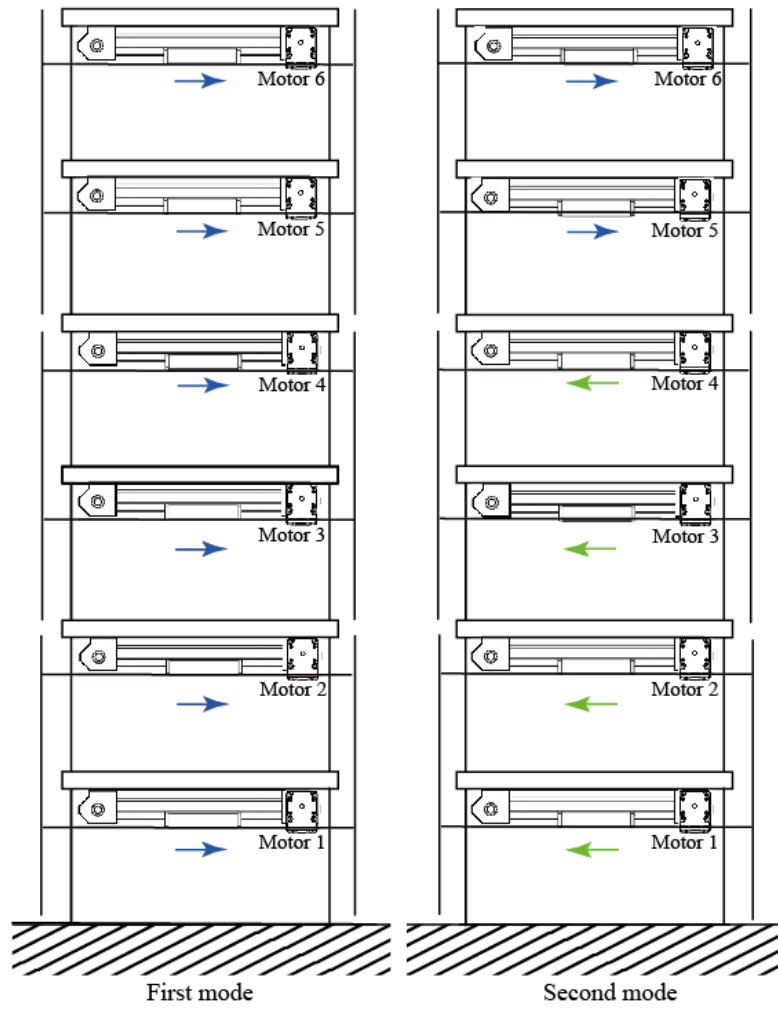


Figure 6.9: Motion patterns of the actuators under DSF configuration.

The modal frequencies of the structure can be found by comparing the magnitudes of responses caused by harmonic excitations at various frequencies. Frequency sweep tests were conducted for the AMD, DMD and DSF systems to detect the structures' modal frequencies. Then the motors were programed to target these frequencies. When the structure was exciting near a natural frequency, the structure was in resonance and the response gradually amplified and eventually reached a steady state. Figure 6.10 shows the acceleration responses of all six stories when the structure was excited by both the DSF and AMD systems at the frequency corresponding to the 2nd mode of the structure. As shown in the figure, the structural responses gradually amplified and reached steady state in approximately six seconds from still.

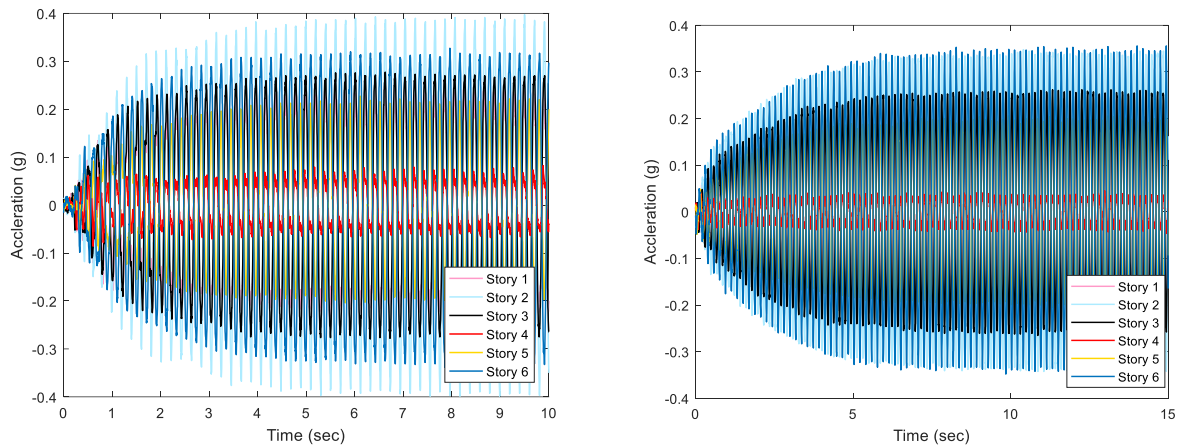


Figure 6.10: Structural harmonic response for DSF (left) and AMD (right).

The steady state responses were related to the mode shapes of the structure. Figure 6.11, Figure 6.12 and Figure 6.13 shows the acceleration responses when the AMD, DMD and DSF system was excited at the 1st and 2st mode, respectively. In the steady state responses, the amplitudes of floor responses was distinctly proportional to the mode shapes of the system. In the other words, the mode shape values indicated how stories deformed relative to one another for a particular mode.

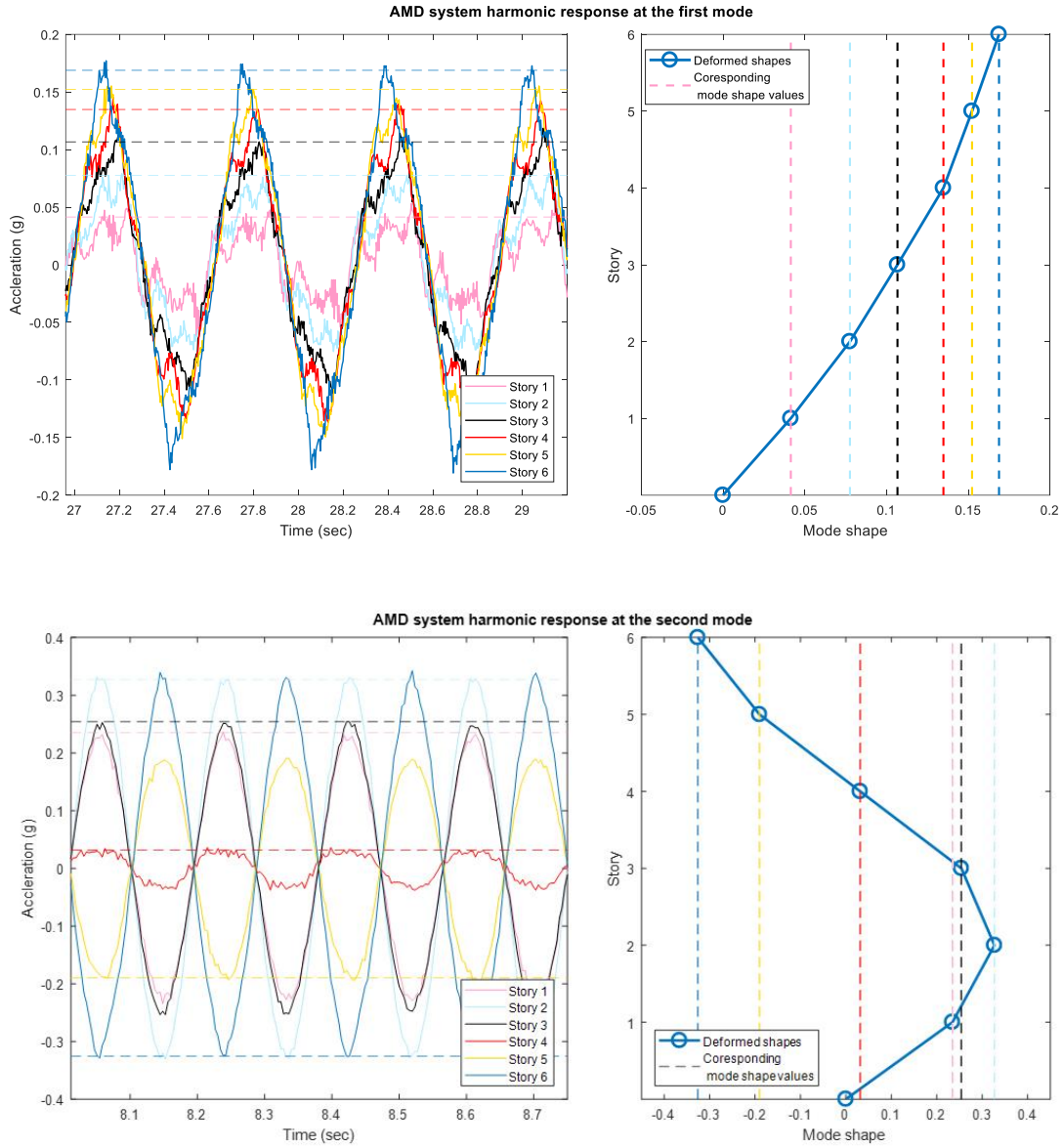


Figure 6.11: AMD system's harmonic response and mode shapes.

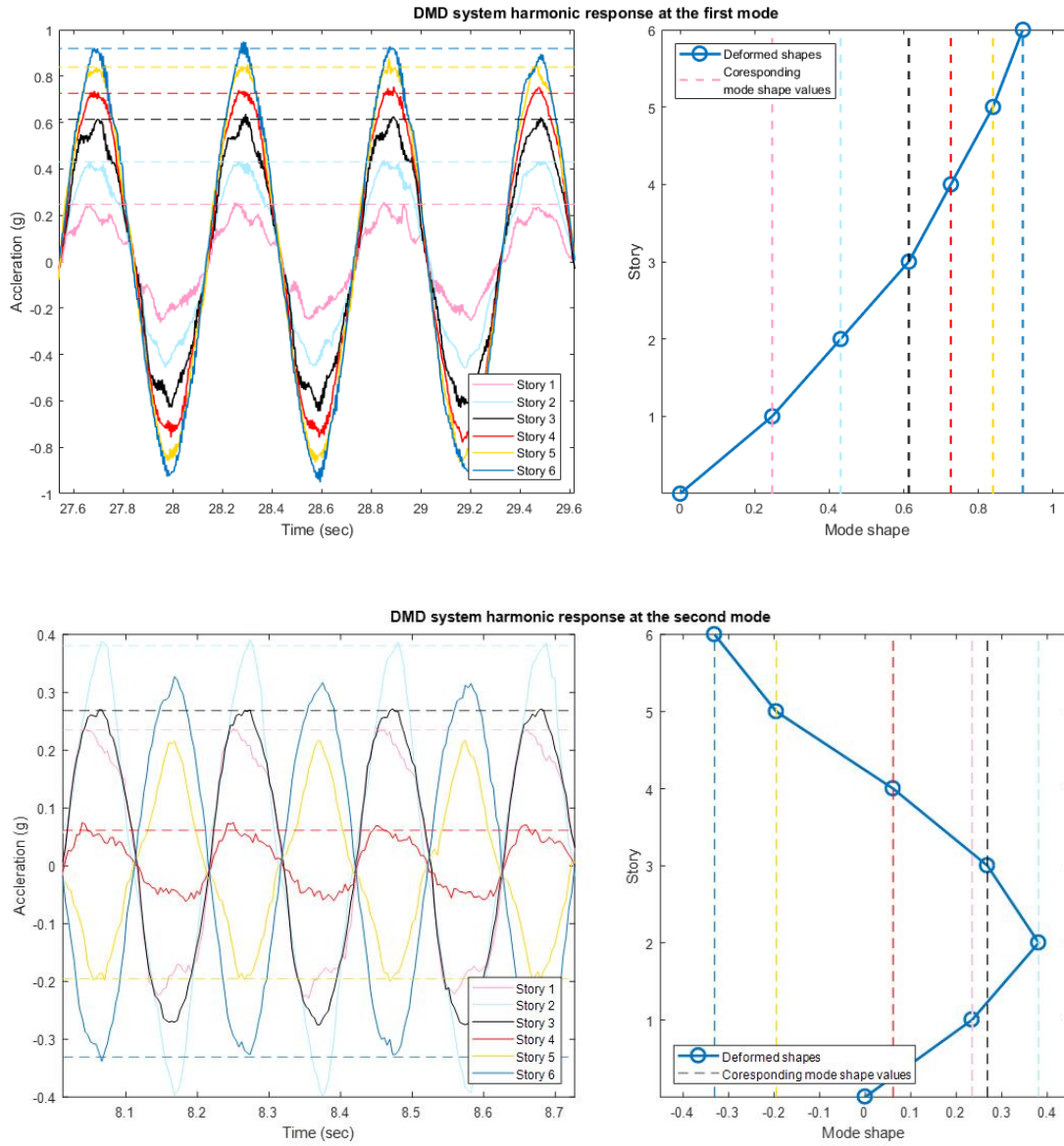


Figure 6.12: DMD system's harmonic response and mode shapes.

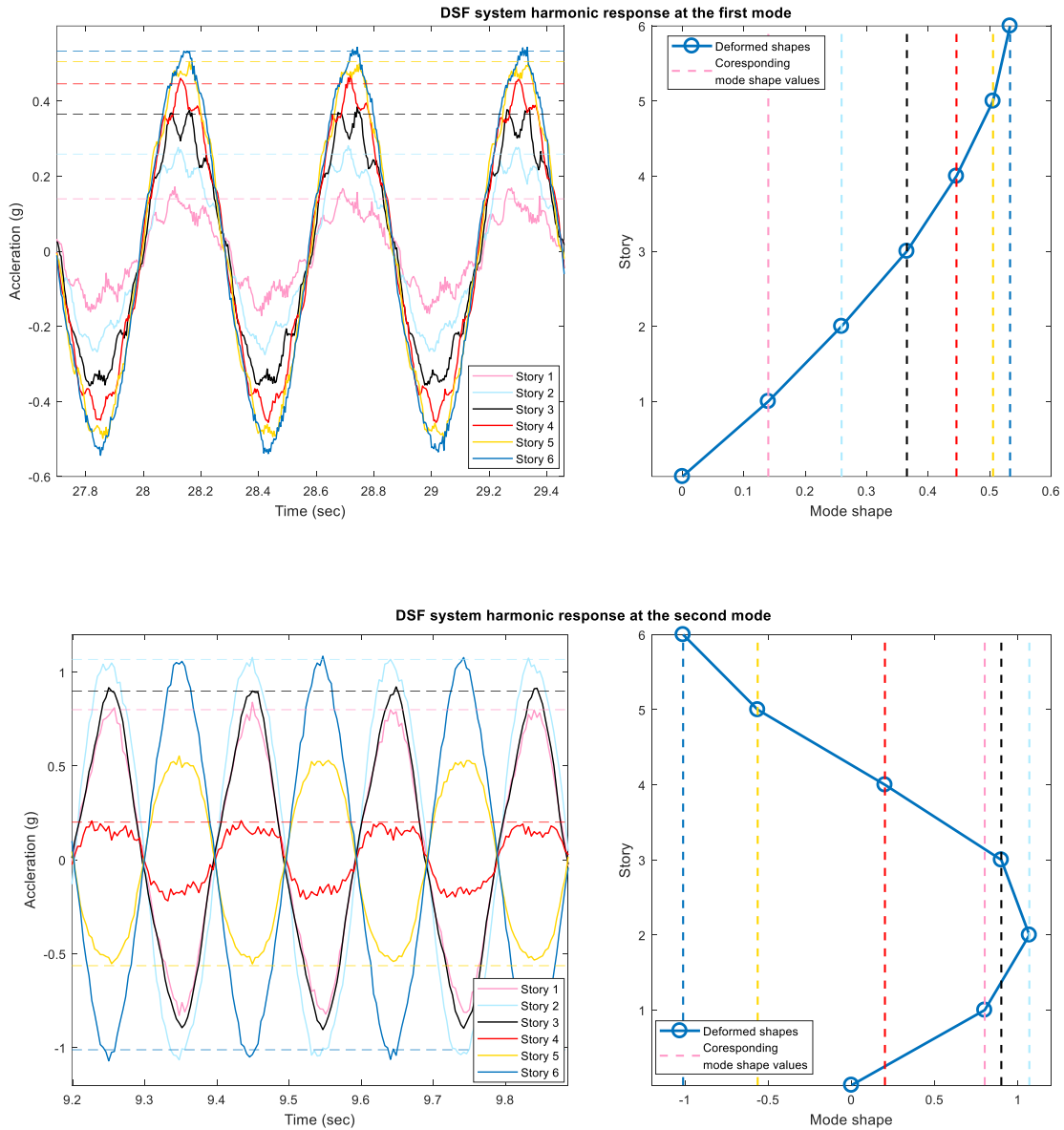





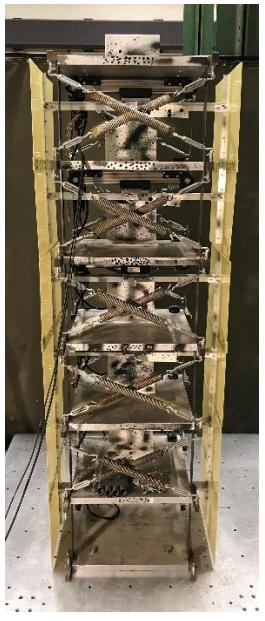


Figure 6.13: DSF system's harmonic response and mode shapes.

6.3 Stiffness estimation

6.3.1 Damage Configurations

Multiple tests were conducted using different damage configurations in the experimental structure. The six testing configurations, as shown in Table 6.3, were (i) healthy, (ii) 6th floor damaged, (iii) 4th floor damaged, (iv) 1st floor damaged, (v) 1st and 4th floors damaged, and (vi) 4th and 6th floors damaged. Spring bracings were removed at those floors to temporarily “damage” the structure on that floor.

Table 6.3: Damage Configurations for DSF configuration (Shaded Floors Are Damaged).

| Configuration 1: Healthy Structure | Configuration 2: 6 th Floor Damaged | Configuration 3: 4 th Floor Damaged | | | | | | | | | | | | | | | | | | |
|---|--|--|---|---|---|---|--|---|---|---|---|---|---|--|---|---|---|---|---|---|
|  <table border="1" style="display: inline-table; vertical-align: middle;"> <tr><td>6</td></tr> <tr><td>5</td></tr> <tr><td>4</td></tr> <tr><td>3</td></tr> <tr><td>2</td></tr> <tr><td>1</td></tr> </table> | 6 | 5 | 4 | 3 | 2 | 1 |  <table border="1" style="display: inline-table; vertical-align: middle;"> <tr style="background-color: red;"><td>6</td></tr> <tr><td>5</td></tr> <tr><td>4</td></tr> <tr><td>3</td></tr> <tr><td>2</td></tr> <tr><td>1</td></tr> </table> | 6 | 5 | 4 | 3 | 2 | 1 |  <table border="1" style="display: inline-table; vertical-align: middle;"> <tr><td>6</td></tr> <tr><td>5</td></tr> <tr style="background-color: red;"><td>4</td></tr> <tr><td>3</td></tr> <tr><td>2</td></tr> <tr><td>1</td></tr> </table> | 6 | 5 | 4 | 3 | 2 | 1 |
| 6 | | | | | | | | | | | | | | | | | | | | |
| 5 | | | | | | | | | | | | | | | | | | | | |
| 4 | | | | | | | | | | | | | | | | | | | | |
| 3 | | | | | | | | | | | | | | | | | | | | |
| 2 | | | | | | | | | | | | | | | | | | | | |
| 1 | | | | | | | | | | | | | | | | | | | | |
| 6 | | | | | | | | | | | | | | | | | | | | |
| 5 | | | | | | | | | | | | | | | | | | | | |
| 4 | | | | | | | | | | | | | | | | | | | | |
| 3 | | | | | | | | | | | | | | | | | | | | |
| 2 | | | | | | | | | | | | | | | | | | | | |
| 1 | | | | | | | | | | | | | | | | | | | | |
| 6 | | | | | | | | | | | | | | | | | | | | |
| 5 | | | | | | | | | | | | | | | | | | | | |
| 4 | | | | | | | | | | | | | | | | | | | | |
| 3 | | | | | | | | | | | | | | | | | | | | |
| 2 | | | | | | | | | | | | | | | | | | | | |
| 1 | | | | | | | | | | | | | | | | | | | | |
| Configuration 4: 1 st Floor Damaged | Configuration 5: 1 st & 4 th Floors Damaged | Configuration 6: 6 th & 4 th Floors Damaged | | | | | | | | | | | | | | | | | | |
|  <table border="1" style="display: inline-table; vertical-align: middle;"> <tr><td>6</td></tr> <tr><td>5</td></tr> <tr><td>4</td></tr> <tr><td>3</td></tr> <tr><td>2</td></tr> <tr style="background-color: red;"><td>1</td></tr> </table> | 6 | 5 | 4 | 3 | 2 | 1 |  <table border="1" style="display: inline-table; vertical-align: middle;"> <tr><td>6</td></tr> <tr><td>5</td></tr> <tr style="background-color: red;"><td>4</td></tr> <tr><td>3</td></tr> <tr><td>2</td></tr> <tr style="background-color: red;"><td>1</td></tr> </table> | 6 | 5 | 4 | 3 | 2 | 1 |  <table border="1" style="display: inline-table; vertical-align: middle;"> <tr style="background-color: red;"><td>6</td></tr> <tr><td>5</td></tr> <tr style="background-color: red;"><td>4</td></tr> <tr><td>3</td></tr> <tr><td>2</td></tr> <tr><td>1</td></tr> </table> | 6 | 5 | 4 | 3 | 2 | 1 |
| 6 | | | | | | | | | | | | | | | | | | | | |
| 5 | | | | | | | | | | | | | | | | | | | | |
| 4 | | | | | | | | | | | | | | | | | | | | |
| 3 | | | | | | | | | | | | | | | | | | | | |
| 2 | | | | | | | | | | | | | | | | | | | | |
| 1 | | | | | | | | | | | | | | | | | | | | |
| 6 | | | | | | | | | | | | | | | | | | | | |
| 5 | | | | | | | | | | | | | | | | | | | | |
| 4 | | | | | | | | | | | | | | | | | | | | |
| 3 | | | | | | | | | | | | | | | | | | | | |
| 2 | | | | | | | | | | | | | | | | | | | | |
| 1 | | | | | | | | | | | | | | | | | | | | |
| 6 | | | | | | | | | | | | | | | | | | | | |
| 5 | | | | | | | | | | | | | | | | | | | | |
| 4 | | | | | | | | | | | | | | | | | | | | |
| 3 | | | | | | | | | | | | | | | | | | | | |
| 2 | | | | | | | | | | | | | | | | | | | | |
| 1 | | | | | | | | | | | | | | | | | | | | |

6.3.2 Least Square Stiffness Estimate

After finding the modal parameters of the structure, the structural stiffnesses can be estimated using a least square estimate (Caicedo *et al.*, 2001). A one-directional six-story shear structure has the following equation of motion:

$$\mathbf{M}\ddot{\mathbf{x}} + \mathbf{C}\dot{\mathbf{x}} + \mathbf{K}\mathbf{x} = \mathbf{u} \quad (6.1)$$

with the mass and stiffness matrices as

$$\mathbf{M} = \begin{bmatrix} m_1 & 0 & 0 & 0 & 0 & 0 \\ 0 & m_2 & 0 & 0 & 0 & 0 \\ 0 & 0 & m_3 & 0 & 0 & 0 \\ 0 & 0 & 0 & m_4 & 0 & 0 \\ 0 & 0 & 0 & 0 & m_5 & 0 \\ 0 & 0 & 0 & 0 & 0 & m_6 \end{bmatrix} \quad \text{and} \quad (6.2)$$

$$\mathbf{K} = \begin{bmatrix} k_1+k_2 & -k_2 & 0 & 0 & 0 & 0 \\ -k_2 & k_2+k_3 & -k_3 & 0 & 0 & 0 \\ 0 & -k_3 & k_3+k_4 & -k_4 & 0 & 0 \\ 0 & 0 & -k_4 & k_4+k_5 & -k_5 & 0 \\ 0 & 0 & 0 & -k_5 & k_5+k_6 & -k_6 \\ 0 & 0 & 0 & 0 & -k_6 & k_6 \end{bmatrix} \quad (6.3)$$

, respectively. The damping matrix, \mathbf{C} , takes a similar form as \mathbf{K} ; $\mathbf{x} = [x_1 \ x_2 \ \dots \ x_6]^T$ is the displacement vector; and \mathbf{u} is the external force vector.

Mass and stiffness matrices can be estimated from modal parameters (eigen-frequencies, λ_j , and mode shapes, Φ_j) of the structure. First, (6.1) can be expressed as an eigenvalue problem:

$$(\mathbf{K} - \lambda_j \mathbf{M})\Phi_j = 0 \quad . \quad (6.4)$$

(6.4) can be rearranged to

$$\mathbf{K}\Phi_j = \lambda_j \mathbf{M}\Phi_j, j = 1:6 \quad \text{and} \quad (6.5)$$

$$\begin{bmatrix} \phi_{1,j} + \phi_{2,j} & -\phi_{2,j} & 0 & 0 & 0 & 0 \\ -\phi_{2,j} & \phi_{2,j} + \phi_{3,j} & -\phi_{3,j} & 0 & 0 & 0 \\ 0 & -\phi_{3,j} & \phi_{3,j} + \phi_{4,j} & -\phi_{4,j} & 0 & 0 \\ 0 & 0 & -\phi_{4,j} & \phi_{4,j} + \phi_{5,j} & -\phi_{5,j} & 0 \\ 0 & 0 & 0 & -\phi_{5,j} & \phi_{5,j} + \phi_{6,j} & -\phi_{6,j} \\ 0 & 0 & 0 & 0 & -\phi_{6,j} & \phi_{6,j} \end{bmatrix} \begin{bmatrix} k_1 \\ k_2 \\ k_3 \\ k_4 \\ k_5 \\ k_6 \end{bmatrix} = \begin{bmatrix} \phi_{1,j} \lambda_j m_1 \\ \phi_{2,j} \lambda_j m_2 \\ \phi_{3,j} \lambda_j m_3 \\ \phi_{4,j} \lambda_j m_4 \\ \phi_{5,j} \lambda_j m_5 \\ \phi_{6,j} \lambda_j m_6 \end{bmatrix}. \quad (6.6)$$

Once eigen-frequencies and mode shapes are obtained from modal analysis, the stiffness values in \mathbf{K} can be solved for any particular eigenvalue and eigenvector by pre-multiplying both sides of (6.6) with the inverse of the matrix of Φ values. Using a least square approach, the overall structural stiffnesses can be estimated from the eigenvalues and corresponding eigenvectors.

Structural damage can be detected once stiffness changes observed in the structure. To compute stiffness changes in the structure, the following equation was used to compare relative percentage changes of the stiffness values with respect to the healthy structure:

$$\Delta \hat{k}_i(\%) = \left(\frac{\hat{k}_{i,damaged}}{\hat{k}_{i,healthy}} - 1 \right) \times 100 \quad (6.7)$$

where $\hat{k}_{i,damaged}$ and $\hat{k}_{i,healthy}$ are the estimated stiffness values of the i -th floor in the damaged and healthy structure, respectively.

6.4 Results Discussion

In the experiments, the first and second modes were excited for the AMD, DMD and DSF systems. The structural mode shapes were estimated based on the steady state acceleration response measured by accelerometers. SHM analyses was performed on multiple damage configurations described in Table 6.3. Based on the structural modal parameters, the structural stiffness values were estimated using (6.6). Structural damage could be detected by changes in the stiffness values of the structure and the percent changes per floor was calculated using (6.7). Stiffness estimations from the AMD, DMD and DSF systems are displayed in Tables 6.5, Table 6.6 and Table 6.7 respectively.

Table 6.4 helps define damage identification statuses and their corresponding color shades used in Table 6.5, Table 6.6 and Table 6.7. Actual damage floors are emboldened.

Table 6.4: Definition of the damage identification status and their corresponding color shade.





| Status | Definition | Color Shades |
|-------------------|--|---|
| Damage identified | Actual damage locations detected (CORRECT) |  |
| False positive | No damage at this position but the result indicated that damage occurred (INNOCORECT)($>1.00\%$ stiffness decrease) |  |
| False negative | Actual damage at this position but the result indicated that damage did not occur (INCORRECT) |  |
| No damage | No damage at this position and the result indicated that damage did not occur (CORRECT) |  |

Table 6.5: Stiffnesses (N/mm) estimated for the AMD system excited at the first and second modes.

| AMD system excited at the first mode | | | | | | | | | | | |
|---------------------------------------|---------|--------|---------|--------|---------|--------|---------|-------------|---------|-------------|---------|
| Damage pattern | Healthy | 6th | | 4th | | 1st | | 4th and 6th | | 1st and 4th | |
| Freq. (Hz) | 1.578 | 1.578 | | 1.574 | | 1.578 | | 1.570 | | 1.570 | |
| Floor | Stiff. | Stiff. | Diff. | Stiff. | Diff. | Stiff. | Diff. | Stiff. | Diff. | Stiff. | Diff. |
| 1 | 40.46 | 40.68 | 0.52% | 41.00 | 1.31% | 36.32 | -10.23% | 42.1 | 4.03% | 36.95 | -8.68% |
| 2 | 40.66 | 40.88 | 0.55% | 40.67 | 0.03% | 42.44 | 4.4% | 41.48 | 2.04% | 42.82 | 5.32% |
| 3 | 41.11 | 41.19 | 0.19% | 43.04 | 4.7% | 43.12 | 4.89% | 42.36 | 3.04% | 45.07 | 9.64% |
| 4 | 40.32 | 40.29 | -0.07% | 36.08 | -10.53% | 44.38 | 10.08% | 34.54 | -14.34% | 36.58 | -9.28% |
| 5 | 36.52 | 37 | 1.31% | 37.43 | 2.48% | 35.72 | -2.2% | 37.61 | 2.98% | 40.09 | 9.76% |
| 6 | 31.95 | 26.96 | -15.6% | 33.6 | 5.17% | 37.16 | 16.34% | 29.32 | -8.21% | 40.41 | 26.49% |
| AMD system excited at the second mode | | | | | | | | | | | |
| Damage pattern | Healthy | 6th | | 4th | | 1st | | 4th and 6th | | 1st and 4th | |
| Freq. (Hz) | 5.406 | 5.398 | | 5.398 | | 5.406 | | 5.398 | | 5.398 | |
| Floor | Stiff. | Stiff. | Diff. | Stiff. | Diff. | Stiff. | Diff. | Stiff. | Diff. | Stiff. | Diff. |
| 1 | 35.88 | 37.82 | 5.42% | 27.35 | -23.75% | 27.92 | -22.16% | 38.76 | 8.03% | 34.03 | -5.14% |
| 2 | 25.24 | 37.76 | 49.57% | 15.97 | -36.72% | 3.55 | -85.95% | 38.42 | 52.21% | 39.43 | 56.21% |
| 3 | 69.11 | 44.6 | -35.46% | 62.27 | -9.89% | 76.51 | 10.72% | 38.74 | -43.94% | 41.51 | -39.93% |
| 4 | 55.63 | 43.14 | -22.46% | 41.7 | -25.04% | 72.66 | 30.61% | 31.81 | -42.83% | 33.69 | -39.44% |
| 5 | 55.66 | 42.27 | -24.06% | 49.2 | -11.61% | 60.69 | 9.03% | 34.64 | -37.77% | 36.92 | -33.67% |
| 6 | 64.13 | 38.87 | -39.38% | 64.42 | 0.45% | 92 | 43.47% | 27.01 | -57.89% | 37.21 | -41.97% |

Table 6.6: Stiffnesses (N/mm) estimated for the DMD system excited at the first and second modes.

| DMD system excited at the first mode | | | | | | | | | | | |
|---------------------------------------|---------|--------|---------|--------|---------|--------|---------|-------------|---------|-------------|---------|
| Damage pattern | Healthy | 6th | | 4th | | 1st | | 4th and 6th | | 1st and 4th | |
| Freq. (Hz) | 1.688 | 1.68 | | 1.672 | | 1.578 | | 1.570 | | 1.570 | |
| Floor | Stiff. | Stiff. | Diff. | Stiff. | Diff. | Stiff. | Diff. | Stiff. | Diff. | Stiff. | Diff. |
| 1 | 40.64 | 39.80 | -2.07% | 42.61 | 4.84% | 36.13 | -11.09% | 41.97 | 3.27% | 37.73 | -7.15% |
| 2 | 40.63 | 38.27 | -5.79% | 43.22 | 6.39% | 43.42 | 6.87% | 41.83 | 2.95% | 43.56 | 7.22% |
| 3 | 56.11 | 60.05 | 7.01% | 53.4 | -4.84% | 52.28 | -6.84% | 57.76 | 2.92% | 56.11 | 0.00% |
| 4 | 52.44 | 53.57 | 2.16% | 45.64 | -12.97% | 54.85 | 4.58% | 47.06 | -10.26% | 47.02 | -10.34% |
| 5 | 49.55 | 49.66 | 0.22% | 49.37 | -0.36% | 49.13 | -0.86% | 51.34 | 3.6% | 50.54 | 1.99% |
| 6 | 53.72 | 47.10 | -12.31% | 55.85 | 3.97% | 56.79 | 5.73% | 48.36 | -9.98% | 59.46 | 10.7% |
| DMD system excited at the second mode | | | | | | | | | | | |
| Damage pattern | Healthy | 6th | | 4th | | 1st | | 4th and 6th | | 1st and 4th | |
| Freq. (Hz) | 4.906 | 4.883 | | 4.891 | | 4.781 | | 4.852 | | 4.813 | |
| Floor | Stiff. | Stiff. | Diff. | Stiff. | Diff. | Stiff. | Diff. | Stiff. | Diff. | Stiff. | Diff. |
| 1 | 37.36 | 39.80 | 1.24% | 38.33 | 2.61% | 31.56 | -15.51% | 40.01 | 7.10% | 34.49 | -7.67% |
| 2 | 35.64 | 38.27 | 5.95% | 38.41 | 7.78% | 34.7 | -2.64% | 40.03 | 12.32% | 37.5 | 5.22% |
| 3 | 44.62 | 60.05 | -0.05% | 42.73 | -4.24% | 45.74 | 2.51% | 44.15 | -1.06% | 43.24 | -3.09% |
| 4 | 41.93 | 53.57 | 2.88% | 37.32 | -10.98% | 43.4 | 3.52% | 38.3 | -8.64% | 38.84 | -7.37% |
| 5 | 42.31 | 49.66 | -0.08% | 43.05 | 1.75% | 43.74 | 3.39% | 44.43 | 5.02% | 41.04 | -3.00% |
| 6 | 45.76 | 47.10 | -15.06% | 47.36 | 3.48% | 47.27 | 3.28% | 39.8 | -13.03% | 48.27 | 5.48% |

Table 6.7: Stiffnesses (N/mm) estimated for the DSF system excited at the first and second modes.

| DSF system excited at the first mode | | | | | | | | | | | |
|---------------------------------------|---------|--------|----------------|--------|----------------|--------|----------------|-------------|----------------|-------------------------|----------------|
| Damage pattern | Healthy | 6th | | 4th | | 1st | | 4th and 6th | | 1st and 4th | |
| Freq. (Hz) | 1.727 | 1.711 | | 1.699 | | 1.672 | | 1.699 | | 1.672 | |
| Floor | Stiff. | Stiff. | Diff. | Stiff. | Diff. | Stiff. | Diff. | Stiff. | Diff. | Stiff. | Diff. |
| 1 | 43.68 | 43.61 | -0.16% | 43.75 | 0.17% | 43.68 | -13.45% | 44.23 | 1.27% | 44.23 | -16.34% |
| 2 | 48.04 | 48.29 | 0.53% | 48.83 | 1.64% | 48.04 | 0.21% | 48.38 | 0.71% | 48.38 | 0.69% |
| 3 | 46.96 | 50.24 | 6.97% | 47.47 | 1.08% | 46.96 | 1.63% | 47.75 | 1.68% | 47.75 | 5.58% |
| 4 | 49.93 | 51.95 | 4.05% | 42.6 | -14.68% | 49.93 | 0.09% | 42.96 | -13.97% | 42.96 | -11.16% |
| 5 | 47.44 | 49.92 | 5.23% | 48.32 | 1.87% | 47.44 | 0.96% | 48.02 | 1.22% | 48.02 | 1.38% |
| 6 | 52.4 | 41.94 | -19.96% | 50.14 | -4.32% | 52.4 | -3.14% | 41.97 | -19.91% | 41.97 | -5.98% |
| DSF system excited at the second mode | | | | | | | | | | | |
| Damage pattern | Healthy | 6th | | 4th | | 1st | | 4th and 6th | | 1st and 4 th | |
| Freq. (Hz) | 5.102 | 5.063 | | 5.059 | | 5.047 | | 5.000 | | 5.010 | |
| Floor | Stiff. | Stiff. | Diff. | Stiff. | Diff. | Stiff. | Diff. | Stiff. | Diff. | Stiff. | Diff. |
| 1 | 40.64 | 39.8 | -2.07% | 42.61 | 4.84% | 36.13 | -11.09% | 41.97 | 3.27% | 37.73 | -7.15% |
| 2 | 40.63 | 38.27 | -5.79% | 43.22 | 6.39% | 43.42 | 6.87% | 41.83 | 2.95% | 43.56 | 7.22% |
| 3 | 56.11 | 60.05 | 7.01% | 53.4 | -4.84% | 52.28 | -6.84% | 57.75 | 2.92% | 56.11 | 0.00% |
| 4 | 52.44 | 53.57 | 2.16% | 45.64 | -12.97% | 54.85 | 4.58% | 47.06 | -10.26% | 47.02 | -10.34% |
| 5 | 49.55 | 49.66 | 0.22% | 49.37 | -0.36% | 49.13 | -0.86% | 51.34 | 3.60% | 50.54 | 1.99% |
| 6 | 53.72 | 47.1 | -12.31% | 55.85 | 3.97% | 56.79 | 5.73% | 48.36 | -9.98% | 59.46 | 10.7% |

By comparing stiffness values estimated from healthy and damaged structures, it was possible to identify structural damage. From Table 6.5, the AMD system was able to detect the all damaged stories at the first mode. However, the second mode excited by the AMD is not dependable; there are significant stiffness estimate errors for false positives, indicating damage at healthy floors. As shown in Tables 6.6 and 6.7, the DMD and DSF systems could identify the all damaged stories at both first and second modes. Although estimate errors for false positives exist, the errors indicates stiffness loss are under 6% which is smaller compare to the estimated

actual damage decrease stories which is greater than 9%, the success in identification of the stiffness loss verified the accuracy of the mode shapes obtained from DMD and DSF excitation.

Combining the first and second modal parameters, the stiffness of the structural can be estimated through a least square stiffness estimation using (6.6). Based on the least square stiffness estimation of the first two modes, Table 6.8 and 6.9 show the estimated stiffness values of the DMD and DSF systems, respectively, and the percent decreases from the healthy structures. Damaged floors are emboldened and the percent decrease of stiffness per floor was calculated using (6.7).

By comparing stiffness values estimated from healthy and damaged structures, damage location could be detected in both DMD and DSF systems. By combining the first two modes to estimate stiffness values, the false positive errors had largely been eliminated compared to estimates from individual modes shown in Tables 6.6 and 6.7. The results shown in Tables 6.8 and 6.9 show that the proposed DSF system had comparable results to the DMD system in terms of detecting stiffness changes.

Table 6.8: DMD configuration estimated stiffness, N/mm (% change from the healthy structure).

| Configuration | 1 | 2 | 3 | 4 | 5 | 6 |
|----------------|----------------|----------------------------------|--------------------------|----------------------------------|----------------------------------|-----------------------------------|
| Damaged Floors | None (Healthy) | 6th | 4th | 1st | 4 th & 6th | 1 st & 4 th |
| Floor 1 | 42.19 (0%) | 41.93 (-0.61%) | 42.15 (-0.10%) | 34.96 (-17.13%) | 42.88 (1.64%) | 36.5 (-13.59%) |
| Floor 2 | 42.73 (0%) | 43.30 (1.35%) | 43.27 (1.28%) | 42.03 (-1.63%) | 43.69 (2.25%) | 44.18 (3.40%) |
| Floor 3 | 43.15 (0%) | 45.25 (4.86%) | 45.11 (4.55%) | 43.67 (1.22%) | 44.35 (5.11%) | 46.17 (7.01%) |
| Floor 4 | 44.18 (0%) | 46.02 (4.16%) | 40.24 (-8.91%) | 44.38 (0.45%) | 40.27 (-8.85%) | 40.70 (-7.88%) |
| Floor 5 | 45.10 (0%) | 45.42 (0.70%) | 46.57 (3.24%) | 45.23 (0.29%) | 46.89 (3.95%) | 44.95 (-0.34%) |
| Floor 6 | 48.95 (0%) | 41.82 (-14.58%) | 51.26 (4.71%) | 49.05 (0.20%) | 42.04 (-14.12%) | 52.61 (7.47%) |

Table 6.9: DSF configuration estimated stiffness, N/mm (% change from the healthy structure).

| Configuration | 1 | 2 | 3 | 4 | 5 | 6 |
|----------------|----------------|----------------------------------|----------------------------------|----------------------------------|----------------------------------|-----------------------------------|
| Damaged Floors | None (Healthy) | 6th | 4th | 1st | 4 th & 6th | 1 st & 4 th |
| Floor 1 | 43.76 (0%) | 43.41 (-0.79%) | 44.22 (1.05%) | 37.90 (-13.37%) | 43.83 (0.18%) | 39.13 (-10.57%) |
| Floor 2 | 47.49 (0%) | 46.83 (-1.39%) | 47.90 (0.87%) | 47.88 (0.81%) | 47.24 (-0.54%) | 48.84 (2.85%) |
| Floor 3 | 47.42 (0%) | 49.74 (4.90%) | 47.38 (-0.09%) | 48.06 (1.35%) | 47.95 (1.11%) | 50.18 (5.81%) |
| Floor 4 | 50.19 (0%) | 51.12 (1.85%) | 43.92 (-12.49%) | 52.46 (4.54%) | 44.18 (-11.96%) | 45.47 (-9.41%) |
| Floor 5 | 48.37 (0%) | 48.52 (0.30%) | 49.83 (3.01%) | 48.84 (0.97%) | 49.12 (1.54%) | 49.41 (2.15%) |
| Floor 6 | 53.33 (0%) | 46.27 (-13.24%) | 54.12 (1.47%) | 56.13 (5.23%) | 46.49 (-12.83%) | 54.17 (1.56%) |

6.5 Conclusion

In this experiment, a six-story model structure with motorized (“active”) mass dampers was tested with five damage patterns to demonstrate accurate damage detection. Acceleration responses were measured by 12-bit wireless accelerometers (Microstrain G-link) installed on each floor. By programming the motors, the actuators were synced and excited specific structural modes to amplify structural responses. The amplified structural responses improved signal-to-noise levels. Different actuator configurations of the AMD, DMD and DSF systems were tested and compared. For each mode of the structures, modal parameters and floor stiffness values were estimated based on the steady state response. The AMD system was able to identify the structural stiffnesses based on the first mode but failed to identify the structural stiffnesses at the second mode. For DMD and DSF system, it was shown that exciting the structures with the directions of actuator forces following mode shape directions could greatly improve the accuracy of modal parameter estimations. Utilizing combinations of the DMD’s and DSF’s multiple active dampers to target structural modes of interest, multiple structural modes could be excited and the damage patterns in structures were successfully detected. Although the interaction between the dampers (façade panels) and the structure becomes more complex in DSF system compared to the DMD system, the proposed SHM methods could achieve comparable stiffness identification results in both the DSF and DMD systems.

Chapter 7 Conclusion

7.1 Conclusion

In this dissertation, an innovative system integrating double skin façades (DSF) and mass damper was analyzed. By motorizing DSFs, the movable façade system can improve energy efficiency by adjusting the airflow between the skin façades. Previous studies showed that heating loads typically decrease with small DSF cavity depths (slow airflow in the cavity) and cooling loads are minimized with large DSF cavity depths (fast airflow in the cavity).

In addition to energy efficiency, the resulting DSF mass damper system can significantly reduce structural motions under earthquake excitation. Shake table experiments were conducted in which a scaled six-story structure with DSF dampers was subjected to historical earthquake records. Both the actively and passively controlled DSF mass damper systems were shown to significantly reduce structural motions. The passive controlled DSF damper systems was shown to mostly outperform a conventional tuned mass damper system with an equivalent damper mass ratio. While under the active control strategies, DSF damper systems outperformed a conventional active mass damper system with the same damper mass ratio and same level of control force.

Moreover, the actuators and sensors installed for the active control system were also used to excite the structure for structural health monitoring (SHM) purposes. Utilizing DSF's multiple active dampers to target structural modes of interest, multiple structural modes could be excited and various damage patterns in structures were successfully detected. Given that SHM systems require hundreds of sensors that are costly to install, this dissertation also looks to reduce the

installation cost of SHM by using smartphones as alternative sensors. Though smartphones had inconsistent sampling rate, experiment results showed that the smartphones successfully detected all the damage cases.

This research utilizes DSF, which is an established architecture competent, by using an integrated approach to balance the objectives of providing hazard safety, saving energy, and achieving a cost-effective and sustainable design solution. The synergy of the integrated system comes not only from its individual functions but also their utilization. SC systems are used only during the infrequent recurrence of strong motions; SHM systems are used to periodically assess structural integrity; and EC systems are in constant use to provide continuous comfort for building occupants. In other words, the proposed integrated system will perform environmental control most of the time and switch to SC and/or SHM when needed and, thus, provide a synergistic tri-purpose system to improve building energy efficiency and enhance structural and life safety.

7.2 Limitations and Future Work

The integrative smart building system proposed in this dissertation provides an innovative concept, while only studied under the limited conditions. A numerical analysis of the proposed system was previously demonstrated to be effective in reducing vibrations during strong motions (Fu and Zhang 2016). Under an experimental setting, this dissertation focuses on experimental verification of the Structural Control (SC) and Structural Health Monitoring (SHM) systems on a scaled six-story shear structure in one direction. The Environmental Control (EC) system was investigated through literature studies. To prove the values of the integrative design, future studies are needed to account for more realistic building conditions, as summarized below:

- In this study, the SC and SHM aspects of the DSF damper system were experimented in one direction only. In SC experiments, since the shake table in this study was unidirectional, the DSF damper system acted alongside the shake table stroke and could only reduce vibrations in one direction. In earthquakes, strong motions can occur in multiple directions. To account for excitations of multiple directions, the SC aspect of the DSF damper system should be further expanded to two-directional. Mover, the SHM aspect can also benefited from the two-directional installation of the DSF damper system; the actuators can excite bi-directionally to target the structure's modes in different directions including torsional modes.
- The scalability and expandability of the DSF damper system also should be further verified on larger scale even full scale building models. Given that more sensor units are likely to be installed on a larger scale structure, the capacity of the data aggregator and

the processing power of controller shall be examined. Due to the cost constraint and physical limitation of this study, only one actuator was installed at each floor to motorize the façade damper. Given the heavy weight of the façade damper, when expanding to larger scale structures, multiples actuators must be installed at each floor to connect to the façade damper.

- The constructability of using DSF glass panels as mass dampers should be carefully investigated. The breakage and detachment of heavy façade panels in seismic events can be severe threats to life safety; it also comprises the effectiveness of the DSF damper. In this study, movement is allowed in DSF outer facade panel while it spanning and connecting to multiple floors. To guarantee the façade strength in the experiments, the movable outer facade panel are modeled with the fiber glass panels. However, for the DSF damper systems to apply in real world buildings, greater rigidity in the framing assembly shall be considered in the design and installation. In addition, innovations in the materials are granted to improve both the strength and movability of the façade assembly while keeping the aesthetics.
- In active structural control, time delay and data loss problems existed in wireless communication will affect the system robustness when applied to active structural control. Structural control applications have fast sampling rate under the seismic events and, thus, latency and loss of data can considerably affect the control effectiveness. Under extreme conditions, big latency will affect the system stability and loss of data might disable the control system. In the active control study, the laboratory experiment configuration largely eliminated the radio interference in wireless transmission, so a low duty cycle data transmission protocol was adopted. Due to laboratory environment and

hardware selection, the effects of the data packet loss were neglected and transmission latency was factored as one sample delay. However, future research should account for potential wireless data transmission failures, especially under stressful environments during earthquakes. To ensure data transmission, future studies should improve wireless protocols to ensure data transmission while minimizing the time delay.

- This study demonstrated that SHM and SC systems can share the same set of hardware, and SHM and SC systems can be further integrated. In the active control experiments, the control loop included four separate systems: wireless sensors, data aggregator, real-time controller and actuators; the wireless data were collected by data aggregator and parsed in the real-time controller. Future studies should consider integrate the aggregator and controller systems as a single processing unit. This design will further integrates SHM and SC systems to reduce the hardware costs, minimize the system latency, and increase the robustness.
- A decentralized control scheme using the active DSF dampers should be explored. In the current implementation, a centralized data aggregation, processing and control calculation scheme was studied. Given that a large number of sensor and actuator units will be installed in a full scale building, the transmissibility of wireless data will be a challenge. Future studies should consider decentralized schemes. The decentralized design will involve localizing the data sensing and control actuation process within one or a few neighboring DSF damper units.
- Due to the time and cost constraints for the research, the energy efficiency performance with the proposed movable DSF design was investigated through literature studies. From computational fluid dynamics (CFD) and heat transfer simulation modeling, these studies

showed that building heating loads typically decrease with slow airflow in the cavity and cooling loads are minimized with fast airflow in the cavity. By motorizing DSFs, the proposed movable façade system can adjust the airflow between the skin façades and enables energy efficiency improvements. However, due to the complexity of analyzing DSFs, assumptions and limitations existed in these simulations, and, therefore, full-sized experiments are warranted to 1) validate simulation with actual experimental measurements, 2) demonstrate the effect with cavity size adjustments on airflow changes, and 3) correlates the changes in DSF airflow rates to cooling and heating loads. In addition, the energy efficiency performance of the DSF damper system should also be examined in multiple climates to assess its effectiveness.

- For the proposed DSF damper system, the initial installation cost might increase significantly when applied to large scale structures, while the benefits comes in the long term in protecting structural integrity and reducing the building energy consumption. A cost and benefit analysis of the DSF-damper system, accounting for both the structural and environmental effects during the life cycle of a building, should be conducted at the design phase to examine the economic feasibility of the system. In such analysis, an energy simulation should be conducted to quantify the energy savings during the life cycle of the building. On the other hand, a structural simulation should be conducted to evaluate the expected building seismic damage over its life cycle, followed by a quantitative analysis on savings in repair/replacement costs brought by structural control systems. These savings should be compared to the initially installation costs of the DSF damper system.

- By eliminating wiring and lowering installation cost, wireless sensor networks offer major advantages in SHM and SC applications. However, wireless communication demands large power consumption, which is a critical constraint for battery powered wireless sensors. Continued development of sensors with lower energy consumption should be carried out. In addition, building on the successful results of using smartphones for SHM (Appendix), continued development of low noise, high resolution and cost-effective sensing hardware is warranted.

Appendix. Structural health monitoring with smartphones

A.1 Introduction

Structural health monitoring (SHM) assesses a structure's integrity through analyzing structural response data such as accelerations and strains to detect changes in structural characteristics. A key component in SHM is a sensing system that measure structural response data. SHM sensing systems are often complex and costly. This study investigates the use of smartphones as an alternative sensing network and compared them to a commercial wireless sensor system.

Recent studies have verified that smartphone accelerometers are valid options in measuring structural vibrations. In 2013, Kotsakos *et al.* developed a SHM network with several Android based handholding tablet. The tablet is Galaxy tab 2 7.0 equipped with accelerometers and able to record acceleration at a sampling rate of 65 Hz. The system was able to detect the natural frequencies of a structure by using the peak picking method. In 2015, Feng *et al.* compared three smart phone devices, iPhone 3Gs, iPhone 5 and Samsung Galaxy S4 (android), to a reference sensor (PCB Piezotronics NI SCXI-1531). All four devices were mounted to a shake table and accelerations were recorded. The study found the more recent devices could obtain the accelerations better than the older generations. The authors reported the issue of not having time synchronization for the devices. Yu *et al.* (2015) also showed that smartphone devices could obtain accurate structural vibrations. In their study, acceleration data obtain from iPhones were first used to accurately estimate the natural frequency of a pendulum. In addition,

another test, in which four different types of accelerometers were attached to a floor of a three story frame on a shake table, was conducted to compare the accelerations obtained from different devices. The four sensor devices were a wired, wireless accelerometer, smartphone, and an external accelerometer board attached to a smartphone. It was found that all acceleration data compared well to one another.

Min *et al.* (2015) developed a smartphone application to measure the absolute dynamic displacements. The authors used the rear camera of the iPhone 6 Plus to capture the motion of a color-patterned target and convert to absolute displacements in real-time up to 120Hz sampling rate. The performance of the developed smartphone application was validated experimentally with shake table tests, the smartphone showing comparable results with those of conventional laser displacement sensor.

To date, researches using smartphones for SHM purposes focus on validating smartphones' measurement with conventional sensing systems, though natural frequencies of experimental structures were able to be obtained with smartphones, however none current research have applied smartphone for structural damage diagnosis. This project builds on prior efforts and creates a network of time-synchronized smartphones that can measure vibrations and detect structural changes in multiple locations of a structure.

This research project was collaborated with Mr. Kyle Wyatt, a recently graduated Master's student, who developed an Android smartphone application using Java programming. The application allows creating a network of time-synchronized smartphones that can measure vibrations in multiple locations of a structure. This is a crucial development because SHM systems require a network of sensors with accurate time synchronization. The author was mainly responsible for building a test structure and developing a MATLAB code for post processing. A

commercial wireless accelerometers system (list the make and model of the accelerometers) was also introduced to serve as a baseline model. SHM experiments were conducted on the test structure with Kyle. Acceleration data were recorded by both the smartphone system and the wireless accelerometer system for detecting change in the structural properties. Figure A.1 explains and differentiates the collaboration between Kyle and the author. Please note many figures and tables in this chapter are from Kyle’s Master’s thesis (Kyle 2015).

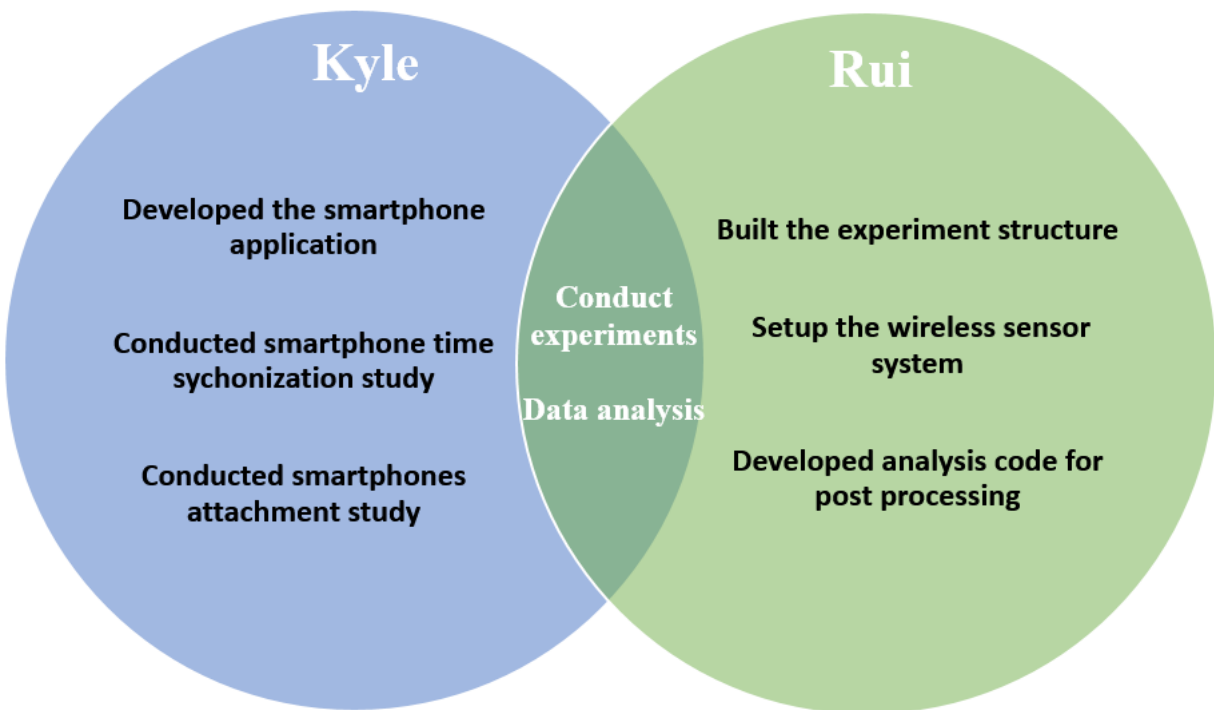


Figure A.1: Contribution of Kyle and the author (Rui).

A.2 Experiment setup

The experimental structure was a six-foot, six-story shear structure mounted on a shake table. The structure used was essentially the same as the “uncontrolled structure” configuration in DSF mass damper experiments; structural details can be find in Section A.2. In order to

simulate “healthy” and “damaged” cases, cross braced springs were installed on the structure to adjust the stiffness at certain floor levels without damaging the main structure; a single cross bracing consisted of one spring, and two turnbuckles (Figure A.2) and they could be easily installed and removed. The stiffness of each spring was 2.35 N/mm (13.41 lb/inch) and total mass of all three components, two turn buckles and one spring was 0.49 kg (1.07 lb). When a story was fully braced, the four cross bracings would add a total of 1.94 kg (4.28 lb).



Figure A.2: Spring and turnbuckles used for cross bracing (Picture credit: Kyle Wyatt 2015).

A healthy structure was fully braced with springs (Figure A.3) and damage was introduced by removing bracing springs at one or more story levels (Figure A.4), when the springs were removed to change the inter-story stiffness, they were taped to the floor from which they were removed to maintain a constant mass for that specific floor.

The testing apparatus was a seismic shake table manufactured by MTS, it has a 4 m (13') × 2.74 m (9') dimension capable of uniaxial shaking at frequencies up to 100 Hz. The hydraulic actuator was capable of generating maximum ground acceleration of 3g at ±7.62 cm (3") stroke.



Figure A.3: Test configuration for a “healthy” structure.

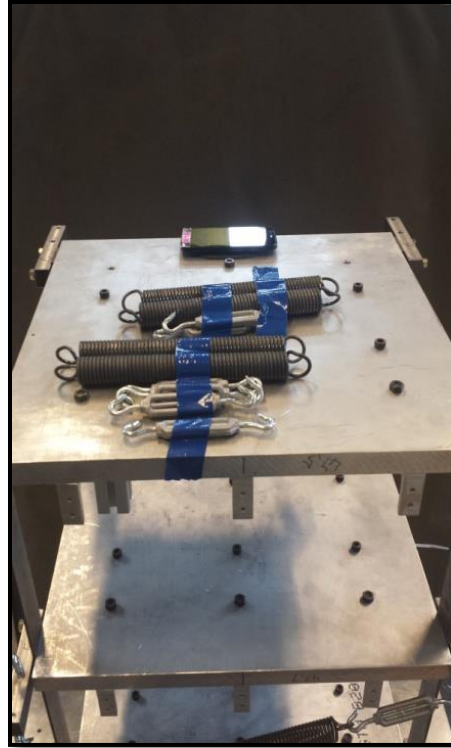


Figure A.4: Test configuration for a damaged floor (6th) case.

A.3 Data acquisition

Acceleration data of each story were recorded by a smartphone (a 2013 Motorola G) and a Microstrain® G-Link® -LXRS® wireless accelerometer (2015). The smartphones with the developed application has the capability to (1) synchronize time between smart phones and (2) record the acceleration data and save it to “.csv” files on board. The Microstrain wireless accelerometer system is a dedicated commercial sensing system and it was introduced to serve as a baseline reference for the smartphone system. Compared to the smartphone system, the Microstrain system contains a data acquisition (DAQ) unit which is capable of auto time

synchronization and recording the acceleration data (Figure A.5). For both system, the collected data were transferred to a computer for SHM analysis.

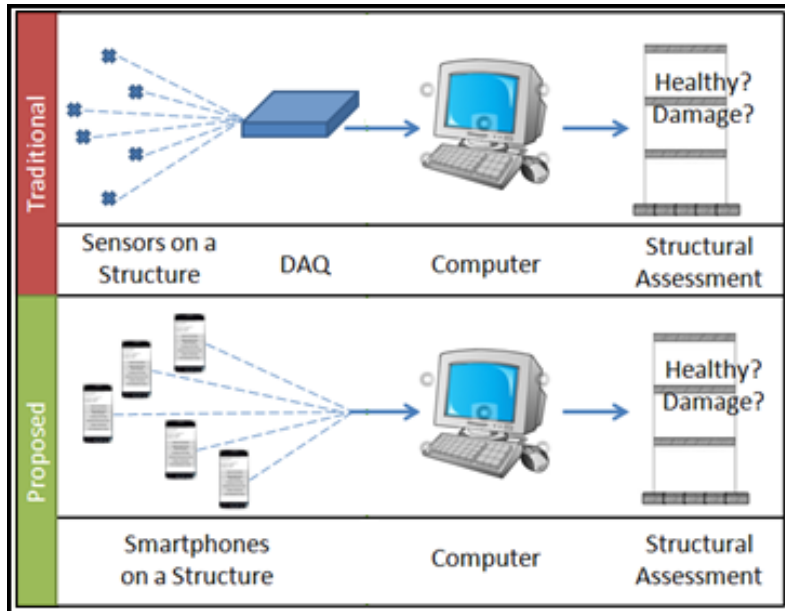




Figure A.5: Difference in workflow comparing wireless accelerometers to smart phones (Kyle, 2015)

The hardware specification and the price of two systems are listed in Table A.1. The proposed smartphone sensing system is an all-inclusive system: they have onboard memory, processors and wireless communication channels and the ability to work separately (such that they can be placed as far away from one another as needed) after they are time-synchronized. Meanwhile, the Microstrain sensors are dependent on a DAQ that costs an additional \$995 (“G-Link®”, 2015) to obtain the data from the sensors. Since the smartphones record data locally and can transmit data directly to a computer, data can be obtained without a DAQ. The Moto G smartphones also cost significantly less than the Microstrain accelerometers. Each Moto G smartphone costs approximately \$180, while each Microstrain accelerometer costs \$545 (“G-Link®”, 2015).







Table A.1: Hardware specification and the price comparison of smartphones and wireless accelerometers.

| | Moto G - 2013 | Microstrain |
|-------------------|---|--|
| Sensor Name | LIS3DH-3-axis Smartphones | G-Link® - LXRS® |
| Sensor Image |  |  |
| Sensor Price: | \$180 | \$545 |
| DAQ Price: | N.A. | \$995 |
| Sensor Range | $\pm 4g$ | $\pm 2g$ |
| Sensor Resolution | 12 bits | 12 bits |
| Sampling Rate | ~ 100 Hz | 128 – 512 Hz |
| Battery | 2070mAh | 220mAh |
| Sensor memory | 8GB | 2MB |
| DAQ memory | N.A. | 2GB |
| Mounting | Sticky pads | Bolt |

A.4 Testing configurations

Multiple tests were conducted using different configurations of damage on the experimental structure. The six testing configurations, as shown in Table A.2, were (i) healthy, (ii) 6th floor damaged, (iii) 4th floor damaged, (iv) 1st floor damaged, (v) 1st and 4th floors damaged, and (vi) 4th and 6th floors damaged. Spring bracing were removed at those levels to temporarily “damage” the structure at that level. The structure was subjected to square wave ground motions to excitation all the vibration modes. For each testing configuration, three shake tests were used.

Table A.2: Damage Configurations (Shaded Floors Are Damaged) (Kyle, 2015).

| Configuration 1: Healthy Structure | Configuration 2: 6 th Floor Damaged | Configuration 3: 4 th Floor Damaged | | | | | | | | | | | | | | | | | | |
|---|--|--|---|---|---|---|---|---|---|---|---|---|---|---|---|---|---|---|---|---|
|  <table border="1" data-bbox="540 390 602 995"> <tr><td>6</td></tr> <tr><td>5</td></tr> <tr><td>4</td></tr> <tr><td>3</td></tr> <tr><td>2</td></tr> <tr><td>1</td></tr> </table> | 6 | 5 | 4 | 3 | 2 | 1 |  <table border="1" data-bbox="930 390 992 995"> <tr><td>6</td></tr> <tr><td>5</td></tr> <tr><td>4</td></tr> <tr><td>3</td></tr> <tr><td>2</td></tr> <tr><td>1</td></tr> </table> | 6 | 5 | 4 | 3 | 2 | 1 |  <table border="1" data-bbox="1304 390 1365 995"> <tr><td>6</td></tr> <tr><td>5</td></tr> <tr><td>4</td></tr> <tr><td>3</td></tr> <tr><td>2</td></tr> <tr><td>1</td></tr> </table> | 6 | 5 | 4 | 3 | 2 | 1 |
| 6 | | | | | | | | | | | | | | | | | | | | |
| 5 | | | | | | | | | | | | | | | | | | | | |
| 4 | | | | | | | | | | | | | | | | | | | | |
| 3 | | | | | | | | | | | | | | | | | | | | |
| 2 | | | | | | | | | | | | | | | | | | | | |
| 1 | | | | | | | | | | | | | | | | | | | | |
| 6 | | | | | | | | | | | | | | | | | | | | |
| 5 | | | | | | | | | | | | | | | | | | | | |
| 4 | | | | | | | | | | | | | | | | | | | | |
| 3 | | | | | | | | | | | | | | | | | | | | |
| 2 | | | | | | | | | | | | | | | | | | | | |
| 1 | | | | | | | | | | | | | | | | | | | | |
| 6 | | | | | | | | | | | | | | | | | | | | |
| 5 | | | | | | | | | | | | | | | | | | | | |
| 4 | | | | | | | | | | | | | | | | | | | | |
| 3 | | | | | | | | | | | | | | | | | | | | |
| 2 | | | | | | | | | | | | | | | | | | | | |
| 1 | | | | | | | | | | | | | | | | | | | | |
| Configuration 4: 1 st Floor Damaged | Configuration 5: 1 st & 4 th Floors Damaged | Configuration 6: 6 th & 4 th Floors Damaged | | | | | | | | | | | | | | | | | | |
|  <table border="1" data-bbox="540 1161 602 1766"> <tr><td>6</td></tr> <tr><td>5</td></tr> <tr><td>4</td></tr> <tr><td>3</td></tr> <tr><td>2</td></tr> <tr><td>1</td></tr> </table> | 6 | 5 | 4 | 3 | 2 | 1 |  <table border="1" data-bbox="930 1161 992 1766"> <tr><td>6</td></tr> <tr><td>5</td></tr> <tr><td>4</td></tr> <tr><td>3</td></tr> <tr><td>2</td></tr> <tr><td>1</td></tr> </table> | 6 | 5 | 4 | 3 | 2 | 1 |  <table border="1" data-bbox="1304 1161 1365 1766"> <tr><td>6</td></tr> <tr><td>5</td></tr> <tr><td>4</td></tr> <tr><td>3</td></tr> <tr><td>2</td></tr> <tr><td>1</td></tr> </table> | 6 | 5 | 4 | 3 | 2 | 1 |
| 6 | | | | | | | | | | | | | | | | | | | | |
| 5 | | | | | | | | | | | | | | | | | | | | |
| 4 | | | | | | | | | | | | | | | | | | | | |
| 3 | | | | | | | | | | | | | | | | | | | | |
| 2 | | | | | | | | | | | | | | | | | | | | |
| 1 | | | | | | | | | | | | | | | | | | | | |
| 6 | | | | | | | | | | | | | | | | | | | | |
| 5 | | | | | | | | | | | | | | | | | | | | |
| 4 | | | | | | | | | | | | | | | | | | | | |
| 3 | | | | | | | | | | | | | | | | | | | | |
| 2 | | | | | | | | | | | | | | | | | | | | |
| 1 | | | | | | | | | | | | | | | | | | | | |
| 6 | | | | | | | | | | | | | | | | | | | | |
| 5 | | | | | | | | | | | | | | | | | | | | |
| 4 | | | | | | | | | | | | | | | | | | | | |
| 3 | | | | | | | | | | | | | | | | | | | | |
| 2 | | | | | | | | | | | | | | | | | | | | |
| 1 | | | | | | | | | | | | | | | | | | | | |

A.5 Post processing

Acceleration data for all six floors were recorded with both the smart phones and the Microstrain wireless accelerometers under different damage configurations. A time domain modal analysis method Eigen-system Realization Algorithm (ERA) is used to estimate the modal parameters (i.e. mode shapes and frequencies). The stiffness of the structure was estimated via a least square method.

From the measured vibration of a structure, modal parameters of the structure could be estimated. This research used Eigensystem Realization Algorithm (ERA) as modal analysis method. The ERA is a widely used time domain modal analysis method; it was developed by Juang and Pappa in 1985. The ERA constructs a state-space representation for an entire structure using impulse response measurements, which can then be used to estimate its modes.

ERA uses singular value decomposition on the Hankel matrix,

$$\mathbf{H}(k-1) = \begin{bmatrix} \mathbf{Y}(k) & \mathbf{Y}(k+1) & \cdots & \mathbf{Y}(k+p) \\ \mathbf{Y}(k+1) & \mathbf{Y}(k+2) & \cdots & \mathbf{Y}(k+p+1) \\ \vdots & \vdots & \ddots & \vdots \\ \mathbf{Y}(k+r) & \mathbf{Y}(k+r+1) & \cdots & \mathbf{Y}(k+p+r) \end{bmatrix} \quad (\text{A.1})$$

where $\mathbf{Y}(k)$ is the pulse response matrix such that $\mathbf{Y}_{ij}(k)$ is the impulse response at the k^{th} time instant collected at the i^{th} location due to an impulsive excitation at the j^{th} location in the structure. The singular value decomposition of $\mathbf{H}(0)$ is denoted by

$$\mathbf{H}(0) = \mathbf{P}\mathbf{D}\mathbf{Q}^T. \quad (\text{A.2})$$

Here, \mathbf{P} and \mathbf{Q}^T are unitary matrices formed by left and right singular vectors respectively and \mathbf{D} is the diagonal matrix formed by the singular values. Singular vectors corresponding to “low” singular values are attributed to noise and the reduced order matrices \mathbf{P}_n , \mathbf{Q}_n and \mathbf{D}_n are generated by using only the singular vectors corresponding to the “high” singular values. The linear system parameters corresponding to the reduced order system can now be estimated using the equations:

$$\mathbf{A} = \mathbf{D}_n^{-1/2} \mathbf{P}_n^T \mathbf{H}(1) \mathbf{Q}_n \mathbf{D}_n^{-1/2} \quad (\text{A.3})$$

$$\mathbf{B} = \mathbf{D}_n^{-1/2} \mathbf{Q}_n^T \mathbf{E}_m \quad (\text{A.4})$$

$$\mathbf{C}_i = \mathbf{E}_n^T \mathbf{P}_n \mathbf{D}_n^{-1/2} \quad (\text{A.5})$$

where $\mathbf{E}_p^T = [\mathbf{I}_p \ \mathbf{0}]$ with \mathbf{I}_p being the identity matrix of order p . The mode shapes of the structure correspond to the columns in the matrix $\mathbf{V} = \mathbf{C}_i \mathbf{\Phi}$, where $\mathbf{\Phi}$ contains the eigenvectors of \mathbf{A} . And the modal frequencies of the structure correspond to the eigenvalues of \mathbf{A} .

After finding the modal parameters of the structure, the structural stiffness can be estimated using a least squares estimate (Caicedo *et al.*, 2001), the procedure followed the stiffness estimation method described in Section 6.3.

A.6 Results Discussion

Figure A.6 compares the time history acceleration of two system. Since the smartphones have the same resolution compared to the Microstrain wireless accelerometers, these two systems should record similar accelerations. The minor difference observed in the graph is majorly the sampling rate difference between two systems. The sampling rate of Microstrain

wireless accelerometers was set to 256Hz in the tests while the smartphones has an inconsistent sampling rate about 100Hz. The consistency between the two systems proved the proposed smartphone is a valid acceleration measurement system as demonstrated in other studies (Kotsakos *et al.*, 2013; Min *et al.*, 2015; Yu *et al.*, 2015).

Sixth Floor Acceleration Comparison

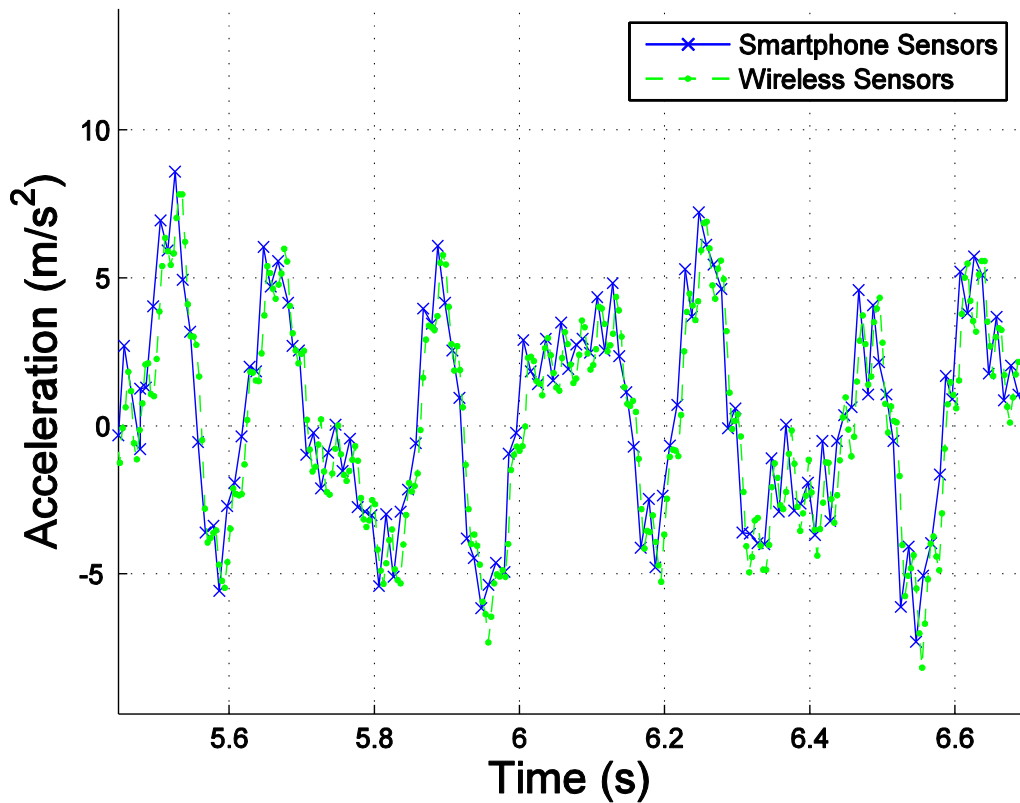


Figure A.6: Microstrain to Smartphone time history acceleration data comparison. (Kyle, 2015)

SHM analysis was performed on multiple test configurations. After acceleration data were obtained from both the smartphone and the Microstrain sensors, they were post processed to detect stiffness changes in the structure.

Stiffness estimations obtained using the least squares estimate from both smartphone and Microstrain sensors are displayed in Table A.3 and Table A.4, respectively. Damaged floors are

emboldened. Both sensing system yielded similar stiffness estimations, showing that the smartphone system was able to closely match the results of the Microstrain system—a dedicated sensing system. To compute stiffness changes in the structure (as measured by the two sensing systems), the following equation was used to compare relative percentage change of stiffness value respect to the healthy:

$$\Delta \hat{k}_i(\%) = \left(\frac{\hat{k}_{i,damaged}}{\hat{k}_{i,healthy}} - 1 \right) \times 100 \quad (A.6)$$

where $\hat{k}_{i,damaged}$ and $\hat{k}_{i,healthy}$ are the estimated stiffness value of the i -th floor on the damaged and healthy structure, respectively.

Table A.3 and Table A.4 show the percent decrease of stiffness per floor using (A.6) in the smartphone and Mircostrain systems, respectively. Damaged floors are again highlighted in green. Both sensors were capable of detecting the damage locations when comparing the healthy and the damage configurations. Generally, the Microstrain sensor estimates had less errors in the non-damaged locations compared to the estimates from the smartphone sensors.

By comparing stiffness values estimated from healthy and damaged structures, it was possible to identify structural damage. In the experiments conducted, the smartphone sensing system could detect structural damage that exceeded 10% drop in stiffness in a floor. Testing proved incorporating smartphones into experimental structural analysis situations could be possible, and improved upon going forward.

Table A.3: Smartphone sensors: estimated stiffness, N/mm (% change from the healthy structure).

| Configuration | 1 | 2 | 3 | 4 | 5 | 6 |
|----------------|----------------|---------------------------------|---------------------------------|---------------------------------|---------------------------------|-----------------------------------|
| Damaged Floors | None (Healthy) | 6th | 4th | 1st | 4 th & 6th | 1 st & 4 th |
| Floor 1 | 43.6 (0%) | 41.5 (-4.82%) | 44.3 (1.61%) | 34.1 (-21.79%) | 46.8 (7.34%) | 36.6 (-16.06%) |
| Floor 2 | 48.0 (0%) | 46.6 (-2.92%) | 47.1 (-1.87%) | 48.7 (1.46%) | 45.0 (-6.25%) | 45.9 (-4.38%) |
| Floor 3 | 44.0 (0%) | 46.2 (5.00%) | 46.6 (5.91%) | 43.4 (-1.36%) | 47.6 (8.18%) | 46.6 (5.91%) |
| Floor 4 | 46.9 (0%) | 44.1 (-5.97%) | 39.9 (-14.93%) | 44.3 (-5.54%) | 37.8 (-19.40%) | 37.3 (-20.47%) |
| Floor 5 | 47.1 (0%) | 49.0 (4.03%) | 48.9 (3.82%) | 45.5 (-3.40) | 49.9 (5.94%) | 49.6 (5.31%) |
| Floor 6 | 50.4 (0%) | 44.3 (-12.10%) | 50.3 (-0.20%) | 50.4 (0.00%) | 43.8 (-13.10%) | 49.9 (-0.99%) |

Comparison of Smartphone and Microstrain Results

Table A.4: Microstrain Sensors: estimated stiffness, N/mm (% change from the healthy structure).

| Configuration | 1 | 2 | 3 | 4 | 5 | 6 |
|----------------|----------------|---------------------------------|---------------------------------|---------------------------------|---------------------------------|-----------------------------------|
| Damaged Floors | None (Healthy) | 6th | 4 th | 1st | 4 th & 6th | 1 st & 4 th |
| Floor 1 | 46.1 (0%) | 45.9 (-0.38%) | 49.7 (7.99%) | 36.4 (-20.91%) | 44.3 (-3.80%) | 37.8 (-17.87%) |
| Floor 2 | 46.4 (0%) | 47.5 (2.26%) | 46.2 (-0.38%) | 47.1 (1.51%) | 46.2 (-0.38%) | 46.1 (-0.76%) |
| Floor 3 | 48.2 (0%) | 46.9 (-2.55%) | 48.2 (0.00%) | 46.8 (-2.91%) | 48.7 (1.09%) | 48.5 (0.73%) |
| Floor 4 | 47.3 (0%) | 47.6 (0.74%) | 41.3 (-12.59%) | 47.3 (0.00%) | 40.5 (-14.44%) | 40.6 (-14.07%) |
| Floor 5 | 48.9 (0%) | 49.2 (0.72%) | 48.7 (-0.36%) | 47.6 (2.51%) | 49.4 (1.08%) | 48.9 (0.00%) |
| Floor 6 | 51.0 (0%) | 44.1 (-13.40%) | 51.1 (0.34%) | 51.5 (1.03%) | 44.5 (-12.72%) | 51.3 (0.69%) |

A.7 Conclusion

To verify a new structural health monitoring (SHM) system based on smartphones, testing was conducted with a scaled six story structure with, a smartphone and a commercial (Microstrain) accelerometer mounted at each floor of the structure. The time history acceleration responses were first compared between the two sensing system and they showed that the two systems recorded similar response data. Then SHM experiments were conducted using the shake table. Five damage configurations were applied to the structure by removing cross bracings at different floor combinations. Acceleration data of Microstrain accelerometers and smartphones were both collected and stiffness values of each floor level were then estimated through a modal analysis technique. The stiffness results from smartphones and Microstrain accelerometers were compared. Given that the smartphones' sampling rate was not as consistent as the one of Microstrain sensors, results from smartphone were not as accurate compared to the Microstrain data. Nonetheless, both data sets could successfully detect all the damage cases.

Since smartphones equipped with built-in accelerometers, network modules and onboard processors, they could eventually provide an alternative to expensive sensing systems because they provide an all-inclusive system capable of forming a sensing network, recording accelerations and eventually performing real-time damage diagnosis on board.

Reference

- Abdel-Rohman M and Leipholz HH. Structural control by pole assignment method. J Eng Mech Div: ASCE 1978; 104: 1159–1175.
- Abe, M., & Fujino, Y. (1994). Dynamic characterization of multiple tuned mass dampers and some design formulas. Earthquake Engineering & Structural Dynamics, 23(8), 813-835.
- Advanced Earthquake Resistant Design Techniques, (2015). Retrieved December 02, 2015, from <http://theconstructor.org/earthquake/earthquake-resistant-techniques/5607/>
- Aly, A. M., Zasso, A., & Resta, F. (2011). Dynamics and control of high-rise buildings under multidirectional wind loads. Smart Materials Research, 2011.
- Balocco, C. (2004). A non-dimensional analysis of a ventilated double façade energy performance. Energy and Buildings, 36(1), 35-40. Retrieved from http://ac.els-cdn.com/S0378778803000860/1-s2.0-S0378778803000860-main.pdf?_tid=73fc70ae-e0d0-11e5-8d30-00000aab0f26&acdnat=1456962340_56a3560f6d427248e51d27315cbe5ff1
- Battaini, M., Yang, G., & Spencer, B. (2000). Bench-scale experiment for structural control. Journal of Engineering Mechanics, 126(2), 140-148.
- Becker, T. C., Yamamoto, S., Hamaguchi, H., Higashino, M., & Nakashima, M. (2015). Application of Isolation to High-Rise Buildings: A Japanese Design Case Study through a US Design Code Lens. Earthquake Spectra, 31(3), 1451-1470.

- Bergman, L., McFarland, D., Hall, J., Johnson, E., & Kareem, A. (1989). Optimal distribution of tuned mass dampers in wind-sensitive structures. Paper presented at the Structural Safety and Reliability.
- Beskyroun, S., Wotherspoon, L., Ma, Q., & Popli, B. (2013). Ambient and forced vibration testing of a 13-story reinforced concrete building. In Proceedings of the New Zealand Society for Earthquake Engineering Conference (NZSEE).
- Brunoro, S., Rinaldi, A., & Sayigh, A. (2011). Double layer glass façade in the refurbishment and architectural renewal of existing buildings in Italy. Paper presented at the World Renewable Energy Congress.
- Buckman, A., Mayfield, M., & BM Beck, S. (2014). What is a smart building? Smart and Sustainable Built Environment, 3(2), 92-109.
- Butterworth, J., Lee, J. H., & Davidson, B. (2004, August). Experimental determination of modal damping from full scale testing. In 13th world conference on earthquake engineering, Vancouver, Paper (Vol. 310).
- CCM Automation Technology (2017). Retrieved July 02, 2017, from <http://www.ccmade.com/>.
- Casciati, S. and Chen, Z.C. (2012), “An active mass damper system for structural control using real-time wireless sensors”, Struct. Control Health Monit., 19(8), 758-767. DOI: 10.1002/stc:1485.
- Chang, J. C., & Soong, T. T. (1980). Structural control using active tuned mass dampers. Journal of the Engineering Mechanics Division, 106(6), 1091-1098.

- Chen, G., & Wu, J. (2001). Optimal placement of multiple tune mass dampers for seismic structures. *Journal of Structural Engineering*, 127(9), 1054-1062.
- Chopra, A. K. (2007). *Dynamics of structures: theory and applications to earthquake engineering*. 2007: Prentice-Hall.
- Chang, J. C., & Soong, T. T. (1980). Structural control using active tuned mass dampers. *Journal of the Engineering Mechanics Division*, 106(6), 1091-1098.
- Chung, L., Reinhorn, A., & Soong, T. (1988). Experiments on active control of seismic structures. *Journal of Engineering Mechanics*, 114(2), 241-256.
- Chung, L., Lin, R., Soong, T., & Reinhorn, A. (1989). Experimental study of active control for MDOF seismic structures. *Journal of Engineering Mechanics*, 115(8), 1609-1627.
- Chung, L., Reinhorn, A., & Soong, T. (1988). Experiments on active control of seismic structures. *Journal of Engineering Mechanics*, 114(2), 241-256.
- Connor, J. J. (2003). *Introduction to structural motion control*. Prentice Hall.
- Constec Engi, Co. (2016) Retrieved February 25, 2016, from <http://www.constec.co.jp/en/seismic/seismic01.html>
- Doyle, J. C., Glover, K., Khargonekar, P. P., & Francis, B. A. (1989). State-space solutions to standard H_2 and H_∞ control problems. *Automatic Control, IEEE Transactions on*, 34(8), 831-847.
- Duke, S. (1996). Acceleration Feedback Control of MDOF Systems. *ASCE., J. Engrg. Mech*, 122, 907 -917.

- Dyke, S., Spencer, B., Quast, P., Kaspari, D., & Sain, M. (1996). Implementation of an active mass driver using acceleration feedback control. *Computer-Aided Civil and Infrastructure Engineering*, 11(5), 305-323.
- Dyke, S., Spencer Jr, B., Sain, M., and Carlson, J. (1998). "An experimental study of MR dampers for seismic protection." *Smart materials and structures*, 7(5), 693.
- Environmental Protection Agency (EPA). (2015). Retrieved December 02, 2015, from <http://www2.epa.gov/greeningepa>
- Frahm, H. (1911). Device for damping vibrations of bodies: Google Patents.
- Franklin, G., Powell, J. and Workman, M. (1998), *Digital Control of Dynamic Systems*, 3rd Ed., California: Ellis-Kagle Press.
- Fu, T. S., Ghosh, A., Johnson, E. A., & Krishnamachari, B. (2013). Energy-efficient deployment strategies in structural health monitoring using wireless sensor networks. *Structural Control and Health Monitoring*, 20(6), 971-986.
- Fu, T. S., & Johnson, E. A. (2010). Distributed mass damper system for integrating structural and environmental controls in buildings. *Journal of Engineering Mechanics*, 137(3), 205-213.
- Fu, T. S., & Johnson, E. A. (2014). Structural health monitoring with a distributed mass damper system. *Structural Control and Health Monitoring*, 21(2), 18
- Fu, T. S., & Zhang, R. (2016). Integrating Double-Skin Façades and Mass Dampers for Structural Safety and Energy Efficiency. *Journal of Architectural Engineering*, 22(4), 04016014.

Tuned Mass Dampers for Bridges, Buildings and other Tall Structures, (2016). Retrieved March 25, 2016, from

<http://www.emda.no/pdf/gerb/13Tuned%20Mass%20Dampers%20for%20Bridges,%20Buildings%20and%20other%20Tall%20Structures.pdf>

Golub, G. H. and C. F. Van Loan, Matrix Computations, Johns Hopkins University Press, Baltimore, 1989, pp. 557-558.

Gracia Cuesta, A. d., Navarro, L., Castell, A., Ruiz-Pardo, Á., Álvarez, S., & Cabeza, L. F. (2013). Experimental study of a ventilated facade with PCM during winter period. Energy and Buildings, 2013, vol. 58, p. 324–332.

Gratia, E., & De Herde, A. (2004). Optimal operation of a south double-skin facade. Energy and Buildings, 36(1), 41-60.

Gratia, E., & De Herde, A. (2007). Greenhouse effect in double-skin facade. Energy and Buildings, 39(2), 199-211.

G-Link® -LXRS®. (2017). Retrieved July 02, 2017, from <http://www.microstrain.com/wireless/g-link>.

Hernandez Tascon, M. (2008). Experimental and computational evaluation of thermal performance and overheating in double skin facades. University of Nottingham.

Hien, W. N., Liping, W., Chandra, A. N., Pandey, A. R., & Xiaolin, W. (2005). Effects of double glazed facade on energy consumption, thermal comfort and condensation for a typical office building in Singapore. Energy and Buildings, 37(6), 563-572.

- Honorius, F. (2016). Tipologie di difesa dalle azioni sismiche: controllo attivo, semi-attivo, passivo, ibrido (In Italian). Retrieved March 22, 2016, from <http://www.strutturista.com/2009/06/tipologie-di-difesa-dalle-azioni-sismiche-controllo-attivo-semi-attivo-passivo-ibrido/>
- Hong, T., Kim, J., Lee, J., Koo, C., & Park, H. S. (2013). Assessment of seasonal energy efficiency strategies of a double skin façade in a monsoon climate region. *Energies*, 6(9), 4352-4376.
- Housner, G.W., Bergman, L.A., Caughey, T.K., Chassiakos, A.G., Claus, R.O., Masri, S.F., Skelton, R.E., Soong, T.T., Spencer, B.F. and Yao, J.T.P. (1997), “Structural control: past, present, and future”, *J. Eng. Mech. - ASCE*, 123(9), 897-972. doi:10.1061/(ASCE)0733-9399(1997)123:9(897).
- Hudson, Donald E. (1962) Synchronized vibration generators for dynamic tests of full-scale structures. California Institute of Technology. (Unpublished)
<http://resolver.caltech.edu/CaltechEERL:1962.EERL.1962.001>
- Igusa, T., & Xu, K. (1994). Vibration control using multiple tuned mass dampers. *Journal of sound and vibration*, 175(4), 491-503.
- Kareem, A., Kijewski, T., & Tamura, Y. (1999). Mitigation of motions of tall buildings with specific examples of recent applications. *Wind and structures*, 2(3), 201-251.
- Kareem, A., & Kline, S. (1995). Performance of multiple mass dampers under random loading. *Journal of structural engineering*, 121(2), 348-361.

- Kobori, T., Takahashi, M., Nasu, T., Niwa, N., & Ogasawara, K. (1993). Seismic response controlled structure with active variable stiffness system. *Earthquake Engineering & Structural Dynamics*, 22(11), 925-941.
- Kobori, T., Inoue, Y., Seto, K., Iemura, H., Nishitani, A. (Eds.), *Proceedings of Second World Conference on Structural Control*, Wiley, New York, 1998.
- Li, C. (2000). Performance of multiple tuned mass dampers for attenuating undesirable oscillations of structures under the ground acceleration. *Earthquake Engineering & Structural Dynamics*, 29(9), 1405-1421.
- Li, C. (2002). Optimum multiple tuned mass dampers for structures under the ground acceleration based on DDMF and ADMF. *Earthquake Engineering & Structural Dynamics*, 31(4), 897-919.
- Linderman, L. E., & Spencer Jr, B. F. (2016). Decentralized Active Control of Multistory Civil Structure with Wireless Smart Sensor Nodes. *Journal of Engineering Mechanics*, 142(10), 04016078.
- Liu, Y., Matsuhisa, H., and Utsuno, H. (2008). "Semi-active vibration isolation system with variable stiffness and damping control." *Journal of Sound and Vibration*, 313(1–2), 16-28.
- Loftness, V., Hartkopf, V., Gurtekin, B., Hansen, D., & Hitchcock, R. (2003). Linking energy to health and productivity in the built environment. Paper presented at the Greenbuild conference.
- Masri SF, Bekey GA and Caughey TK. Optimum pulse control of flexible structures. *J Appl Mech: T ASME* 1981; 48: 619–626.

- Manz, H., Loutzenhiser, P., Frank, T., Strachan, P. A., Bundi, R., & Maxwell, G. (2006). Series of experiments for empirical validation of solar gain modeling in building energy simulation codes—Experimental setup, test cell characterization, specifications and uncertainty analysis. *Building and environment*, 41(12), 1784-1797.
- Min, J.H., Gelo, N.J., and Jo, H. (2015), “Non-contact and Real-time Dynamic Displacement Monitoring using Smartphone Technologies”, *Journal of Life Cycle Reliability and Safety Engineering*, 4 (2), 40-51.
- Moon, K. S. (2009). Tall building motion control using double skin façades. *Journal of architectural engineering*, 15(3), 84-90.
- Moog Animatics SM23165D (2017). Retrieved July 02, 2017, from <http://www.animatics.com/products/smartmotor/animatics/nema-23-2300-series/sm23165d.html>.
- Murty, C. V. R. (2005). Earthquake tips. Indian Institute of Technology Kanpur, India.
- National Instrument, Converting a Desktop PC to a LabVIEW Real-Time Target. Retrieved April 25, 2017, from <http://www.ni.com/tutorial/2733/en/>.
- Obayashi Corporation (2012). “Hula Mass Damper System.” Retrieved March 22, 2016, from http://www.obayashi.co.jp/service_and_technology/related/tech60 (in Japanese).
- Omenzetter, P., Beskhyroun, S., Shabbir, F., Chen, G. W., Chen, X., Wang, S., & Zha, W. (2013). Forced and Ambient Vibration Testing of Full Scale Bridges. A report submitted to Earthquake Commission Research Foundation (Project No. UNI/578).

- Pappas, A., & Zhai, Z. (2006). Energy simulation of a double skin façade: a process using CFD and EnergyPlus. Paper presented at the Proceedings of the Second National IBPSA-USA Conference, Cambridge, Massachusetts.
- Poole, M., & Shvartzberg, M. (2015). *The Politics of Parametricism: Digital Technologies in Architecture*: Bloomsbury Publishing.
- Rahmani, B., Kandar, M. Z., & Rahmani, P. (2012). How double skin Façade's air-gap sizes effect on lowering solar heat gain in tropical climate. *World Applied Sciences Journal*, 18(6), 774-778.
- Ramallo, J. C., Johnson, E. A., & Spencer Jr, B. F. (2002). "Smart" base isolation systems. *Journal of Engineering Mechanics*, 128(10), 1088-1099.
- Randall, S., Halsted, D., & Taylor, D. (1981). Optimum vibration absorbers for linear damped systems. *Journal of Mechanical Design*, 103(4), 908-913.
- Reinhorn, A. M. (1989). 1: 4 scale model studies of active tendon systems and active mass dampers for aseismic protection: National Center for Earthquake Engineering Research.
- Rytter, A. (1993). "Vibration based inspection of civil engineering structures," Ph. D. Dissertation, Department of Building Technology and Structural Engineering, Aalborg University, Denmark.
- Ross, M. (2010), "Slow Flow: New Wind Tunnel Is Largest of Its Type", UNH Photographic Services. Retrieved December 02, 2015, from http://www.unh.edu/news/cj_nr/2010/nov/bp15tunnel.cfm

- Saelens, D., Roels, S., & Hens, H. (2008). Strategies to improve the energy performance of multiple-skin facades. *Building and Environment*, 43(4), 638-650.
- Sae-Ung, S. (1976). ACTIVE CONTROL OF BUILDING STRUCTURES SUBJECTED TO WIND LOADS. (PhD), Purdue University.
- Sakamoto, M. and T. Kobori. (1994). "Practical Applications of Active and Hybrid Response Control Systems." Proc. of the Int. Workshop on Struct. Control, Univ. of Southern California, pp. 432-46.
- Santhosh, H., Manjunath, K., & Kumar, K. S. (2013). Seismic analysis of low to medium rise building for base isolation. Paper presented at the IC-RICE Conference Issue| Nov-2013, Available@ <http://www.ijret.org>. Fixed Base Top Isolated.
- Simiu, E., & Scanlan, R. H. (1996). *cWind effects on structures*: Wiley.
- Singh, M., Matheu, E., & Suarez, L. (1997). ACTIVE AND SEMI-ACTIVE CONTROL OF STRUCTURES UNDER SEISMIC EXCITATION. *Earthquake Engineering & Structural Dynamics*, 26(2), 193-213.
- Smola, A. J., & Schölkopf, B. (2004). A tutorial on support vector regression. *Statistics and computing*, 14(3), 199-222.
- Soong, T., & Spencer Jr Reviewer, B. (1992). Active structural control: theory and practice. *Journal of Engineering Mechanics*, 118(6), 1282-1285.
- Spencer, B. (2002). Smart damping technologies for dynamic hazard mitigation. NIST SPECIAL PUBLICATION SP, 75-82.

- Spencer, B., Dyke, S., & Deoskar, H. (1998). Benchmark problems in structural control: part I-active mass driver system. *Earthquake Engineering and Structural Dynamics*, 27(11), 1127-1140.
- Stec, W., & Van Paassen, A. (2005). Symbiosis of the double skin façade with the HVAC system. *Energy and Buildings*, 37(5), 461-469.
- Stengel, R.F. (1986). *Stochastic Optimal Control: Theory and Application*. New York: John Wiley & Sons.
- Suhardjo, J., Spencer Jr, B., & Kareem, A. (1992). Frequency domain optimal control of wind-excited buildings. *Journal of Engineering Mechanics*, 118(12), 2463-2481.
- TAS. (2009). Software package for the thermal analysis of buildings, 13/14 Cofferidge Close, Stony Stratford, Milton Keynes MK11 1BY, UK.
- Tsai, H. C., & Lin, G. C. (1993). Optimum tuned-mass dampers for minimizing steady-state response of support-excited and damped systems. *Earthquake Engineering & Structural Dynamics*, 22(11), 957-973.
- The Smart Buildings Institute. (2015). Retrieved December 02, 2015, from <http://www.smartbuildingsinstitute.org>
- Warburton, G. (1981). Optimum absorber parameters for minimizing vibration response. *Earthquake Engineering & Structural Dynamics*, 9(3), 251-262.
- Warburton, G. (1982). Optimum absorber parameters for various combinations of response and excitation parameters. *Earthquake Engineering & Structural Dynamics*, 10(3), 381-401.

- Warburton, G., & Ayorinde, E. (1980). Optimum absorber parameters for simple systems. *Earthquake Engineering & Structural Dynamics*, 8(3), 197-217.
- Wigginton, M., & Harris, J. (2013). *Intelligent skins*: Routledge.
- Wu, J.-C., & Pan, B.-C. (2002). Wind tunnel verification of actively controlled high-rise building in along-wind motion. *Journal of Wind Engineering and Industrial Aerodynamics*, 90(12), 1933-1950.
- Xi, W. (2014). *Performance Based Implementation of Seismic Protective Devices for Structures*.
- Xu, L., & Ojima, T. (2007). Field experiments on natural energy utilization in a residential house with a double skin façade system. *Building and Environment*, 42(5), 2014-2023.
- Yamaguchi, H., & Harnpornchai, N. (1993). Fundamental characteristics of multiple tuned mass dampers for suppressing harmonically forced oscillations. *Earthquake Engineering & Structural Dynamics*, 22(1), 51-62.
- Yang, J., & Samali, B. (1983). Control of tall buildings in along-wind motion. *Journal of Structural Engineering*, 109(1), 50-68.
- Zhang, C., & Ou, J. (2008). Control strategies and experimental verifications of the electromagnetic mass damper system for structural vibration control. *Earthquake Engineering and Engineering Vibration*, 7(2), 181-192.
- Zuo, L., & Nayfeh, S. A. (2005). Optimization of the individual stiffness and damping parameters in multiple-tuned-mass-damper systems. *Journal of Vibration and Acoustics*, 127(1), 77-83.